PhD program in Material Science and Nanotechnology

Cycle XXXVIII

Design and Development of Functional Fillers for Applications in Advanced Self-Healing and Self-Sensing Polymer Composites

PhD Candidate: Marta Colombo

Registration number: 825231

Tutor: Prof. Massimiliano D'Arienzo

Industrial Tutor: Massimiliano Riva

Coordinator: Prof. Francesco Montalenti

ACADEMIC YEAR 2024/2025

Finanziato dall'Unione europea NextGenerationEU

Ministero dell'Università e della Ricerca

Italiadomani PIANO NAZIONALE DI RIPRESA E RESILIENZA

Contents

Glossary

APTES	*3-Aminopropyltriethoxysilane*
ATR-FTIR	*Attenuated Total Reflectance Fourier Transform Infrared*
BET	*Brunauer-Emmett-Teller Theory*
BJH	*Barrett-Joyner-Halenda Method*
CF	*Carbon Fiber*
CNTs	*Carbon nanotubes*
CNTs_TA	*Carbon nanotubes after an acid treatment*
CNTs@ZnO	*Carbon nanotubes decorated with ZnO nanoparticles*
CVD	*Chemical Vapour Deposition*
DMA	*Dynamic Mechanical Analysis*
DSC	*Differential Scanning Calorimetry*
EDX	*Energy Dispersive X-ray Spectroscopy*
EMAA	P*oly(ethylene-co-methacrylic acid)*
FRPs	*Fibre Reinforced Polymers*
F3P	*Three-point Flexural Test*
GF	*Glass Fiber*
GFRPs	*Glass Fibre Reinforced Polymers*
GO	*Graphene oxide*
IFSS	*Interfacial Shear Strength*
ILSS	*Interlaminar Shear Strength*
MWCNTs	*Multi-walled carbon nanotubes*
NBBs	*Nanobuilding Blocks*
NMR	*Nuclear Magnetic Resonance*
NPs	*Nanoparticles*

PDMS	*Polydimethylsiloxane*
rGO	*Reduced Graphene Oxide*
SEM	*Scanning Electron Microscopy*
sGF	*GF sprayed with rGO and EMAA*
sGF/rGO	*GF sprayed with rGO and EMAA with rGO embedded in the matrix*
SH	*Self-Healing*
SHM	*Structural-Health Monitoring*
SiO_2	*Silica nanoparticles*
SSA	*Specific surface area*
SWCNTs	*Single-walled carbon nanotubes*
TEM	*Transmission Electron Microscopy*
TEOS	*Tetraethyl orthosilicate*
TGA	*Thermal Gravimetric Analysis*
UV-Vis	*Ultraviolet-Visible*
XNBR	*Carboxylated Nitrile Butadiene Rubber*
XPS	*X-ray Photoelectron Spectroscopy*
XRD	*X-Ray Diffraction Analysis*
X@rGO	*Hybrid filler with rGO (X=SiO_2, Halloysite)*
ZnO	*Zinc Oxide*

Preface

The advancement of hybrid materials and nanocomposites has opened new frontiers in the development of multifunctional systems that combine high mechanical performance with intelligent functionalities. Hybrid materials, defined as intimate mixtures of organic and inorganic components, exhibit unique synergistic properties that arise from interactions at their interfaces rather than from the individual characteristics of each constituent. When these interfaces operate at the nanoscale, the resulting nanocomposites often display exceptional mechanical, electrical, and thermal properties, making them highly versatile for advanced technological applications.

Within this evolving field, particular attention has been directed toward smart polymer composites, a class of materials capable of responding to external stimuli such as stress, strain, temperature, or electric fields. Among them, self-sensing composites have emerged as a promising solution to revolutionize structural health monitoring (SHM). Conventional SHM systems depend on external sensors embedded within structures to track their condition. Although effective, these systems add complexity, cost, and weight, and often struggle to detect internal or micro-scale damage in real time due to wiring and data acquisition limitations. In contrast, self-sensing materials integrate the sensing capability directly within the material itself by embedding conductive nanofillers which form internal percolative networks that autonomously detect structural changes acting as artificial neurons that perceive and transmit signals in response to mechanical stimuli. Changes in electrical resistance caused by cracks, delamination, or deformation thus serve as immediate indicators of damage, enabling continuous, in-situ monitoring without the need for external sensors.

Beyond self-sensing, recent research efforts have also focused on self-healing composites, which introduce an additional level of intelligence by enabling materials to autonomously repair damage after mechanical failure or environmental degradation. These systems combine physical responsiveness with chemical adaptability, allowing polymer chains to reconfigure or re-bond through reversible interactions such as hydrogen bonding, ionic cross-links, or dynamic covalent chemistry. The integration of self-healing and self-sensing functionalities thus paves the way for truly autonomous structural materials, capable not only of detecting damage but also of responding to it, restoring mechanical integrity and extending service life.

This thesis investigates the design, synthesis, and characterization of multifunctional hybrid composites integrating these functionalities through three main research streams:

1. X@rGO (X = SiO_2 nanoparticles or Halloysite nanotubes) has been designed to integrate the high surface area and conductivity of reduced graphene oxide with the reinforcement and chemical

stability of ceramic phases. The filler has been embedded in epoxy matrix for glass fiber reinforced polymer composite (GFRPs) as reinforcement and conductive unit for self-sensing applications. Moreover, the same filler was introduced in polydimethylsiloxane (PDMS) enhancing reinforcement and imparting electrical conductivity to the matrix film that can be exploited for potential applications as a stretchable piezoresistive sensors.

2. CNTs@ZnO has been developed to combine the exceptional electrical conductivity of carbon nanotubes with the dynamic ionic crosslinking ability of zinc oxide. When incorporated into carboxylated rubber matrices (e.g. XNBR), these hybrids enable self-healing through reversible Zn^{2+}-COOH interactions, while simultaneously imparting electrical conductivity for damage monitoring that can be exploited in many applications such as the O-ring production.
3. GFRPs incorporating modified glass fibers coated with reduced graphene oxide (rGO) and self-healing polymers were produced to extend these concepts to structural composites. This strategy demonstrates the potential for lightweight, robust, and multifunctional composite systems capable of in-situ damage detection and recovery for many applications (e.g. automotive, structural or wind industries).

Structure of the thesis

Chapter 1 reports a general scenario on smart polymer composite for self-sensing, focusing on the introduction of carbon-based filler in GFRPs by matrix or fiber surface modification, and for self-healing with a particular attention to the ionomer's strategy. Later, a focus on the material employed in these systems is presented, especially referring to ceramic- and carbon-based filler.

Chapter 2 focuses on the synthesis and characterization of the hybrid filler X@rGO based on silica nanoparticles and commercial halloysite. It begins with Stöber method for the synthesis of SiO_2 NPs with a diameter of 70 nm. Then, the surface functionalization with alkoxysilane (APTES) occurs. The last step is the anchoring of graphene oxide in water and the thermal reduction in H_2/N_2 atmosphere of the filler. The hybrid filler X@rGO is then embedded in a PDMS matrix and characterized in terms of mechanical, thermal, and dielectric properties, highlighting how the presence of rGO-modified fillers influences crosslinking dynamics, conductivity, and interfacial polarization phenomena. Lastly, SiO_2@rGO has been embedded in an epoxy matrix for GFRPs composite and tested the interfacial adhesion fibre-matrix in presence of the hybrid filler with a micromechanical test.

Chapter 3 overviews the synthesis and characterization of the hybrid filler CNTs@ZnO through a soft-chemistry approach starting from a zinc precursor (i.e. zinc acetate dihydrate) that hydrolyses and condensates on the carbon nanotubes surface. The interaction between hybrid filler and carboxylic

group termination of stearic acid as a polymer model compound to assess the availability of ZnO has been tested. Lastly, the nanocomposite of CNTs@ZnO in XNBR matrix have been developed and tested in terms of mechanical, electrical and self-healing properties.

Chapter 4 outlines the optimization of rGO/EMAA coating though spray-coating method for the physical modification of the glass fiber surface. The manufacturing process of the 4-ply laminates by hand lay-up has been developed and the mechanical properties of the laminates have been tested. Finally, healing tests of the specimens have been conducted through an optimized healing protocol.

Chapter 5 presents a comprehensive summary of the thesis, synthesizing the main findings and results obtained throughout the research. It also discusses future perspectives, identifying areas that require further optimization to improve material properties and performance, and proposes potential directions for continued research and development.

1. Introduction

1.1 Hybrid materials and Nanocomposites

According to the International Union of Pure and Applied Chemistry (IUPAC)[1], Hybrid Material is composed of an intimate mixture of inorganic components, organic components or both types of components, usually interpenetrating on scale of less than 1µm. On the other hand, the term Nanocomposite is defined as a composite in which at least one of the phase domains has at least one dimension of the order of nanometres. While nanocomposites fall within the category of hybrid materials, not all hybrid materials qualify as nanocomposites. This distinction is critical, as extensive research has demonstrated that nanoscale dimensions exert a deep influence on the resulting material properties, often yielding behaviours and performance characteristics that differ substantially from those of systems lacking nanoscale features.

The properties of hybrid materials are not merely the sum of their individual components. Instead, they emerge from the strong synergy generated by the extensive hybrid interface. This organic–inorganic interface, defined by the type of interactions, bonding energy, and connectivity, plays a dominant role in modulating a large number of properties such as optical behaviour, mechanical strength, separation efficiency, catalytic activity, and resistance to chemical and thermal stresses[2].

The nature of the interactions between the organic and inorganic components defines two distinct classes of hybrid materials[3]. In *Class I hybrid materials*, the organic and inorganic components interact through weak interactions such as van der Waals forces, hydrogen bonding or electrostatic interactions. In contrast, *Class II hybrid materials* involve phases that are wholly or partially connected by strong chemical bonds, characterized by significant orbital overlap, including covalent or ionic bonds. The interaction mechanisms between organic and inorganic species, also govern their properties. Weak interactions (e.g. hydrogen bonding, van der Waals forces) may allow dynamic processes such as aggregation, phase separation, or leaching, whereas strong interactions (e.g., covalent bonds) provide greater stability, as seen in nanoparticle/polymer networks. The choice of interaction strength can be tailored to the desired properties; for instance, weak interactions enable component mobility, while specific interactions such as coordination or electron transfer can significantly influence electronic behaviour[4].

Beyond the nature of the interface and the intended application, an equally critical aspect in designing hybrid networks lies in the chemical pathways employed to synthesize the material. A summarized global view of the different approaches to generate a hybrid material is presented in Figure 1.1.

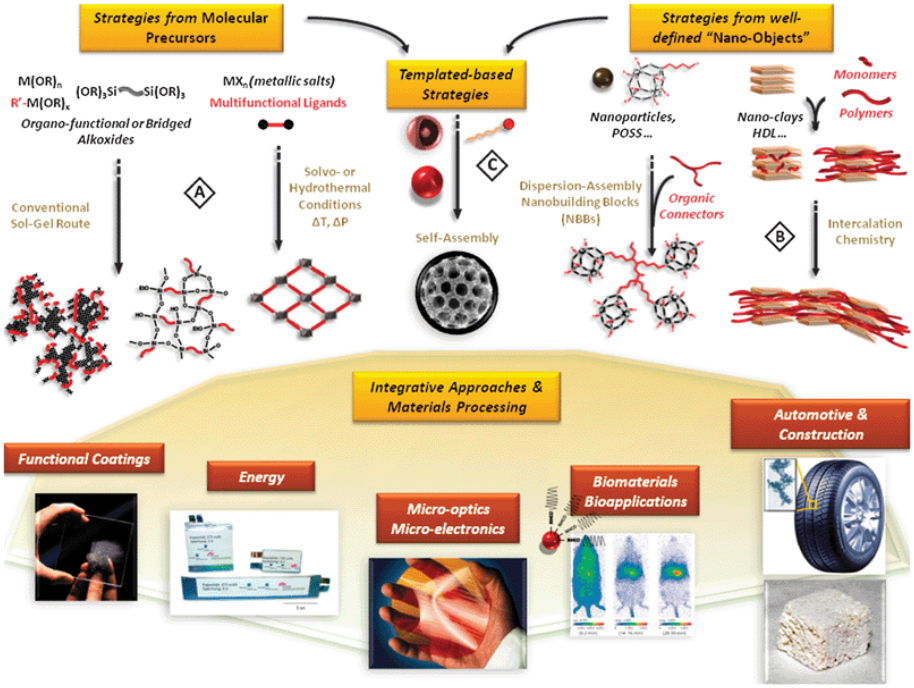

Figure 1.1 Schematic illustration of the different pathways for synthetizing hybrid materials[2].

Three different bottom-up strategies have been highlighted to design advanced materials[5]. *Route A* is soft chemistry strategy which includes sol-gel chemistry and solvo- or hydrothermal synthesis. These low-cost strategies produce amorphous nanocomposite hybrid materials with various microstructures, high versatility, and useful properties, making them suitable for commercial applications such as films, powders, or monoliths. Despite these advantages, they often suffer from size polydispersity and local chemical heterogeneity. Advancing academic understanding and achieving precise control over their local and semi-local structure will be crucial for tailoring properties in future applications. *Route B* corresponds to the hybridization of Nanobuilding Blocks (NBBs) via assembling or intercalation. These NBBs are nanometric, monodispersed and with a defined structure which is maintained in the final nanocomposite (i.e. clusters, modified nanoparticles, clays, nanocore-shells, etc...). Nanobuilding blocks can be functionalized with polymerizable ligands, organic spacers, or dendrimers, enabling diverse architectures and organic–inorganic interfaces through various assembly strategies. Stepwise synthesis further provides precise control over their semi-local structure. *Route C*, based on self-assembly strategy, focuses on the organization of growing inorganic or hybrid networks, where organic surfactants act as templates. Within this framework, organic–inorganic hybrid phases stand out for their versatility, enabling the design of a wide spectrum of nanocomposites: from ordered dispersions of inorganic domains in hybrid matrices to controlled nano segregation of organic polymers within inorganic frameworks. This ability to tune architecture at the nanoscale paves the way for the development of functional materials with tailored properties.

1.2 Smart polymer composites

In recent years, the rise of smart materials and technologies has paralleled the development of hybrid and composite materials. The official and standard definition of Smart material has not been published by IUPAC, but this term refers to a material whose properties are modulated by external stimuli, enabling application in various fields (e.g. structural monitoring, packaging, automotive, aerospace, and medical devices). These external stimuli can range from strain, stress, temperature, light, chemicals (including pH), electric and magnetic fields, hydrostatic pressure, radiation, and more.

Among the various smart materials, the class of Smart polymer composite has been reaching significant attention in the last years thanks to their versatility in various fields of application. These materials are composed of a nano- or micro-filler with an organic (like natural fibers) or inorganic (e.g. graphene oxide, ceramics and glass fiber) nature, embedded in a polymer (i.e. thermosetting and thermoplastic). In the next sections two types of smart polymer composite have been deeply exploited: self-sensing and self-healing composites.

1.2.1 Self-sensing composites

The use of advanced GFRPs in structural applications has grown rapidly in recent years, driven by major industries such as aerospace, automotive, wind energy, and construction. Their widespread adoption stems from their outstanding mechanical performance (e.g. high stiffness and fatigue resistance provided by reinforcing fibers within the polymer matrix) combined with low production costs, chemical stability, and design flexibility, which make them attractive alternatives to metals and ceramics. Given these applications, safety and long-term reliability are essential to ensure the secure use of composite materials, especially for components with extended service lives, such as turbine blades designed for 25 years or car frames expected to endure over 200,000 km. However, achieving high-performance structures remains challenging, as they often operate under severe conditions involving complex multiaxial cyclic loads, high stress or strain levels, and occasional extreme events. These factors can progressively reduce the material stiffness—by as much as 30–40% before final failure. Moreover, defects and damage such as voids, fiber wrinkling, delamination, or impact-induced flaws can develop throughout the lifecycle of GFRPs, affecting the matrix, fibers, and particularly their interfaces.

Early identification of structural damage or potential failure is crucial to ensure operational safety. Conventional non-destructive testing (NDT) techniques, such as visual inspection, ultrasonic, thermographic, infrared, radiographic, and electromagnetic testing, are widely employed to detect defects and failures. However, these methods depend on scheduled periodic inspections carried out by external operators, which can lead to delayed detection and increased maintenance costs.

To address these limitations, structural health monitoring (SHM) technologies have recently emerged as a promising alternative. These systems enable in situ and real-time detection of damage by integrating sensors directly into the structure, allowing continuous monitoring and early identification of potential failures. This capability is particularly valuable for detecting internal damage, which often goes unnoticed using conventional techniques like visual inspection.

In general, SHM relies on permanently embedded or surface-mounted sensors and actuators (e.g. acoustic emission or optical fiber sensors) that record the real-time response of the material under service conditions. The operating principle of SHM can be compared to that of a biological nervous system: the sensors act as sensory receptors that detect structural changes and transmit the information to a central processing unit (Figure 1.2a), which then interprets the signal and triggers an appropriate response.

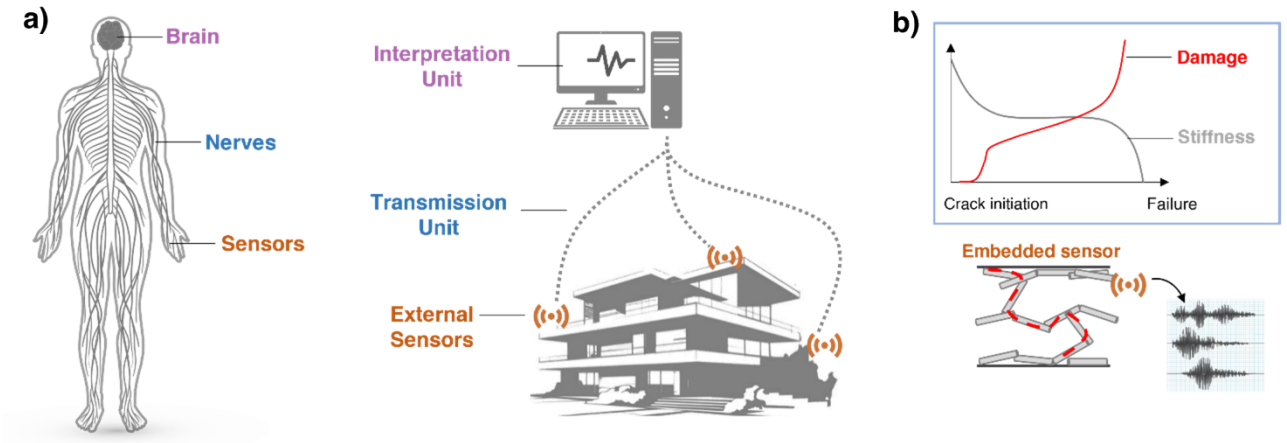

Figure 1.2 a) Analogy between the human body and smart structures with SHM systems; b) Schematic representation of a cross-ply composite incorporating a conductive filler network, illustrating the associated stiffness reduction and increase in electrical resistance under service loading. The red dashed line indicates the conduction pathway through the percolating network[6].

Research in the field of structural health monitoring has increasingly shifted toward the development of smart materials with intrinsic self-sensing capabilities, capable of monitoring their own structural integrity without the need for external sensors, cables, or wiring. This new generation of materials offers a significant reduction in both cost and weight compared to traditional SHM systems, while also simplifying the overall design and integration process. In these self-sensing composites, the monitoring functionality is achieved through the incorporation of electrically conductive fillers—such as carbon nanotubes, graphene nanoplatelets, carbon black, or metallic nanowires—into the polymer matrix of glass fiber-reinforced polymers (GFRPs). These fillers not only contribute to the mechanical reinforcement of the composite but also act as “artificial neurons,” enabling the material to detect and respond to damage events in real time. When uniformly dispersed within the epoxy matrix, the

conductive fillers create a percolated conductive network throughout the composite [7]. Under normal operating conditions, this network ensures stable electrical conductivity. However, when structural damage occurs (e.g. microcrack initiation, fiber–matrix debonding, or delamination) the local conductive pathways are disrupted. These interruptions lead to a measurable increase in electrical resistance, which directly correlates with the extent of the damage. Consequently, variations in the composite's electrical resistance can be used as a reliable damage-sensing parameter, allowing for the quantitative evaluation of the material's health state without the need for destructive mechanical testing. This concept forms the basis of self-sensing SHM materials, which combine reinforcement capability and sensing functionality within a single, multifunctional structure.

Figure 1.2b presents a schematic representation of the self-monitoring mechanism in a GFRPs, where the dashed red line illustrates the electrical conduction pathway formed through the percolating network of conductive fillers. Electrical conductivity in such systems arises from two main mechanisms: ohmic conduction, occurring through direct contact between adjacent filler particles, and tunnelling conduction, which takes place across the nanometric gaps separating individual particles or agglomerates[7]. Throughout the study, a comprehensive damage analysis of the composites is performed to evaluate the primary damage mechanisms (e.g. crack initiation, crack propagation, and fiber failure) under different loading conditions, including static, fatigue, and impact tests. The self-monitoring performance of the material is assessed by tracking the changes in electrical resistance during mechanical loading, thereby correlating variations in conductivity with the progression of damage and demonstrating the self-sensing capability of the composites. The main advantage of this approach lies in its non-invasive and in-situ nature, offering high sensitivity to both matrix and interfacial damage. Moreover, it provides remarkable versatility and design flexibility, as the sensing performance can be tailored by adjusting the type, size, shape, and concentration of conductive fillers. These fillers can be incorporated into the composite matrix using various physical and chemical techniques, such as direct mixing with the resin, surface coating of the glass fibers, or chemical grafting. Nonetheless, achieving appropriate processing conditions is essential to ensure uniform filler dispersion and distribution, which promotes the formation of a stable conductive network while preserving the mechanical integrity of the GFRP.

The fiber–filler/matrix interface is a critical factor in the progressive damage of GFRPs, as stress concentrations arise from mismatched thermal expansion coefficients. This interface is better described as an interphase, a transition region where the physical, chemical, and mechanical properties gradually evolve from fiber to matrix and are strongly influenced by fiber surface topography and processing conditions[8]. Adhesion at the interface can occur through several mechanisms, including mechanical interlocking, electrostatic attraction, interdiffusion, and chemical bonding, with

their contribution depending on surface characteristics. The incorporation of carbon-based fillers (e.g., CNTs, graphene, GO) enhances these mechanisms by increasing surface roughness, improving wettability, and promoting polymer chain penetration. Functionalized nanofillers can additionally form covalent or van der Waals bonds with both fibers and matrix, leading to stronger adhesion, more efficient load transfer, reduced voids, and a more uniform stress distribution.

Beyond strengthening, nanofillers also improve electrical conductivity and piezoresistive response, imparting multifunctionality by simultaneously enhancing both the mechanical performance and the self-sensing capability of GFRPs. However, achieving homogeneous filler dispersion and distribution, minimizing aggregation and tailoring the filler/matrix interface remain critical to ensuring a robust conductive network while preserving the intrinsic mechanical performance of GFRPs.

1.2.1.1 Introduction of carbon-based filler in GFRPs

Achieving self-sensing behaviour requires the filler content to exceed the percolation threshold, where a continuous 3D conductive network is formed within the matrix. CNTs, due to their high aspect ratio, typically reach percolation at very low loadings (0.01–1 wt.%), whereas rGO generally requires higher contents (0.1–2 wt.%), depending on exfoliation and processing conditions[9].

Several strategies have been reported for incorporating carbon-based fillers into GFRPs, including matrix modification via mechanical mixing, as well as fiber modification through physical, chemical, thermal, or coating treatments.

Matrix modification

In this approach, carbon-based fillers are first dispersed in the resin, after which GFRP composites are fabricated using the manufacturing techniques described in Section 1.3.1. The main challenges of this method concern achieving uniform filler dispersion within the matrix while preventing aggregation and excessive increases in viscosity. Graphene and its derivatives tend to strongly agglomerate due to van der Waals forces and π-π interactions between lamellae, whereas the high aspect ratio of CNTs promotes the formation of entangled clusters. As a result, careful optimization of filler loading is essential. To address these issues, physical dispersion techniques such as ultrasonication or three-roll milling are often employed to break down aggregates, enhance homogeneity, and prevent the presence of clusters larger than the inter-tow spacing of the fibers.

GF modification

An alternative strategy for introducing carbon fillers into GFRPs involves fiber surface modification through coating or chemical grafting. Since GFs are typically coated with a sizing layer (mainly silane

coupling agents, film formers, and additives) to protect against damage and improve matrix adhesion, tailoring or removing this layer can enhance compatibility with carbon-based fillers.

- *Fiber coating*: Coating is a surface modification technique for GFs, in which layers of a carbon-based filler suspension are deposited, with the stability of the dispersion being crucial to achieve a uniform and homogeneous film. As shown in Figure 1.3, several methods can be employed for this purpose, including dip-coating[10,11], doctor blade coating[12], chemical vapor deposition (CVD)[13], electrophoretic deposition (EPD)[14,15], and spray-coating[16,17].

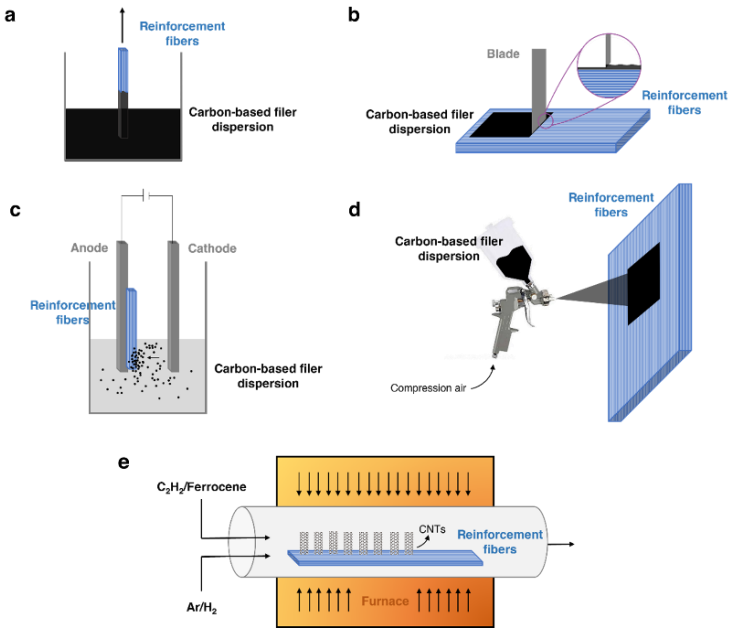

Figure 1.3 Schematic illustration of GFRP coating techniques: (a) dip-coating, (b) doctor blade coating, (c) EPD, (d) spray coating, and (e) CVD[6].

- *Chemical grafting*: The fiber/epoxy interface is critical in GFRPs for efficient load transfer, but in the absence of primary bonds, only weak secondary interactions occur, which deteriorate under wet conditions as water molecules disrupt the interface. To overcome this, compatibilizing agents[18], particularly organofunctional silanes, are widely employed. Their effectiveness depends on silane type, layer thickness, and substrate pretreatment, but under moisture exposure, the key factor is the formation of strong chemical bonds between silane, glass fibers, and epoxy. Through hydrolysis and condensation, silanes form a thin siloxane film that bonds with the matrix, creating a robust polymer/siloxane/glass interphase described by the Plueddemann model (Figure 1.4)[19].

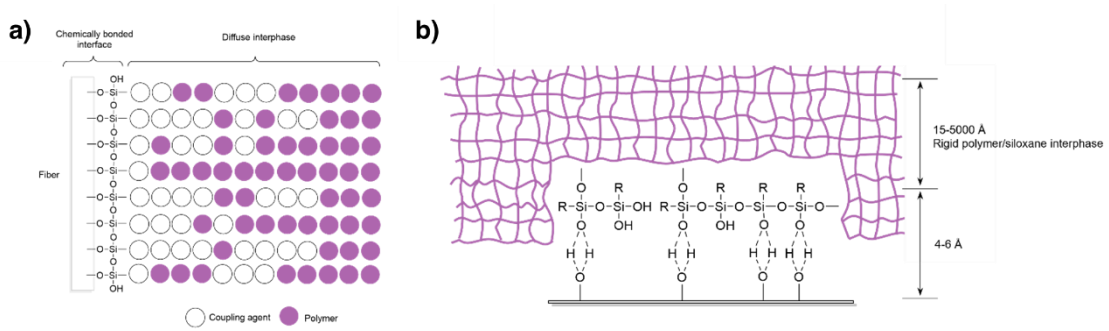

Figure 1.4 Schematic representations of (a) bonding between siloxane and polymer chains, and (b) the polymer/siloxane/glass fiber interphase[6].

A key-role is played by the interphase between glass fiber and epoxy, in fact is important to modify the interface to tune the mechanical properties of the composite. Various techniques exist to evaluate fiber/matrix interfacial strength in continuous fiber composites, ranging from micro-scale tests on individual fibers to macro-scale tests on full laminates. The main micromechanical methods for evaluating the fiber–matrix interface in fiber-reinforced polymers are the fiber fragmentation[20,21], microbond (droplet strip-off)[22,23], single-fiber pull-out [24,25], and single-fiber push-out tests [26,27]. All primarily generate interfacial shear stress, enabling the determination of the interfacial shear strength (IFSS).

- The fiber fragmentation test measures fiber breakage under tension to estimate the critical fiber length for effective stress transfer but is limited to transparent, ductile matrices and relies on simplifying assumptions.
- The microbond test uses small polymer droplets on a fiber that are stripped off to evaluate adhesion, offering simplicity and low material use, though stress field complexities may affect accuracy.
- The single-fiber pull-out test directly measures the force required to extract a fiber from a solidified droplet, providing detailed force–displacement data and versatility across fiber–matrix systems.
- The push-out test applies to real composite slices, pushing fibers out with a micro-punch. While sample preparation is demanding, it allows testing under more realistic composite conditions.

Overall, micro-scale tests offer controlled evaluation of interfacial properties, but their small-scale setups and simplified conditions may not fully replicate the behaviour of real composite materials under service environments.

Macro-mechanical testing methods evaluate the interfacial strength of fiber-reinforced composites at the laminate level, offering a more realistic representation of material performance than micro-scale tests. These methods induce shear stresses that often lead to interfacial or interlaminar failure; when

the failure is adhesive (fiber–matrix debonding), the measured shear strength directly reflects the interfacial shear strength (IFSS).

The three most common macro-mechanical tests are:

- Iosipescu shear test employs a notched specimen in a specialized fixture to generate a region of pure shear, providing detailed data on shear modulus, ultimate shear strength, and stress–strain behavior[28].
- ± 45° tensile test uses a laminate with fibers oriented at ± 45° to the loading axis; shear stresses arise during tension, allowing the calculation of in-plane shear modulus and strength, often revealing interfacial failure mechanisms[29].
- Short-beam shear (SBS) test applies a three-point bending setup with a low span-to-thickness ratio to promote interlaminar shear failure. Despite mixed stress states and potential stress concentrations, it remains a simple, rapid, and widely used method for assessing interlaminar shear strength (ILSS)[30].

Overall, macro-scale tests provide practical insights into fiber–matrix adhesion under realistic structural conditions, though results may be influenced by other failure mechanisms beyond the interface.

1.2.2 Self-healing composites

Inspired by natural systems, self-healing (SH) materials possess the capability to repair or restore damage by mimicking mechanisms observed in living organisms, such as plants and human skin. To define the fundamental requirements for successful self-healing, van der Zwaag[31] identified three key concepts and a fourth is necessary to allow a more comprehensive classification of the different generations of self-healing materials:

- *Localization*: The self-healing process depends on the depth of the damage in the material network. It can be superficial (e.g. scratches, microcrack, cut), deep (e.g. fiber debonding or delamination) or at molecular scale such as breakage of material network.
- *Temporality*: The second factor refers to the time gap between the occur of the damage and its repair (i.e. diffusion of the healing agent or reformations of bonds).
- *Mobility*: To decrease the temporality and optimize the healing process, the mobility, which promotes the healing agent diffusion as well as the restoring of the bonds, is crucial.
- *Mechanism*: The process can occur through an extrinsic or intrinsic mechanism leading to a classification of the SH materials[32–34]. The first class consists of a release of an external agent, typically stored in microcapsules or vascular networks, widely used in thermosetting matrices. This strategy, however, is generally restricted to repairing a single localized damage event.

Moreover, the applications remain limited due to weak interfacial interactions between the capsules and the polymer matrix, as well as the risk of premature capsule rupture during composite fabrication. Such events may not only prevent healing but can also act as crack initiators, ultimately impairing the mechanical properties of the material. On the other hand, intrinsic self-healing, widely applied to elastomer matrix systems, is based on the chemistry of dynamic reversible bonds which can be covalent (i.e. Diels-Alder[35], Disulfide bond[36,37], Schiff base[38], Boronic ester bonds[39,40] and Vitrimers[41]) or non-covalent (i.e. H bonding, π- π stacking, Host-guest interactions, metal-ligand coordination and ionic interactions) bonds. This last class of reversible supramolecular SH material will be deeply discussed in the next Section.

1.2.2.1 Intrinsic self-healing: ionomers strategy

A major challenge in designing self-healing polymers lies in reconciling two seemingly contradictory requirements: on one hand, outstanding mechanical properties demand a stable and rigid covalent network, while on the other, efficient self-healing relies on mobile and flexible polymer chains[42]. In this context, ionomers[43] have emerged as a promising class of materials.

Ionomers typically contain up to 15 mol% of ionic groups incorporated into the polymer backbone, which are partially or fully neutralized to form salts[44–46]. The ionic interactions in these materials often involve electrostatic interactions between carboxylate or sulfonate anions and counter cations originating from Group 1, Group 2, or transition metals. According to the Eisenberg model[47], these ionic species first associate into multiplets, which subsequently aggregate into larger clusters. Clusters are generally described as assemblies of multiplets surrounded by confined polymer chains with reduced mobility, giving rise to distinct ionic domains (Figure 1.5).

Crucially, the dynamic nature of these ionic domains, enabled by the ion-hopping mechanism (i.e. where ionic associations undergo thermo-reversible breaking and reformation) endows ionomers with their SH ability, while simultaneously maintaining good mechanical performance[48,49].

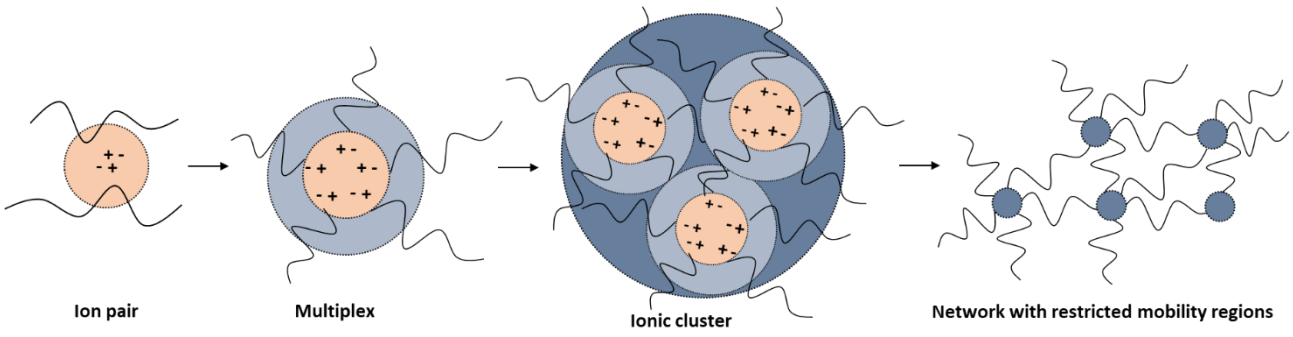

Figure 1.5 Hierarchy of ionic domains that act as restricted regions in the polymer network.

Metal oxide nanoparticles such as zinc oxide (ZnO) have attracted broad interest in the field of polymer engineering due to their high stability, good photocatalytic activity, antibacterial activity, and non-toxicity[50]. Additionally, ZnO nanoparticles represent a common material used in rubber vulcanization systems as a crosslinker or accelerator. Recent studies have highlighted the introduction of ZnO as an effective and versatile approach to generate reversible ionic dynamic interactions within rubbery matrices[51]. On a molecular level, the Zn^{2+} cations from ZnO can interact ionically with the carboxylic groups of a polymeric matrix, forming thermoreversible associations[51,52], as shown in Figure 1.6.

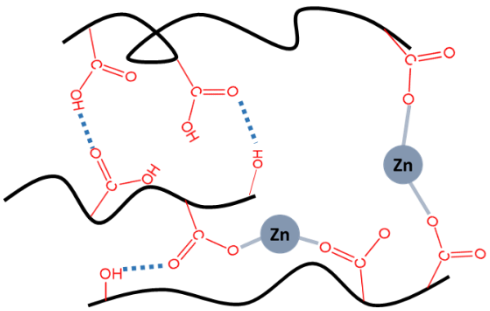

Figure 1.6. Schematic representation of Zn^{2+} coordinating carboxylic groups of the polymeric matrix.

In a similar context, Xu et al.[53] developed self-healing supramolecular elastomers through a controlled vulcanization process of natural rubber (NR) incorporating ionic cross-links. In this study, the authors deliberately adjusted the vulcanization conditions to prevent the formation of a conventional covalent cross-linked network, instead promoting the creation of reversible ionic cross-links by in situ polymerization of zinc dimethacrylate within the NR matrix. The resulting ionic supramolecular network exhibited enhanced chain mobility and dynamic behaviour, allowing fully cut surfaces to autonomously rejoin and recover their original mechanical properties after the self-healing process. Remarkably, healing efficiencies of 90–100% were achieved at room temperature within minutes. Specifically, Zn^{2+} coordinated with two carboxylic groups forms ionic clusters that can be readily graft-polymerized onto rubber chains through peroxide-induced vulcanization. In this configuration, Zn^{2+} ions serve as salt bridges between grafted polymer chains, contributing to the formation of a dynamic ionic network and facilitating the self-healing process. However, in polymer nanocomposites where the filler system is independent of the reversible supramolecular network, the addition of fillers often compromises the self-healing ability, despite improving mechanical strength. To overcome this limitation, Xu et al.[54] performed an in-situ reaction of methacrylic acid with zinc oxide within natural rubber to generate ionic cross-links. The residual ZnO particles introduced only minor hindrance to the reformation of ionic bonds due to the natural affinity between Zn^{2+}-rich ionic domains and ZnO. As a result, the homogeneously dispersed residual ZnO enhanced the mechanical performance of the material, while the system with an methacrylic acid/ZnO molar ratio of 2:1.4 achieved a healing efficiency of 53% after 1 minute, increasing to 76% after 5 minutes.

Recently, Shi et al.[55] developed thermoplastic silicone elastomers based on cross-linking interactions between ZnO and carboxylic acid groups grafted onto the side chains of polydimethylsiloxane (PDMS). The researchers achieved an optimal balance between mechanical strength and self-healing performance by employing a catalytic ring-opening polymerization of three vinyl-functional PDMS precursors initiated by trimeric phosphazene base. The carboxyl-functionalized PDMS (PDMS-g-COOH) was subsequently synthesized through a thiol–ene click reaction, and the final composite was obtained by reinforcing PDMS-g-COOH with ZnO nanoparticles. By adjusting the molecular weight of the PDMS precursors and the COOH/ZnO molar ratio, the team was able to tailor the mechanical and self-healing properties through the formation of dynamic salt-bonding networks. The resulting PDMS-g-COOH/ZnO nanocomposites demonstrated an impressive self-healing efficiency of 83.5% at 80°C after 4 hours, with a notable mechanical strength exceeding 5 MPa. In this system, the high-molecular-weight PDMS-g-COOH served as the primary network backbone, maintaining overall toughness, while the COO^-/Zn^{2+} coordination bonds acted as dynamic cross-links, effectively dissipating stress during deformation and enabling autonomous recovery.

1.3 Materials employed in these systems

1.3.1 GF

Glass fibers (GF) are synthetic fibers produced from silica-based, or other glass formulations, extruded into filaments with micrometric diameters. Fibers are generally classified as either natural (e.g., jute, flax, cellulose) or synthetic (e.g., carbon, glass, boron) [56–58]. Synthetic fibers typically provide higher stiffness, strength, and fatigue resistance than natural ones, while also exhibiting good compatibility with polymer matrices. This compatibility minimizes fiber aggregation and enhances moisture resistance[59]. While natural fibers offer sustainability, renewability, and biodegradability, their ability to significantly improve the mechanical performance of composites is limited. Consequently, synthetic fibers, particularly GF, have been widely favoured in structural applications.

GFs remain the most widely employed reinforcement in FRPs and can be classified according to their length and chemical composition, both of which critically influence the physical and mechanical behaviour of glass fiber–reinforced polymers. Fiber length governs orientation and thus dictates the structural performance of the composite[60,61].

Continuous fiber–reinforced composites, composed of long fibers typically arranged in tows or woven into uni-/bi-directional fabrics, enable highly efficient load transfer and superior mechanical strength.

In contrast, discontinuous fiber–reinforced composites, which use shorter fibers in chopped strand form (3–12 mm) or milled form (0.15–4 mm)[62], require careful design to ensure effective load transfer and to reduce crack initiation and propagation. Since the interfacial adhesion and overall strength of a composite scale directly with fiber length (for a given fiber volume fraction), shorter fibers generally result in reduced strength and fracture resistance[63].

Nevertheless, discontinuous fiber systems are attracting growing interest due to their cost-effectiveness, processing flexibility, and ability to achieve isotropic properties. They serve as an intermediate solution between continuous fiber laminates and neat polymers, offering enhanced stiffness and strength compared to the latter. Such materials are particularly relevant in civil engineering applications (e.g., pavements, concrete reinforcement) where wear resistance is critical[64], as well as in automotive applications, where manufacturing efficiency and reduced cost are major advantages.

The classification of GF according to their chemical composition is summarized in Table 1.1, where the capital letter (namely E, C, S, A, D, R) is used to discriminate the percentages of inorganic materials used to produce the fibres.

Table 1.1 Chemical compositions expressed in weight percent and physical properties of different GFs[6].

Type	SiO_2	Al_2O_3	TiO_2	B_2O_3	CaO	MgO	Na_2O	K_2O	Properties
E-glass	55.0	14.0	0.2	7.0	22.0	1.0	0.5	0.3	Higher strength and electrical resistivity
C-glass	64.6	4.1	-	5.0	13.4	3.3	9.6	0.5	Higher corrosion resistance
S-glass	65.0	25.0	-	-	-	10.0	-	-	Highest tensile strength
A-glass	67.5	3.5	-	1.5	6.5	4.5	13.5	3.0	Higher durability, strength and electric resistivity
D-glass	74.0	-	-	22.5	-	-	1.5	2.0	Low dielectric constant
R-glass	60.0	24.0	-	-	9.0	6.0	0.5	0.1	Higher strength and acid corrosion resistance

In general, GF are primarily composed of silica (SiO_2), which accounts for approximately 55–70 % of their content, followed by alumina (Al_2O_3) and various other metal oxides. These additional oxides are incorporated to finely tune the mechanical, electrical, and corrosion-resistant properties of the fibers. Among the different types, E-glass fibers (i.e. mainly consisting of SiO_2, CaO, and Al_2O_3) are the most widely used in GFRPs. They combine high strength, thermal stability, and electrical resistivity with excellent resistance to common chemical agents, abrasion, and vibration, as well as remarkable flexibility. These attributes explain their prevalence as the standard reinforcement in GFRPs.

Despite their many advantages, GFs also present drawbacks, such as a lower stiffness-to-density ratio compared to carbon fibers and, as previously noted, difficulties in disposal at the end of their service life[64]. GFRPs produced through multiple manufacturing steps, are particularly challenging to recycle or

reuse, making waste management a pressing research topic[65–67]. Mechanical grinding enables the direct reuse of fibers as chopped fillers in various applications, while chemical and thermal processes have been extensively investigated to recover GFRPs. However, these latter methods remain costly and environmentally burdensome, largely due to the significant energy required to reach the very high processing temperatures involved[68].

Manufacturing techniques of GFRPs

The main techniques used for the fabrication of GFRPs, particularly those employing thermosetting matrices, are summarized in Figure 1.7. Several manufacturing methods have been reported, including hand lay-up[69], resin transfer molding (RTM)[70], vacuum-assisted RTM (VARTM)[71,72], filament winding[73], pultrusion[74], compression molding[75], and automated fiber placement (AFP)[76,77]. The selection of a specific technique depends primarily on production costs and the targeted characteristics of the final composite, such as size, geometry, and mechanical performance. These methods differ mainly in the procedures used to combine the polymer matrix with the fibers (e.g., open mold, closed mold, resin bath) and in the curing processes applied.

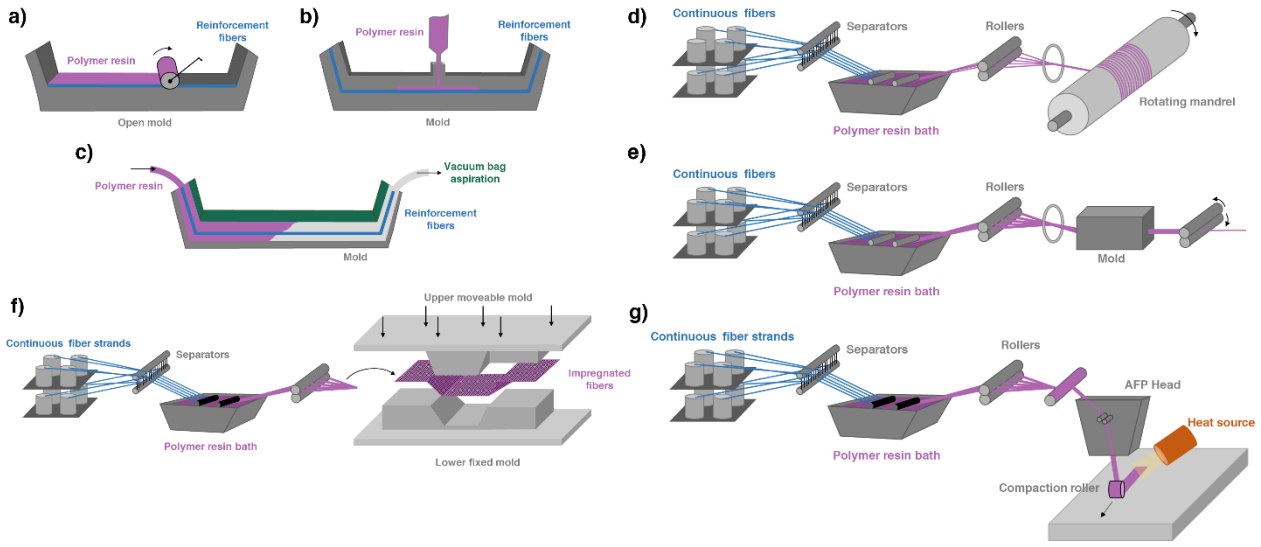

Figure 1.7 Schematic illustration of manufacturing techniques for GFRPs production: a) hand lay-up, b) resin transfer molding (RTM), c) vacuum-assisted resin transfer molding (VARTM), d) filament winding, e) pultrusion, f) compression molding, g) automated fiber placement (AFP)[6].

1.3.2 Nanofiller

1.3.2.1 Carbon-based filler

Carbon nanotubes (CNTs)

CNTs are carbon-based nanomaterials consisting of a single graphitic sheet (graphene) rolled into a cylindrical structure, with diameters in the nanometer range and lengths extending to the micrometer scale or beyond[78]. They can occur as single-walled CNTs (SWCNTs), composed of a single cylindrical layer, or as multi-walled CNTs (MWCNTs), where multiple concentric cylinders are nested within one another. Compared with other carbonaceous fillers, such as carbon black, CNTs exhibit exceptionally high aspect ratios and outstanding structural and functional properties, including superior mechanical strength and electrical conductivity[79]. These features arise from the sp^2 carbon–carbon bonding, which imparts very high tensile strength and low electrical resistivity—although the latter may be influenced by structural defects[80]. CNTs are also highly elastic, allowing them to recover their original shape after deformation. Owing to this unique combination of properties, they have been extensively investigated as reinforcing agents in composite materials to produce ultralight, mechanically robust systems[81].

CNTs also exhibit exceptional electrical and thermal conductivity (10^6–10^7 S m^{-1} and 3000–3500 W $m^{-1}K^{-1}$, respectively)[82], arising from the strong carbon–carbon bonds that enable them to withstand high electric currents and elevated temperatures. When incorporated into polymer composites, CNTs can impart electrical functionality, which is strongly influenced by their concentration, alignment, morphology, and dispersion within the matrix. Their geometry and resulting structure critically determine electrical, thermal, and mechanical performance, allowing CNTs to display either metallic-like conductivity or semiconducting behaviour. In the case of SWCNTs, this electronic behaviour is dictated by the graphene rolling direction, described by the chiral vector $\overrightarrow{C_h} = n\overrightarrow{a_1} + m\overrightarrow{a_2} = (n, m)$, represented in Figure 1.8. Depending on this configuration, CNTs can adopt armchair, zigzag, or chiral geometries[83,84]: armchair structures exhibit metallic conductivity, while zigzag and chiral forms present variable bandgap energies depending on diameter, spanning from metallic to semiconducting[85].

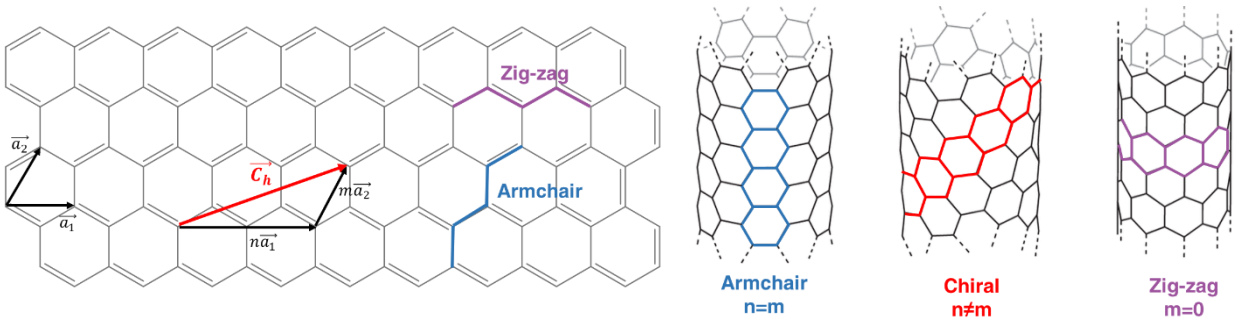

Figure 1.8 Schematic representation of the chiral vector and the three structures of SWCNTs[6].

For MWCNTs, two main structural models have been described: the *Parchment model*, where a single sheet is rolled multiple times, and the *Russian Doll model*, consisting of concentric SWCNTs with interlayer distances similar to graphite. Both models exhibit high electrical conductivity, but MWCNTs generally provide greater tensile strength and enhanced chemical stability, since inner walls are shielded from external reactions[86].

CNTs are typically synthesized using three main techniques: arc discharge[87–90], laser ablation[91,92], and chemical vapor deposition (CVD)[93–95]. All methods rely on supplying energy to a carbon source in the presence of a catalyst, producing carbon atoms or clusters that recombine to form nanotubes. The energy source varies—thermal (CVD), laser irradiation, or electrical discharge—and the choice of technique significantly affects CNT morphology, including diameter, length, purity, and defect density, thereby influencing their mechanical and electrical performance[96,97]. While graphite is used in arc discharge and laser ablation, CVD allows a wider range of carbon precursors, from fossil-based hydrocarbons (natural gas, acetylene, benzene, xylene, toluene) to renewable alternatives such as turpentine, eucalyptus, castor, coconut, and palm oils. Notably, waste cooking oils, such as recycled palm oil, represent a low-cost and environmentally attractive precursor for CNT synthesis[98].

CNTs have been widely investigated as reinforcements in GFRPs to improve their mechanical and multifunctional properties. Panchagnula et al.[99] reported that incorporating MWCNTs into an epoxy matrix by ball milling increased tensile strength and hardness at loadings up to 0.4 wt.%. In another study[100], CNTs were grafted onto glass fiber surfaces via CVD, which slightly reduced fiber tensile strength due to localized thermal degradation but improved interlaminar shear strength (ILSS) through CNT bridging, thereby enhancing flexural performance while maintaining overall tensile properties. Moreover, the intrinsic electrical conductivity of CNTs has enabled their integration into GFRPs for self-sensing applications, further broadening their technological relevance[101–103].

Graphene and its derivates

Graphene is a single layer of graphitic carbon that can be synthesized via top-down or bottom-up approaches[104]. In top-down methods, graphene is typically exfoliated from graphite, offering relatively high yields. Conversely, bottom-up techniques rely on the controlled deposition of graphene onto substrates through processes such as chemical vapor deposition, plasma-enhanced CVD, or epitaxial growth on silicon carbide[105]. While these approaches allow precise control overgrowth and yield contamination-free graphene, they remain limited by low scalability and high production costs.

A critical challenge associated with graphene sheets is their intrinsic instability, as they tend to re-stack or agglomerate via van der Waals interactions to form graphite, the thermodynamically more stable structure. To overcome this issue, graphene can be derived from the reduction of graphene oxide (GO).

GO consists of single atomic layers of graphite decorated with oxygen-containing functional groups, distributed on basal planes and edges, resulting in a hybrid structure of sp^2 and sp^3 carbons. GO is commonly synthesized through the oxidation of graphite (or graphite oxide), where the introduction of oxygen functionalities facilitates exfoliation into monolayers by mild sonication or simple stirring. Although complete reduction of GO to pristine graphene is not achievable, the properties of graphene can be partially restored by reducing GO to reduced graphene oxide (rGO) (Figure 1.9).

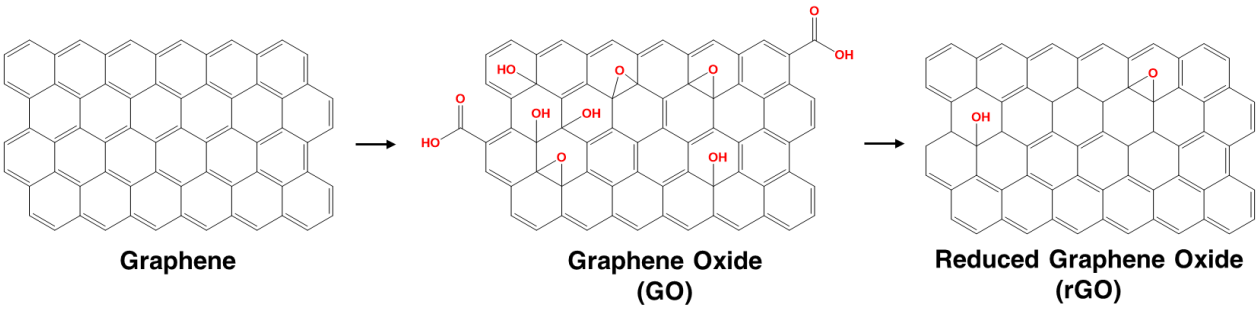

Figure 1.9 Schematic representation of the structure of graphene, GO and rGO[6].

The reduction of graphene oxide can be achieved by chemical, thermal, or electrochemical processes[106–109]. In thermal reduction, high temperatures under an inert atmosphere are required to prevent sample combustion. Chemical reduction is widely employed; however, common reductants such as hydrazine hydrate and sodium borohydride are hazardous, being both toxic and potentially explosive[110]. To address these limitations, recent research has focused on eco-friendly alternatives, including metals (e.g., zinc, iron, aluminum)[111–113], alkaline solutions (sodium or potassium hydroxides)[114], sugars (e.g., glucose, fructose, cellulose)[115,116], and other green substances[117,118]. Despite these advances, issues such as metal contamination and incomplete deoxygenation remain major challenges. Among the proposed options, L-ascorbic acid, a naturally occurring compound found in plants and food, has emerged as a particularly attractive green, effective, and low-cost reducing agent[119].

Due to its low density and high intrinsic strength, graphene is a promising filler in polymeric composites, imparting excellent mechanical performance[120–123]. Its most remarkable property is the extraordinary electrical conductivity, arising from its zero-bandgap semimetal nature, which makes it particularly suited for applications such as self-monitoring structural health systems, despite current cost limitations[124–126]. rGO, although inferior to pristine graphene due to residual structural defects and heteroatoms, is still highly valuable. It retains many of graphene's advantageous properties—such as good conductivity and mechanical reinforcement—and is already widely used in applications including sensors and structural composites. Several studies report rGO as an effective filler in glass fiber–reinforced polymers, enhancing their mechanical strength and electrical conductivity[127–129]. Moreover,

rGO-based GFRPs are being actively investigated for structural health monitoring, enabling the design of smart, lightweight materials with multifunctional properties[130–133].

1.3.2.2 Silica and silicates

Silica

Silica (SiO_2) nanoparticles have attracted considerable interest as nanofillers, owing to their versatility and their ability to enhance a broad spectrum of properties in polymer composites. In particular, SiO_2 NPs have unique physicochemical properties such as high thermal and chemical stability, tunable porosity, and hydroxyl groups enriched surface that can be functionalized with organic compounds to enhance compatibility between the inorganic filler and the organic polymer matrix, further improving the composite's performance[134].

Silica can be synthetized through top-down or bottom-up strategies. Top-down method reduces the bulk material's size via mechanical or chemical process, while bottom-up method involves the chemical synthesis starting from molecules or atoms. Among bottom-up approaches, the sol–gel process is one of the most widely employed, as it allows precise control over nanoparticle size, shape, porosity, and morphology through the careful adjustment of reaction parameters (e.g. temperature, pH, and the presence of templating agents). The Stöber's method[135] is a renowned process to synthesize silica nanoparticles with controlled and uniform size. The process is an ammonia-catalysed sol–gel reaction, where tetraethyl orthosilicate (TEOS) undergoes hydrolysis in the presence of water and a low-molecular-weight alcohol such as ethanol, followed by condensation to yield Si-O-Si bonds (Figure 1.10). The process is commonly catalysed by ammonia, leading to the formation of spherical nanoparticles with sizes ranging from ≈ 20 nm to several micrometres. The ability to precisely control particle size and morphology is crucial for tailoring the performance of silica-based nanocomposites.

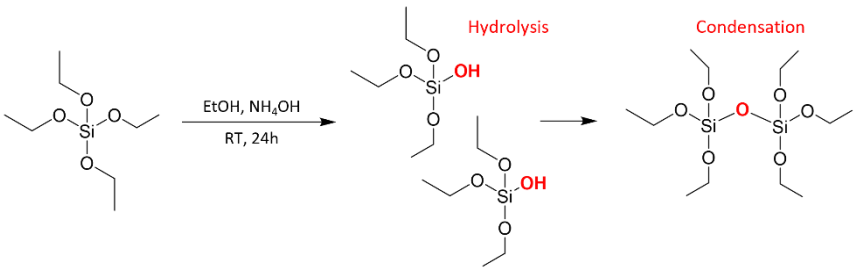

Figure 1.10 Stöber synthesis of SiO_2 NPs through hydrolysis and condensation of the precursor (TEOS).

Halloysite

An alternative class of silica-based materials is represented by clays, which are particularly attractive from a sustainability perspective due to their natural abundance and low cost. Depending on the

specific type of clay, these materials exhibit a combination of advantageous properties for adsorption applications, including high surface area, significant porosity, excellent mechanical strength, and notable chemical and thermal stability. The most widely employed clays are hydrated phyllosilicates, which can be described by the general chemical formula $(Ca, Na, H)(M)_2(Si, Al)_4O_{10}(OH)_2 \cdot nH_2O$, where M corresponds to metals such as aluminium, magnesium, iron, or zinc. Their structure is composed of alternating layers of tetrahedral SiO_4 units and octahedral AlO_6 or MO_6 units[136]. The classification of phyllosilicates is largely determined by the stacking arrangement of these layers:

- *1:1 Silicates*: each tetrahedral sheet is linked to a single octahedral sheet, forming alternating layered structures (e.g. kaolinite and halloysite).
- *2:1 Silicates*: two tetrahedral sheets are sandwiching on octahedral sheet, such as in montmorillonite, smectite, and vermiculite.

In the thesis work, Halloysite has been chosen, between the clays, as reinforcing inorganic filler for polymer composites. In fact, halloysite clay present exceptional physicochemical properties as high aspect ratio and mechanical strength, high hydrophilic due to hydroxyl groups on both inner and outer surfaces that can be used for further functionalization to enhance compatibility with a polymer matrix. The 1:1 layer structure has a single sheet of water molecules in-between with a spacing of 10.1 Å. Therefore, the clay has a hydrated form with a composition of $Al_2Si_2O_5(OH)_4 \cdot 2H_2O$ which irreversibly changes to a dehydrated form at relatively low temperatures or upon being directed to conditions of low relative humidity[137]. As represented in Figure 1.11, the structure is tubular and shows different groups at the surface: Al-OH are present in the internal surface while Si-OH in the external one, providing the possibility of a selective functionalization of the surfaces.

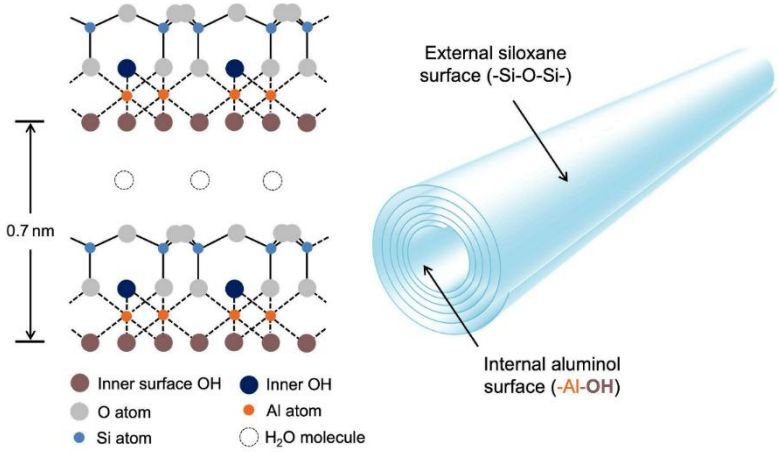

Figure 1.11 Structure of Halloysite clay[138].

1.4 Aims of the thesis

Considering this background, the principal aim of the thesis is to **develop and optimize filler materials able to impart self-healing and/or self-sensing properties to multifunctional polymer nanocomposites**.

In particular, the research activity has been articulated through **three main actions**:

1) The **preparation and exploitation in different polymer matrices of new class of hybrid filler**, **X@rGO, where X = SiO_2 NPs and Halloysite**, which synergistically combine the properties of ceramic and carbon-based materials. When embedded in an elastomer (e.g., **PDMS**), X@rGO not only acts as a reinforcing filler, but upon its loading exceeds the percolation threshold, a conductive network is established within the matrix, **enabling potential applications as a stretchable piezoresistive sensors**. Moreover, the incorporation of this hybrid filler into an **epoxy matrix used for the fabrication of GFRPs** enhances the fibre–matrix interfacial adhesion, leading to **improved mechanical properties**. Additionally, when a conductive network is established within the epoxy matrix, the material can function as an "**artificial neuron", enabling self-sensing capabilities**.

2) The **development of CNTs@ZnO hybrid filler for application** in **self-healable rubber composites**. The decoration of carbon nanotube's structure with zinc oxide nanoparticles (ZnO NPs) **imparts both reinforcement and self-healing properties**, through a reversible association-dissociation mechanism, to rubber carboxylated matrix (i.e. **XNBR**). Additionally, the high electrical conductivity of **CNTs**, when a **well-connected 3d network** is established inside the matrix, **leads to a multifunctional nanocomposite with self-healing and self-sensing properties**.

3) The **manufacturing and characterization of GFRPs incorporating carbon-based fillers**. Spray-coating the glass fiber surface with rGO units dispersed in an acrylic polymer (EMAA) **imparts electrical conductivity and extrinsic self-healing capability**, resulting in a **multifunctional nanocomposite** with both self-repairing and self-sensing properties.

References

[1] Alemán J V, Chadwick A V, He J, Hess M, Horie K, Jones RG, et al. Definitions of terms relating to the structure and processing of sols, gels, networks, and inorganic-organic hybrid materials (IUPAC Recommendations 2007). 2007;79(10):1801-1829. doi:10.1351/pac200779101801

[2] Sanchez C, Belleville P, Popall M, Nicole L. Applications of advanced hybrid organic–inorganic nanomaterials: from laboratory to market. *Chem Soc Rev*. 2011;40(2):696-753. doi:10.1039/C0CS00136H

[3] Judeinstein P, Sanchez C. Hybrid organic–inorganic materials: a land of multidisciplinarity. *J Mater Chem*. 1996;6(4):511-525. doi:10.1039/JM9960600511

[4] Kickelbick G. Introduction to Hybrid Materials. In: *Hybrid Materials*. ; 2006:1-48. doi:10.1002/9783527610495.ch1

[5] Sanchez C, Julián B, Belleville P, Popall M. Applications of hybrid organic–inorganic nanocomposites. *J Mater Chem*. 2005;15(35-36):3559-3592. doi:10.1039/B509097K

[6] Colombo M, Mostoni S, Fredi G, Rodricks C, Kalinka G, Riva M, et al. Interfacial Chemistry Behind Damage Monitoring in Glass Fiber-Reinforced Composites: Attempts and Perspectives. *Polym Compos*. Published online 2025:1-30. doi:10.1002/pc.70332

[7] Paleari L, Bragaglia M, Fabbrocino F, Nanni F. Structural Monitoring of Glass Fiber/Epoxy Laminates by Means of Carbon Nanotubes and Carbon Black Self-Monitoring Plies. *Nanomaterials*. 2021;11(6). doi:10.3390/nano11061543

[8] Sethi S, Ray BC. Environmental effects on fibre reinforced polymeric composites: Evolving reasons and remarks on interfacial strength and stability. *Adv Colloid Interface Sci*. 2015;217:43-67. doi:10.1016/j.cis.2014.12.005

[9] Al-Sabagh A, Taha E, Kandil U, Awadallah A, Nasr G abdelnaser M, Reda Taha M. Monitoring Moisture Damage Propagation in GFRP Composites Using Carbon Nanoparticles. *Polymers (Basel)*. 2017;9(3). doi:10.3390/polym9030094

[10] Singh S, Kamble Z, Neje G. Electro-mechanical behavior of self-sensing textile-reinforced composites for in situ structural health monitoring. *Journal of Reinforced Plastics and Composites*. Published online November 1, 2023. doi:10.1177/07316844231202370

[11] Cao C, Lin Z, Liu X, Jia Y, Saiz E, Wolf SE, et al. Strong Reduced Graphene Oxide Coated Bombyx mori Silk. *Adv Funct Mater*. 2021;31(34):2102923. doi:10.1002/adfm.202102923

[12] Cherrington R, Liang J. 2 - Materials and Deposition Processes for Multifunctionality. In: Goodship V, Middleton B, Cherrington R, eds. *Design and Manufacture of Plastic Components for Multifunctionality*. William Andrew Publishing; 2016:19-51. doi:10.1016/B978-0-323-34061-8.00002-8

[13] Ren X, Zou H, Diao Q, Wang C, Wang Y, Li H, et al. Surface modification technologies for enhancing the tribological properties of cemented carbides: A review. *Tribol Int*. 2023;180:108257. doi:10.1016/j.triboint.2023.108257

[14] Chen J, Wu J, Ge H, Zhao D, Liu C, Hong X. Reduced graphene oxide deposited carbon fiber reinforced polymer composites for electromagnetic interference shielding. *Compos Part A Appl Sci Manuf*. 2016;82:141-150. doi:10.1016/j.compositesa.2015.12.008

[15] Mahmood H, Vanzetti L, Bersani M, Pegoretti A. Mechanical properties and strain monitoring of glass-epoxy composites with graphene-coated fibers. *Compos Part A Appl Sci Manuf*. 2018;107:112-123. doi:10.1016/j.compositesa.2017.12.023

[16] Zhang H, Liu Y, Kuwata M, Bilotti E, Peijs T. Improved fracture toughness and integrated damage sensing capability by spray coated CNTs on carbon fibre prepreg. *Compos Part A Appl Sci Manuf*. 2015;70:102-110. doi:10.1016/j.compositesa.2014.11.029

[17] Vázquez-Moreno JM, Sánchez-Hidalgo R, Sanz-Horcajo E, Viña J, Verdejo R, López-Manchado MA. Preparation and Mechanical Properties of Graphene/Carbon Fiber-Reinforced Hierarchical Polymer Composites. *Journal of Composites Science*. 2019;3(1). doi:10.3390/jcs3010030

[18] Dibenedetto AT. Tailoring of interfaces in glass fiber reinforced polymer composites: a review. *Materials Science and Engineering*. 2001;302:74-82. doi:10.1016/S0921-5093(00)01357-5

[19] E.P. Plueddemann. *Silanes and Other Coupling Agents*. (K.L. Mittal, ed.). The Netherlands; 1992.

[20] Rodricks CW, Greenfeld I, Fiedler B, Wagner HD. Fragmentation of Beaded Fibres in a Composite. *Materials*. 2022;15(3). doi:10.3390/ma15030890

[21] Deng S, Ye L, Mai YW, Liu HY. Evaluation of fibre tensile strength and fibre/matrix adhesion using single fibre fragmentation tests. *Compos Part A Appl Sci Manuf*. 1998;29(4):423-434. doi:10.1016/S1359-835X(97)00094-8

[22] Martone A, Iacono S Dello, Zamani A, Lepore M, Sanguigno L, Maligno A, et al. Modelling of the micro-bond test for mechanical analysis of the fibre/matrix interphase in fibre reinforced plastics. *AIP Conf Proc*. 2019;2196(1):020041. doi:10.1063/1.5140314

[23] Pandey Gajendra, Kareliya Chirag H, Singh Raman P. A study of the effect of experimental test parameters on data scatter in microbond testing. *J Compos Mater*. 2011;46(3):275-284. doi:10.1177/0021998311410508

[24] Zarges JC, Kaufhold C, Feldmann M, Heim HP. Single fiber pull-out test of regenerated cellulose fibers in polypropylene: An energetic evaluation. *Compos Part A Appl Sci Manuf*. 2018;105:19-27. doi:10.1016/j.compositesa.2017.10.030

[25] Hampe A, Kalinka G, Meretz S, Schulz E. An advanced equipment for single-fibre pull-out test designed to monitor the fracture process. *Composites*. 1995;26(1):40-46. doi:10.1016/0010-4361(94)P3628-E

[26] Kalinka G, Leistner A, Hampe A. Characterisation of the fibre/matrix interface in reinforced polymers by the push-in technique. *Compos Sci Technol*. 1997;57(8):845-851. doi:10.1016/S0266-3538(96)00159-5

[27] Jäger J, Sause MGR, Burkert F, Moosburger-Will J, Greisel M, Horn S. Influence of plastic deformation on single-fiber push-out tests of carbon fiber reinforced epoxy resin. *Compos Part A Appl Sci Manuf*. 2015;71:157-167. doi:10.1016/j.compositesa.2015.01.011

[28] Lei Z, Luo G, Sun W, Dong Y, Tan Z, Wan Y, et al. Exploring the Iosipescu method to investigate interlaminar shear fatigue behavior and failure mechanisms of carbon fiber reinforced composites. *Int J Fatigue*. 2023;178:108020. doi:10.1016/j.ijfatigue.2023.108020

[29] Carlsson LA, D. F. A, and Pipes RB. Basic Experimental Characterization of Polymer Matrix Composite Materials. *Polymer Reviews*. 2013;53(2):277-302. doi:10.1080/15583724.2013.776588

[30] Herrera-Franco PJ, Drzal LT. Comparison of methods for the measurement of fibre/matrix adhesion in composites. *Composites*. 1992;23(1):2-27. doi:10.1016/0010-4361(92)90282-Y

[31] van der Zwaag S, Brinkman E. *Self Healing Materials : Pioneering Research in the Netherlands*. IOS Press; 2015.

[32] Utrera-Barrios S, Verdejo R, López-Manchado MÁ, Hernández Santana M. Self-Healing Elastomers: A sustainable solution for automotive applications. *Eur Polym J*. 2023;190:112023. doi:10.1016/j.eurpolymj.2023.112023

[33] Utrera-Barrios S, Verdejo R, López-Manchado MA, Hernández Santana M. Evolution of self-healing elastomers, from extrinsic to combined intrinsic mechanisms: a review. *Mater Horiz*. 2020;7(11):2882-2902. doi:10.1039/D0MH00535E

[34] Sattar MA, Patnaik A. Design Principles of Interfacial Dynamic Bonds in Self-Healing Materials: What are the Parameters? *Chem Asian J*. 2020;15(24):4215-4240. doi:10.1002/asia.202001157

[35] Li J, Zhang G, Sun R, Wong CP. A covalently cross-linked reduced functionalized graphene oxide/polyurethane composite based on Diels–Alder chemistry and its potential application in healable flexible electronics. *J Mater Chem C Mater*. 2017;5(1):220-228. doi:10.1039/C6TC04715G

[36] Zhang L, Qiu T, Sun X, Guo L, He L, Ye J, et al. Achievement of Both Mechanical Properties and Intrinsic Self-Healing under Body Temperature in Polyurethane Elastomers: A Synthesis Strategy from Waterborne Polymers. *Polymers (Basel)*. 2020;12(4). doi:10.3390/polym12040989

[37] Qin H, Zhang T, Li HN, Cong HP, Antonietti M, Yu SH. Dynamic Au-Thiolate Interaction Induced Rapid Self-Healing Nanocomposite Hydrogels with Remarkable Mechanical Behaviors. *Chem*. 2017;3(4):691-705. doi:10.1016/j.chempr.2017.07.017

[38] Fan W, Jin Y, Shi L, Zhou R, Du W. Developing visible-light-induced dynamic aromatic Schiff base bonds for room-temperature self-healable and reprocessable waterborne polyurethanes with high mechanical properties. *J Mater Chem A Mater*. 2020;8(14):6757-6767. doi:10.1039/C9TA13928A

[39] Liu Y, Liu Y, Wang Q, Han Y, Chen H, Tan Y. Doubly Dynamic Hydrogel Formed by Combining Boronate Ester and Acylhydrazone Bonds. *Polymers (Basel)*. 2020;12(2). doi:10.3390/polym12020487

[40] Guan Q, Lin G, Gong Y, Wang J, Tan W, Bao D, et al. Highly efficient self-healable and dual responsive hydrogel-based deformable triboelectric nanogenerators for wearable electronics. *J Mater Chem A Mater*. 2019;7(23):13948-13955. doi:10.1039/C9TA02711D

[41] Wu S, Yang Z, Fang S, Tang Z, Liu F, Guo B. Malleable organic/inorganic thermosetting hybrids enabled by exchangeable silyl ether interfaces. *J Mater Chem A Mater*. 2019;7(4):1459-1467. doi:10.1039/C8TA09866B

[42] Mohd Sani N, Majid N, Rehman A, Hayeemasae N, Radhakrishnan S, Kulkarni M, et al. A review of the recent development in self-healing rubbers and their quantification methods. *Progress in Rubber Plastics and Recycling Technology*. 2023;40:203-241. doi:10.1177/14777606231200952

[43] Hohlbein N, Shaaban A, Bras AR, Pyckhout-Hintzen W, Schmidt AM. Self-healing dynamic bond-based rubbers: understanding the mechanisms in ionomeric elastomer model systems. *Physical Chemistry Chemical Physics*. 2015;17(32):21005-21017. doi:10.1039/C5CP00620A

[44] Tant MR, Mauritz KA, Wilkes GL. *Ionomers: Synthesis, Structure, Properties and Applications*. Chapman & Hall; 1997.

[45] Schlick S. *Ionomers: Characterization, Theory, and Applications*. CRC Press; 1996.

[46] Varley R, Shen S, Zwaag S. The effect of cluster plasticisation on the self healing behaviour of ionomers. *Polymer (Guildf)*. 2010;51:679-686. doi:10.1016/j.polymer.2009.12.025

[47] Eisenberg A, Kim J, Ratner M. Introduction to Ionomers. *Phys Today*. 1999;52(2):68. doi:10.1063/1.882601

[48] Leibler L, Rubinstein M, Colby RH. Dynamics of reversible networks. *Macromolecules*. 1991;24(16):4701-4707. doi:10.1021/ma00016a034

[49] Fong KD, Self J, McCloskey BD, Persson KA. Ion Correlations and Their Impact on Transport in Polymer-Based Electrolytes. *Macromolecules*. 2021;54(6):2575-2591. doi:10.1021/acs.macromol.0c02545

[50] Low DYS, Supramaniam J, Goh BH, Manickam S, Tang SY. A Facile Scalable Strategy for Constructing Novel Robust Self-Healing Glove Utilizing Nanoreinforced Thermoreversible Carboxylated Nitrile Butadiene Rubber. *Adv Funct Mater*. 2024;34(33):2401345. doi:10.1002/adfm.202401345

[51] Utrera-Barrios S, Araujo-Morera J, Reyes L, Verdugo Manzanares R, Verdejo R, Lopez-Manchado M, et al. An effective and sustainable approach for achieving self-healing in nitrile rubber. *Eur Polym J*. 2020;139:110032. doi:10.1016/j.eurpolymj.2020.110032

[52] Nellesen A, von Tapavicza M, Bertling J, Schmidt A, Bold G, Speck T. Biomimetic self-healing elastomers. *Gummi, Fasern, Kunststoffe*. 2011;64:472-475.

[53] Das A, Sallat A, Böhme F, Suckow M, Basu D, Wießner S, et al. Ionic Modification Turns Commercial Rubber into a Self-Healing Material. *ACS Appl Mater Interfaces*. 2015;7(37):20623-20630. doi:10.1021/acsami.5b05041

[54] Xu C, Cao L, Huang X, Chen Y, Lin B, Fu L. Self-Healing Natural Rubber with Tailorable Mechanical Properties Based on Ionic Supramolecular Hybrid Network. *ACS Appl Mater Interfaces*. 2017;9(34):29363-29373. doi:10.1021/acsami.7b09997

[55] Shi J, Zhao N, Yan D, Song J, Fu W, Li Z. Design of a mechanically strong and highly stretchable thermoplastic silicone elastomer based on coulombic interactions. *J Mater Chem A Mater*. 2020;8(12):5943-5951. doi:10.1039/D0TA01593H

[56] Khalid MY, Al Rashid A, Arif ZU, Sheikh MF, Arshad H, Nasir MA. Tensile strength evaluation of glass/jute fibers reinforced composites: An experimental and numerical approach. *Results in Engineering*. 2021;10:100232. doi:10.1016/j.rineng.2021.100232

[57] T P S, Satheeshkumar S, Jesuarockiam N. Hybrid fiber reinforced polymer composites - A review. *Journal of Reinforced Plastics and Composites*. 2014;33:454–471. doi:10.1177/0731684413516393

[58] Kamarudin SH, Mohd Basri MS, Rayung M, Abu F, Ahmad S, Norizan MN, et al. A Review on Natural Fiber Reinforced Polymer Composites (NFRPC) for Sustainable Industrial Applications. *Polymers (Basel)*. 2022;14(17). doi:10.3390/polym14173698

[59] Thwe MM, Liao K. Durability of bamboo-glass fiber reinforced polymer matrix hybrid composites. *Compos Sci Technol*. 2003;63(3):375-387. doi:10.1016/S0266-3538(02)00225-7

[60] Agarwal BD, Broutman LJ, Chandrasghwkhara K. *Analysis and Performance of Fiber Composites*. Wiley; 2006.

[61] Nair AB, B Joseph RD. Eco-friendly bio-composites using natural rubber (NR) matrices and natural fiber reinforcements. In: *Chemistry, Manufacture and Applications of Natural Rubber*. ; 2014:249-283. doi:10.1533/9780857096913.2.249

[62] Miwa M, Horiba N. Effects of fibre length on tensile strength of carbon/glass fibre hybrid composites. *J Mater Sci*. 1994;29:973-977. doi:10.1007/BF00351419

[63] Chung DDL. *Carbon Fiber Composites*. Butterworth-Heinemann; 1994. https://www.sciencedirect.com/science/article/pii/B9780128044599000026

[64] Rajak DK, Pagar DD, Menezes PL, Linul E. Fiber-reinforced polymer composites: Manufacturing, properties, and applications. *Polymers (Basel)*. 2019;11(10). doi:10.3390/polym11101667

[65] Qureshi J. A Review of Recycling Methods for Fibre Reinforced Polymer Composites. *Sustainability*. 2022;14(24). doi:10.3390/su142416855

[66] Tao Y, Hadigheh SA, Wei Y. Recycling of glass fibre reinforced polymer (GFRP) composite wastes in concrete: A critical review and cost benefit analysis. *Structures*. 2023;53:1540-1556. doi:10.1016/j.istruc.2023.05.018

[67] Dong J, Chen M, Wang J. Recycling and optimum utilization of GFRP waste into low-carbon geopolymer paste for sustainable development. *Journal of Building Engineering*. 2024;97:110867. doi:10.1016/j.jobe.2024.110867

[68] Yıldız S, Karaağaç B, Güzeliş SG. Utilization of glass fiber reinforced polymer wastes. *Polym Compos*. 2021;42(1):412-423. doi:10.1002/pc.25834

[69] Avila A, Morais D. A multiscale investigation based on variance analysis for hand lay-up composite manufacturing. *Compos Sci Technol*. 2005;65:827-838. doi:10.1016/j.compscitech.2004.05.021

[70] Kim SJ, Pandey K, Poddar D, Yoo HM. In-situ fabrication of poly-l-lactide & its application as a glass fiber polymer composites using resin transfer molding. *Polym Compos*. n/a(n/a). doi:10.1002/pc.29167

[71] Kazmi SMR, Govignon Q, Bickerton S. Control of laminate quality for parts manufactured using the resin infusion process. *J Compos Mater*. 2018;53(3):327-343. doi:10.1177/0021998318783308

[72] Ricciardi MR, Antonucci V, Durante M, Giordano M, Nele L, Starace G, et al. A new cost-saving vacuum infusion process for fiber-reinforced composites: Pulsed infusion. *J Compos Mater*. 2013;48(11):1365-1373. doi:10.1177/0021998313485998

[73] Mertiny P, Ellyin F, Hothan A. An experimental investigation on the effect of multi-angle filament winding on the strength of tubular composite structures. *Compos Sci Technol*. 2004;64(1):1-9. doi:10.1016/S0266-3538(03)00198-2

[74] Miller AH, Dodds N, Hale JM, Gibson AG. High speed pultrusion of thermoplastic matrix composites. *Compos Part A Appl Sci Manuf*. 1998;29(7):773-782. doi:10.1016/S1359-835X(98)00006-2

[75] Wakeman MD, Cain TA, Rudd CD, Brooks R, Long AC. Compression moulding of glass and polypropylene composites for optimised macro- and micro- mechanical properties—1 commingled glass and polypropylene. *Compos Sci Technol*. 1998;58(12):1879-1898. doi:10.1016/S0266-3538(98)00011-6

[76] Denkena B, Horst P, Heimbs S, Schmidt C, Reichert L, Tiemann T. Automated fiber placement: The impact of manufacturing constraints on achieving structural property targets for CFRP-stiffeners. *Procedia CIRP*. 2023;118:845-850. doi:10.1016/j.procir.2023.06.145

[77] Oromiehie E, Prusty G, Compston P, Rajan G. Automated Fibre Placement based Composite Structures: Review on The Defects, Impacts and Inspections Techniques. *Compos Struct*. 2019;224:110987. doi:10.1016/j.compstruct.2019.110987

[78] Slanina Z. The Science and Technology of Carbon Nanotubes K. Tanaka, T. Yamabe, K. Fukui, Eds.: Elsevier Science, Amsterdam, 1999. *Fullerene Science and Technology*. 2000;8(6):639-640. doi:10.1080/10641220009351440

[79] Mittal G, Dhand V, Rhee KY, Park SJ, Lee WR. A review on carbon nanotubes and graphene as fillers in reinforced polymer nanocomposites. *Journal of Industrial and Engineering Chemistry*. 2015;21:11-25. doi:10.1016/j.jiec.2014.03.022

[80] Dai H, Wong EW, Lieber CM. Probing Electrical Transport in Nanomaterials: Conductivity of Individual Carbon Nanotubes. *Science (1979)*. 1996;272(5261):523-526. doi:10.1126/science.272.5261.523

[81] Bokobza L. Multiwall carbon nanotube elastomeric composites: A review. *Polymer (Guildf)*. 2007;48(17):4907-4920. doi:10.1016/j.polymer.2007.06.046

[82] Ali Z, Yaqoob S, Yu J, D'Amore A. Critical review on the characterization, preparation, and enhanced mechanical, thermal, and electrical properties of carbon nanotubes and their hybrid filler polymer composites for various applications. *Composites Part C: Open Access*. 2024;13:100434. doi:10.1016/j.jcomc.2024.100434

[83] Sisto T, Zakharov L, White B, Jasti R. Towards Pi-Extended Cycloparaphenylenes as Seeds for CNT Growth: Investigating Strain Relieving Ring-Openings and Rearrangements. *Chem Sci*. 2016;7. doi:10.1039/C5SC04218F

[84] Boumia L, Zidour M, Benzair A, Tounsi A. A Timoshenko beam model for vibration analysis of chiral single-walled carbon nanotubes. *Physica E Low Dimens Syst Nanostruct*. 2014;59:186–191. doi:10.1016/j.physe.2014.01.020

[85] Lekawa-Raus A, Patmore J, Kurzepa L, Bulmer J, Koziol K. Electrical Properties of Carbon Nanotube Based Fibers and Their Future Use in Electrical Wiring. *Adv Funct Mater*. 2014;24(24):3661-3682. doi:10.1002/adfm.201303716

[86] Bhushan Kumar D, Popli G. Carbon Nanotubes and Its Applications: A Review. *IJRASET*. 2015;3(7).

[87] Anazawa K, Shimotani K, Manabe C, Watanabe H, Shimizu M. High-purity carbon nanotubes synthesis method by an arc discharging in magnetic field. *Appl Phys Lett*. 2002;81(4):739-741. doi:10.1063/1.1491302

[88] Arora N, Sharma NN. Arc discharge synthesis of carbon nanotubes: Comprehensive review. *Diam Relat Mater*. 2014;50:135-150. doi:10.1016/j.diamond.2014.10.001

[89] Journet C, Maser WK, Bernier P, Loiseau A, de la Chapelle ML, Lefrant S, et al. Large-scale production of single-walled carbon nanotubes by the electric-arc technique. *Nature*. 1997;388(6644):756-758. doi:10.1038/41972

[90] Bethune DS, Kiang CH, de Vries MS, Gorman G, Savoy R, Vazquez J, et al. Cobalt-catalysed growth of carbon nanotubes with single-atomic-layer walls. *Nature*. 1993;363(6430):605-607. doi:10.1038/363605a0

[91] Thess A, Lee R, Nikolaev P, Dai H, Petit P, Robert J, et al. Crystalline Ropes of Metallic Carbon Nanotubes. *Science (1979)*. 1996;273(5274):483-487. doi:10.1126/science.273.5274.483

[92] Muñoz E, Maser WK, Benito AM, Martínez MT, de la Fuente GF, Righi A, et al. Single-walled carbon nanotubes produced by cw CO2-laser ablation: study of parameters important for their formation. *Applied Physics A*. 2000;70(2):145-151. doi:10.1007/s003390050026

[93] Su M, Zheng B, Liu J. A scalable CVD method for the synthesis of single-walled carbon nanotubes with high catalyst productivity. *Chem Phys Lett*. 2000;322(5):321-326. doi:10.1016/S0009-2614(00)00422-X

[94] Maruyama S, Kojima R, Miyauchi Y, Chiashi S, Kohno M. Low-temperature synthesis of high-purity single-walled carbon nanotubes from alcohol. *Chem Phys Lett*. 2002;360(3):229-234. doi:10.1016/S0009-2614(02)00838-2

[95] Meyyappan M, Delzeit L, Cassell A, Hash D. Carbon nanotube growth by PECVD: a review. *Plasma Sources Sci Technol*. 2003;12(2):205-216. doi:10.1088/0963-0252/12/2/312

[96] Hirlekar RS, Yamagar M, Garse H, Vij M, Kadam VJ, Vidyapeeth B. Carbon Nanotubes and its applications: A review. *Asian Journal of Pharmaceutical and Clinical Research*. 2009;2(4).

[97] Saifuddin N, Raziah AZ, Junizah AR. Carbon Nanotubes: A Review on Structure and Their Interaction with Proteins. *J Chem*. 2013;2013(1):676815. doi:10.1155/2013/676815

[98] SURIANI AB, MD NOR R, RUSOP M. Vertically aligned carbon nanotubes synthesized from waste cooking palm oil. *Journal of the Ceramic Society of Japan*. 2010;118(1382):963-968. doi:10.2109/jcersj2.118.963

[99] Panchagnula KK, Kuppan P. Improvement in the mechanical properties of neat GFRPs with multi-walled CNTs. *Journal of Materials Research and Technology*. 2019;8(1):366-376. doi:10.1016/j.jmrt.2018.02.009

[100] Kim GY, Lee G, Yu WR. Carbon-nanotube-grafted glass-fiber-reinforced composites: Synthesis and mechanical properties. *Heliyon*. 2024;10(9). doi:10.1016/j.heliyon.2024.e30262

[101] Zhang H, Bilotti E, Peijs T. The use of carbon nanotubes for damage sensing and structural health monitoring in laminated composites: a review. *Nanocomposites*. 2015;1(4):167-184. doi:10.1080/20550324.2015.1113639

[102] Bhandari M, Wang J, Jang D, Nam I, Huang B. A Comparative Study on the Electrical and Piezoresistive Sensing Characteristics of GFRP and CFRP Composites with Hybridized Incorporation of Carbon Nanotubes, Graphenes, Carbon Nanofibers, and Graphite Nanoplatelets. *Sensors*. 2021;21(21). doi:10.3390/s21217291

[103] Sbarufatti C, Patel B, Fernández X, Scaccabarozzi D, Cinquemani S, Jiménez-Suárez A, et al. Self-sensing of CNT-Doped GFRP Panels During Impact and Compression After Impact Tests. In: ; 2021:527-536. doi:10.1007/978-3-030-64908-1_49

[104] Dreyer DR, Park S, Bielawski CW, Ruoff RS. The chemistry of graphene oxide. *Chem Soc Rev*. 2010;39(1):228-240. doi:10.1039/B917103G

[105] Gutiérrez-Cruz A, Ruiz-Hernández AR, Vega-Clemente JF, Luna-Gazcón DG, Campos-Delgado J. A review of top-down and bottom-up synthesis methods for the production of graphene, graphene oxide and reduced graphene oxide. *J Mater Sci*. 2022;57(31):14543-14578. doi:10.1007/s10853-022-07514-z

[106] Zhou A, Bai J, Hong W, Bai H. Electrochemically reduced graphene oxide: Preparation, composites, and applications. *Carbon N Y*. 2022;191:301-332. doi:10.1016/j.carbon.2022.01.056

[107] Huang L, Zhu P, Li G, Lu D, Sun R, Wong CP. Core–shell SiO 2 @RGO hybrids for epoxy composites with low percolation threshold and enhanced thermo-mechanical properties. *J Mater Chem A*. 2014;2:18246-18255. doi:10.1039/C4TA03702B

[108] Park S, An J, Potts JR, Velamakanni A, Murali S, Ruoff RS. Hydrazine-reduction of graphite- and graphene oxide. *Carbon N Y*. 2011;49(9):3019-3023. doi:10.1016/j.carbon.2011.02.071

[109] De Silva KKH, Huang HH, Yoshimura M. Progress of reduction of graphene oxide by ascorbic acid. *Appl Surf Sci*. 2018;447:338-346. doi:10.1016/j.apsusc.2018.03.243

[110] Fathy M, Gomaa A, Taher FA, El-Fass MM, Kashyout AEHB. Optimizing the preparation parameters of GO and rGO for large-scale production. *J Mater Sci*. 2016;51(12):5664-5675. doi:10.1007/s10853-016-9869-8

[111] Yang S, Yue W, Huang D, Chen C, Lin H, Yang X. A facile green strategy for rapid reduction of graphene oxide by metallic zinc. *RSC Adv*. 2012;2(23):8827-8832. doi:10.1039/C2RA20746J

[112] Fan ZJ, Kai W, Yan J, Wei T, Zhi LJ, Feng J, et al. Facile Synthesis of Graphene Nanosheets via Fe Reduction of Exfoliated Graphite Oxide. *ACS Nano*. 2011;5(1):191-198. doi:10.1021/nn102339t

[113] Fan Z, Wang K, Wei T, Yan J, Song L, Shao B. An environmentally friendly and efficient route for the reduction of graphene oxide by aluminum powder. *Carbon N Y*. 2010;48(5):1686-1689. doi:10.1016/j.carbon.2009.12.063

[114] Fan X, Peng W, Li Y, Li X, Wang S, Zhang G, et al. Deoxygenation of Exfoliated Graphite Oxide under Alkaline Conditions: A Green Route to Graphene Preparation. *Advanced Materials*. 2008;20(23):4490-4493. doi:10.1002/adma.200801306

[115] Zhu C, Guo S, Fang Y, Dong S. Reducing Sugar: New Functional Molecules for the Green Synthesis of Graphene Nanosheets. *ACS Nano*. 2010;4(4):2429-2437. doi:10.1021/nn1002387

[116] Peng H, Meng L, Niu L, Lu Q. Simultaneous Reduction and Surface Functionalization of Graphene Oxide by Natural Cellulose with the Assistance of the Ionic Liquid. *The Journal of Physical Chemistry C*. 2012;116(30):16294-16299. doi:10.1021/jp3043889

[117] Fernández-Merino MJ, Guardia L, Paredes JI, Villar-Rodil S, Solís-Fernández P, Martínez-Alonso A, et al. Vitamin C Is an Ideal Substitute for Hydrazine in the Reduction of Graphene Oxide Suspensions. *The Journal of Physical Chemistry C*. 2010;114(14):6426-6432. doi:10.1021/jp100603h

[118] Bose S, Kuila T, Mishra AK, Kim NH, Lee JH. Dual role of glycine as a chemical functionalizer and a reducing agent in the preparation of graphene: an environmentally friendly method. *J Mater Chem*. 2012;22(19):9696-9703. doi:10.1039/C2JM00011C

[119] Migliavacca A, Latorrata S, Gallo Stampino P, Dotelli G. Preparation and characterization of graphene oxide based membranes as possible Gas Diffusion Layers for PEM fuel cells with enhanced surface homogeneity. *Mater Today Proc*. 2017;4(11, Part 2):11594-11607. doi:10.1016/j.matpr.2017.09.071

[120] Veerakumar VGS, Shanmugavel BP, Harish S. On the Influence of the Functionalization of Graphene Nanoplatelets and Glass Fiber on the Mechanical Properties of GFRP Composites. *Applied Composite Materials*. 2021;28(4):1127-1152. doi:10.1007/s10443-021-09908-9

[121] Topkaya T, Çelik YH, Kilickap E. Mechanical properties of fiber/graphene epoxy hybrid composites. *Journal of Mechanical Science and Technology*. 2020;34(11):4589-4595. doi:10.1007/s12206-020-1016-4

[122] Malik K, Ahmad F, Yunus NA, Megat-Yusoff P, Beh HG, Nosbi N, et al. *The Effects of Graphene Hybridization on Mechanical Properties of GFRP Composites*. Vol 2401.; 2021. doi:10.1063/5.0072598

[123] Shabberhussain S, Ramachandran V. Effect of Graphene Nanoplatelets on Mechanical Performance of GFRP Composites. *Materials Science Forum*. 2022;1059:73-80. doi:10.4028/p-dm021j

[124] Anas M, Nasir MA, Asfar Z, Nauman S, Akalin M, Ahmad F. Structural health monitoring of GFRP laminates using graphene-based smart strain gauges. *Journal of the Brazilian Society of Mechanical Sciences and Engineering*. 2018;40(8):397. doi:10.1007/s40430-018-1320-4

[125] Wang Q, Tian Y, Duongthipthewa A, Zhang J, Liu M, Su Z, et al. An embedded non-intrusive graphene/epoxy broadband nanocomposite sensor co-cured with GFRP for in situ structural health monitoring. *Compos Sci Technol*. 2023;236:109995. doi:10.1016/j.compscitech.2023.109995

[126] Mirabedini A, Ang A, Nikzad M, Fox B, Lau KT, Hameed N. Evolving Strategies for Producing Multiscale Graphene-Enhanced Fiber-Reinforced Polymer Composites for Smart Structural Applications. *Advanced Science*. 2020;7(11):1903501. doi:10.1002/advs.201903501

[127] Kesarwani S, Verma RK, Jayswal SC, Khare P. Investigation of physiochemical and mechanical properties of reduced graphene oxide (rGO) modified carbon fiber polymer composites. *The Journal of The Textile Institute*. 2024;115(2):188-200. doi:10.1080/00405000.2023.2200348

[128] Rafiee M, Nitzsche F, Laliberte J, Hind S, Robitaille F, Labrosse MR. Thermal properties of doubly reinforced fiberglass/epoxy composites with graphene nanoplatelets, graphene oxide and reduced-graphene oxide. *Compos B Eng*. 2019;164:1-9. doi:10.1016/j.compositesb.2018.11.051

[129] Singh SK, Nayak B, Singh TJ, Halder S. Investigating the role of synthesized reduced graphene oxide and graphite micro-fillers on mechanical and fretting wear performance of glass fiber epoxy-based composite. *High Perform Polym*. 2023;35(9):946-962. doi:10.1177/09540083231196087

[130] Bathusha MSS, Din IU, Umer R, Khan KA. In-situ monitoring of crack growth and fracture behavior in composite laminates using embedded sensors of rGO coated fabrics and GnP paper. *Sens Actuators A Phys*. 2024;365:114850. doi:10.1016/j.sna.2023.114850

[131] Nisha MS, Venthan SM, Rangasamy G, Sam DP, Akilesh G, Bhaskar DS, et al. Fabrication and testing of rGO-PVDF nanosensing sheets on glass fibre-reinforced polymer for structural health monitoring in aerospace engineering. *Appl Nanosci*. 2023;13(9):5935-5947. doi:10.1007/s13204-023-02866-7

[132] Górski M, Safuta M. Functional carbon-based materials for structural health monitoring and protection of concrete structures. *Structural Concrete*. 2024;26(5). doi:https://doi.org/10.1002/suco.202400841

[133] Fu YF, Li YQ, Liu YF, Huang P, Hu N, Fu SY. High-Performance Structural Flexible Strain Sensors Based on Graphene-Coated Glass Fabric/Silicone Composite. *ACS Appl Mater Interfaces*. 2018;10(41):35503-35509. doi:10.1021/acsami.8b09424

[134] Lee D, Yoo B. Advanced Silica/Polymer Composites: Materials and Applications. *Journal of Industrial and Engineering Chemistry*. 2016;38. doi:10.1016/j.jiec.2016.04.016

[135] Stöber W, Fink A, Bohn E. Controlled growth of monodisperse silica spheres in the micron size range. *J Colloid Interface Sci*. 1968;26(1):62-69. doi:10.1016/0021-9797(68)90272-5

[136] Uddin F. Clays, Nanoclays, and Montmorillonite Minerals. *Clay, nanoclay and montmorillonite minerals Metallurgical and Materials Transactions A*. 2008;Volume 39:2804-2814. doi:10.1007/s11661-008-9603-5

[137] Kumari N, Mohan C. Basics of Clay Minerals and Their Characteristic Properties. In: ; 2021. doi:10.5772/intechopen.97672

[138] Halloysite Clay Nanotubes. Available from https://phantomplastics.com/functional-fillers/halloysite-filler-gives-unique-properties-to-plastics-and-coatings/.

2. Smart nanocomposite with Hybrid filler X@rGO

In this chapter, the synthesis, characterization, and functional evaluation of a smart nanocomposite systems based on hybrid fillers (X@rGO) are presented. The hybrid fillers were developed by combining inorganic NPs (SiO_2 or Halloysite) with reduced graphene oxide (rGO) to integrate the structural, mechanical, and electrical advantages of both components; these were then embedded in PDMS-based smart composites to impart enhanced mechanical and electrical properties to the resulting nanocomposites for future self-sensing applications.

Section 2.1 describes the preparation and characterisation of the pristine inorganic materials. Silica NPs were synthesised via the Stöber method, while commercial halloysite nanotubes were used as received. Their morphology, texture, and thermal stability were analysed through different techniques. In the following Section 2.2, the synthesis of the hybrid materials (X@rGO) is detailed. The synthesis pathway involved three main steps: (i) surface functionalization of the inorganic phase with 3-aminopropyltriethoxysilane (APTES), (ii) attachment of graphene oxide (GO), and (iii) thermal reduction to obtain rGO. Different characterization analyses were employed to confirm successful grafting, assess the degree of reduction, and evaluate morphological changes. These analyses provided insights into the interfacial interactions between the inorganic phase and the rGO sheets. Section 2.3 discusses the incorporation of the hybrid fillers into a PDMS matrix to assess their functional behaviour in polymer nanocomposites. The resulting materials were analysed for their mechanical, thermal, and dielectric properties, highlighting how the presence of rGO-modified fillers influences crosslinking dynamics, conductivity, and interfacial polarization phenomena. Section 2.4 reports the manufacturing process of GFRPs with SiO_2@rGO embedded in the matrix. Firstly, GF were coated with silica layer and the effective coating confirmed with a morphological analysis (SEM). Then, single fiber push-out tests were performed to evaluate interfacial shear strength (IFSS) when the hybrid filler SiO_2@rGO is dispersed in the matrix. At the end, Section 2.5 summarizes all the results reported in the Chapter.

2.1 Preparation of naked fillers

The preparation of the hybrid filler (X@rGO) involved two different inorganic fillers (X = SiO_2, Halloysite) that were used as support. For SiO_2 NPs synthesis, the Stöber's method[1] has been employed (as reported in Section 1.3.2.2). The process is an ammonia-catalysed sol–gel reaction where the silica precursor (i.e. tetraethyl orthosilicate, TEOS) undergoes hydrolysis and further condensation to form NPs with controlled size and shape. For Halloysite, a commercial nanoclay has been purchased by Sigma-Aldrich and utilized as received.

2.1.1 Experimental procedure of SiO_2 NPs

Materials

Tetraethyl orthosilicate (TEOS, ≥99%) and ammonia solution (NH_4OH, 25 %) were purchased from Sigma-Aldrich. Ethanol (EtOH, ≥99.8%) was purchased from Carlo Erba.

Synthesis

A two-neck round-bottom flask was charged with 484 mL of EtOH and 26.8 mL of NH_4OH solution. The solution was stirred at 700 rpm at RT and 25.75 mL of TEOS has been added dropwise to the reaction flask. The reaction has been stirred for 24 hours at RT. The resulting product was isolated by centrifugation at 9000 rpm for 30 minutes and washed two times with ethanol and one time with distilled water. The final product was dried overnight in an oven at 80 °C.

2.1.2 Characterization of SiO_2 NPs

TEM analysis

TEM analysis has been conducted to study the morphological features of the synthetized spherical silica NPs. As shown in Figure 2.1, the SiO_2 NPs present a homogeneous distribution of the shape and dimensions with a diameter of 70 ± 4 nm.

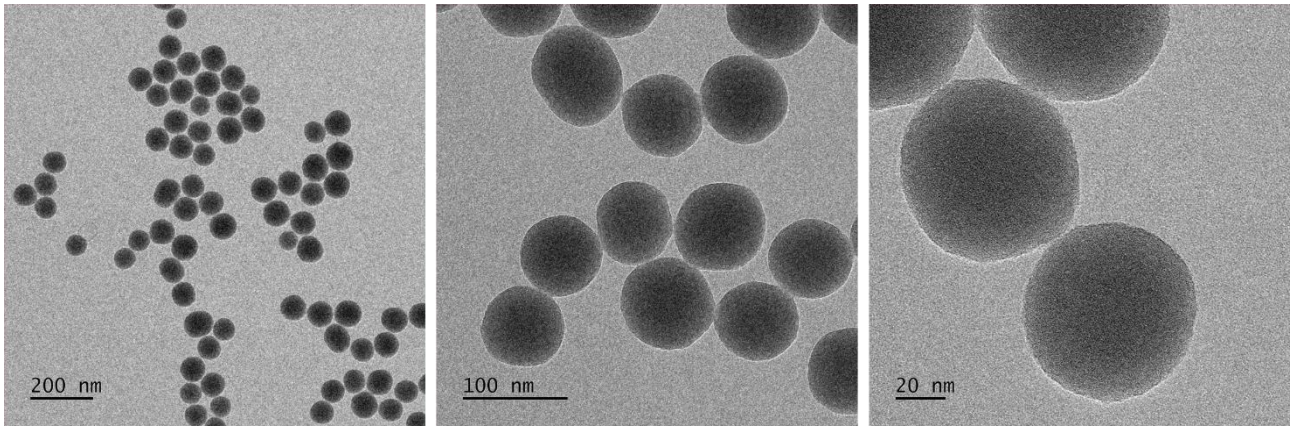

Figure 2.1 TEM micrographs at different magnitudes of Silica NPs.

Nitrogen physisorption

The nitrogen adsorption–desorption isotherm (77 K) was recorded for the SiO_2 NPs. As shown in Figure 2.2a, the isotherm exhibits characteristics of a type IV with a H3 hysteresis at high relative pressure, according to IUPAC classification[2]. This type of isotherm suggests a structure with a limited amount of mesopores. Moreover, for values of $p/p_0 > 0.8$, there is a significant increase in adsorbed volume ascribable to the filling of interparticle spaces. The specific surface area (SSA) and the pore volume have been calculated with a Brunauer–Emmett–Teller (BET) and Barrett-Joyner-Halenda (BJH) models and the values are 64 ± 3 $m^2 g^{-1}$ and 0.425 cc g^{-1} respectively.

The pore size distribution, derived from the BJH model applied uniquely to the desorption curve, reveals distribution centred around at 34.8 nm, as shown in Figure 2.2b. In other words, the mesoporous features observed in the type IV isotherm are likely associated with interparticle voids generated by aggregation, indicating that the NPs tend to exist in an aggregated state.

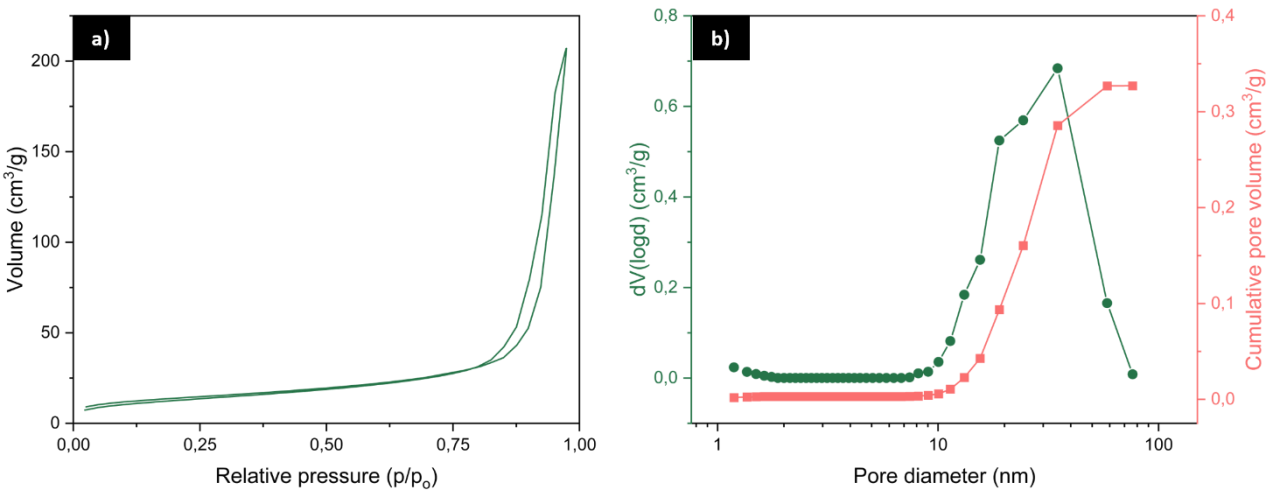

Figure 2.2 a) Nitrogen adsorption-desorption (77K) isotherm of SiO_2 NPs; b) Cumulative pore volume and pore size distribution curves of SiO_2 NPs calculated by BJH model for mesoporous analysis.

TGA

The TGA analysis has been employed to determine the number of hydroxyl groups available on the silica surface. This is particularly relevant to calculate the amount of APTES necessary for a good coverage of the NPs during the surface functionalization process (Figure 2.3). In fact, these groups represent the site of condensation of the silane molecules over the silica particles. The thermogram of bare SiO_2 generally shows two main steps of weight loss: the first step between 30 and 150 °C is related to the loss of water/solvent molecules adsorbed on the surface. The second mass loss observed between 150 and 1000 °C is associated to the decomposition or desorption of surface-bound OH groups (OH_{sup}) covalently bonded over the silica surface. Thus, the moles of OH_{sup} groups per gram of SiO_2 NPs is 5.32 mmol g^{-1}, calculated with the Equations A.18 provided in the appendix.

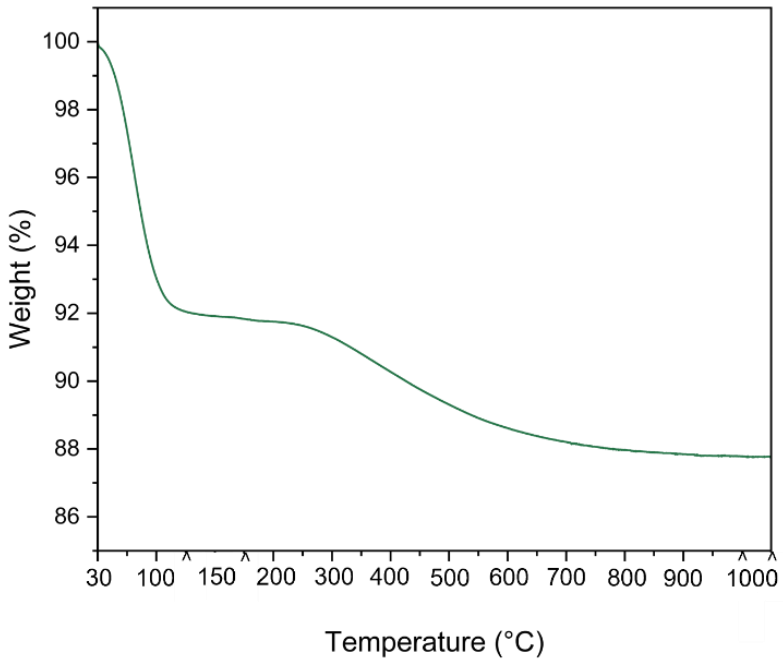

Figure 2.3 TGA thermogram of SiO_2 NPs.

2.1.2 Characterization of Halloysite

TEM analysis

The morphological characterization of Halloysite has been performed by TEM analysis (Figure 2.4). In detail, the filler exhibits a tubular structure with a diameter of 45 ± 15 nm and a length ranging from 500 nm to 2 µm, consistent with the Technical Data Sheet provided by Sigma Aldrich (i.e. 30-70 nm and 1-3 µm, respectively).

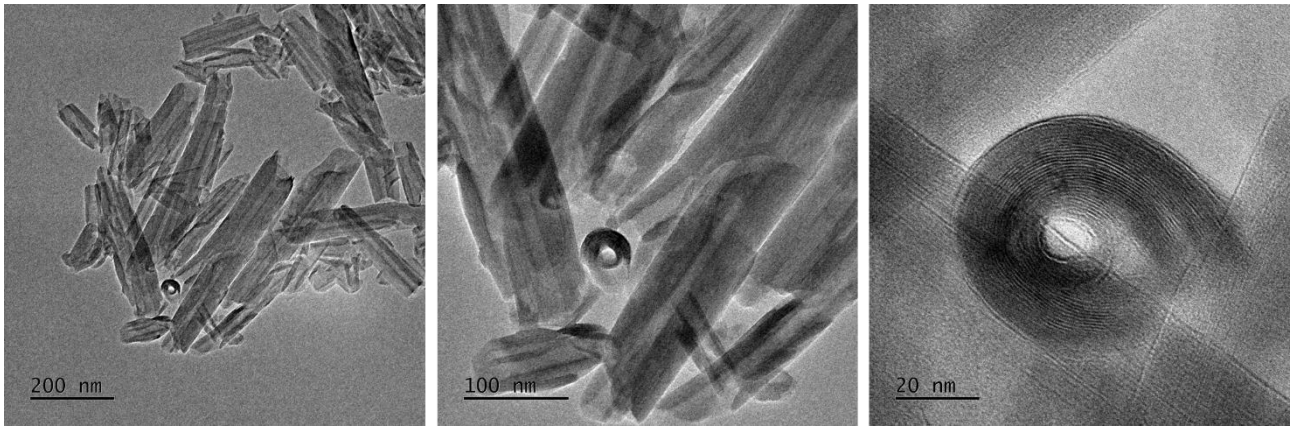

Figure 2.4 TEM images at different magnitudes of commercial Halloysite nanoclay.

Nitrogen physisorption

The nitrogen adsorption–desorption isotherm (77 K) was recorded for commercial Halloysite nanoclay. As shown in Figure 2.5a, the isotherm exhibits the typical features of a type IV isotherm with H3 hysteresis at high relative pressure. This isotherm indicates the presence of a limited fraction of mesopores. Furthermore, at relative pressures (p/p_0) above 0.8, the pronounced rise in adsorbed volume can be attributed to the filling of interparticle voids.

The specific surface area (SSA), calculated with BET model, is 59 ± 4 $m^2\ g^{-1}$ consistent with the value provided from the Technical Data Sheet (i.e. SSA 64 $m^2\ g^{-1}$). On the other side, the pore volume, calculated with BJH method, is 0.530 cc g^{-1}, lower than the known value of 1.26-1.34 mL g^{-1}. This phenomenon can be explained following the curves shown in Figure 2.5b. In fact, during the analysis, the instrument could not fill all the pores and reach a plateau for the cumulative pore volume, probably because of the presence of macropores deriving from the aggregation of the tubular structure of the halloysite.

Moreover, a "cavitation" phenomenon can be observed (black arrow, Figure 2.5a) at ≈ 0.46 p/p_0, which occurs during the desorption process in ink-bottled-shape pores[3]. In these pores, as the pressure is reducing, the condensed gas may suddenly vaporize inside the cavity and subsequently collapse. This

results in an artificial feature in the desorption isotherm and an ambiguous pore size distribution. Such cavitation does not correspond to a real pore size and can mask the actual desorption process. In this case the artificial peak is the one at 3.7 nm, that can be calculated, starting from the relative pressure value of cavitation in the isotherm, following the Kelvin Equation which relates the relative pressure to pore radius (Equation 2.1):

$$\ln \frac{p}{p_0} = -\frac{2\gamma V_m}{rRT} \qquad \text{Eq.2.1}$$

where γ is the surface tension of liquid nitrogen, V_m is the molar volume of N_2, R is the gas constant, T is the temperature and r is the pore radius[4].

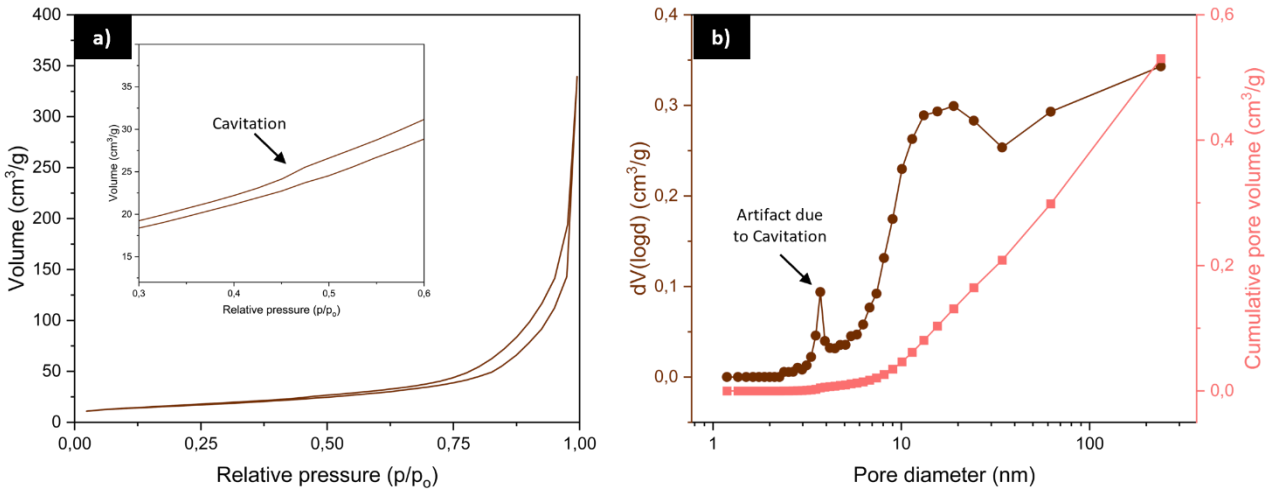

Figure 2.5 a) Nitrogen adsorption-desorption (77K) isotherms of commercial Halloysite; b) Cumulative pore volume and pore size distribution curves of Halloysite calculated by BJH model for mesoporous analysis.

TGA

Differently from silica nanoparticles, the TGA analysis of the halloysite cannot be used to evaluate the number of hydroxyl groups on the surface to further calculate the moles of APTES (Figure 2.6). In fact, the mass loss between 150 and 1000 °C is associated to the decomposition or desorption of surface-bound OH groups, but in the same step there's the elimination of the water trapped in the structure of the tubular filler. Therefore, the number of OH_{sup} groups per unit area, considering all the $\Delta wt.\%_{\,150-1000°C}$ as surface hydroxyl groups, would be vastly overestimated. Consequently, the quantity of APTES to add would be greater than necessary involving its self-condensation to silica, undermining the success of the functionalization.

For this reason, a study of different stoichiometric ratio between the hypothetical moles of OH_{sup} and the moles of APTES has been conducted (see Section 2.2.3).

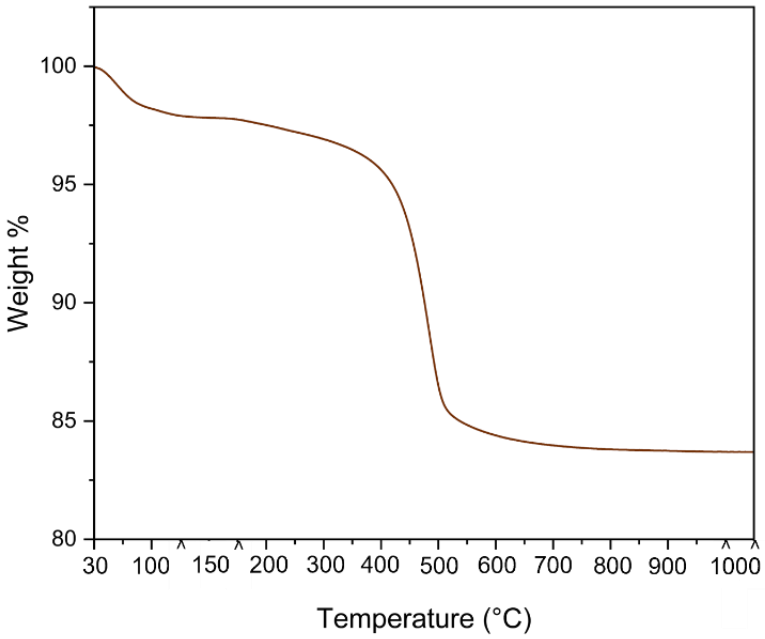

Figure 2.6 TGA thermogram of commercial Halloysite nanoclay.

2.2 Synthesis of X@rGO

In this section, the synthesis and characterization of the hybrid filler X@rGO have been widely described. The synthesis process can be divided in three steps as shown in Scheme 2.1.

The first step is the surface functionalization with APTES. Starting from the number of OH_{sup} of bare silica NPs (calculated from the TGA curve, Figure 2.3), the moles of APTES per gram of SiO_2 were calculated in a stoichiometric ratio 2:1. In the case of halloysite, a deep study is necessary to understand the right amount of organ silane to use in the functionalization reaction. In particular, the OH_{sup} (mol g^{-1}) cannot be determined for this type of filler because during the TGA analysis, the water trapped in the structure is lost in the same range of temperatures used for the calculation too. The chosen one was 2:1 (mol_{OH} g^{-1} : mol_{APTES} g^{-1}), assuming that only half of the weight loss between 150-1000 °C is due to the available OH_{sup} (see Section 2.2.3).

The second step of the process is the attachment of graphene oxide in water solution through electrostatic interactions between the amine groups of the APTES and the oxygenated groups of GO (i.e. carboxylic, epoxydic and carbonylic groups)[5].

Lastly, the third step involves the reduction of the filler to eliminate the oxygenated groups of GO in order to obtain the final hybrid filler X@rGO with an increased electrical conductivity.

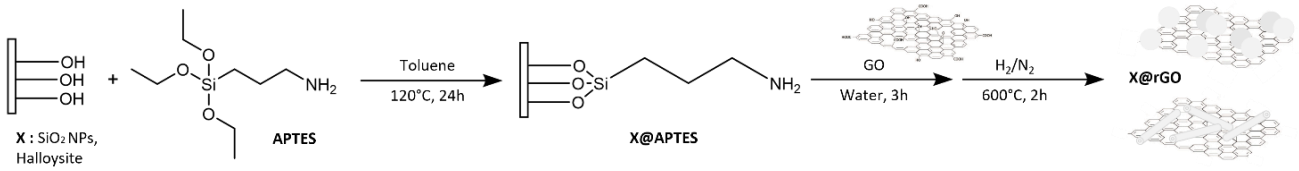

Scheme 2.1 Scheme reaction of the hybrid filler (X@rGO) synthesis.

2.2.1 Experimental procedure of X@rGO

Materials

Halloysite nanoclay was purchased from Sigma-Aldrich. 3-Aminopropryltriethoxysilane (APTES, 98 %) was purchased from abcr. Graphene oxide (GO) water dispersion (0.4 wt.%) was purchased from Graphenea. Toluene (99 %) was purchased from Thermo Fisher Scientific. Ethanol (EtOH, ≥ 99.8 %) was purchased from Carlo Erba.

Synthesis

In a two-neck round-bottom flask, 5.0 g of X (i.e. SiO_2 NPs or commercial halloysite) were dispersed in 120 mL of toluene using an ultrasonic bath for 5 minutes, and the temperature mixture was brought to 120 °C through a silicon oil bath. APTES (2.96 mL for SiO_2, 5.56 mL for halloysite) was added dropwise, and the reaction mixture was stirred for 24 hours under reflux. The resulting product (X@APTES) was isolated by centrifugation, washed two times with toluene (9000 rpm, 20 min) and one time with ethanol (9000 rpm, 30 min) and dried in an oven at 80 °C overnight.

In a one-neck round-bottom flask, 5.0 g of X@APTES were dispersed in 250 mL distilled water using an ultrasonic bath for 15 minutes. 25 mL of GO solution (0.1 g, 2 wt.% of X@APTES) was dispersed in a beaker with 250 mL of distilled water by ultrasonication for 20 minutes. The GO dispersion was added dropwise to the X@APTES dispersion under stirring. The reaction mixture was sonicated for 15 minutes and then stirred for 1 hour. The resulting product (X@GO) was isolated by centrifugation at 9000 rpm for 30 minutes and washed two times with distilled water. The final product was dried overnight in an oven at 80°C.

To obtain the reduction of GO to rGO, the product (X@GO) has been treated for 2 hours at 600 °C in a 5 % H_2/N_2 reducing atmosphere with a heating rate of 5 °C min^{-1}. The final product has been recovered and named X@rGO.

2.2.2 Characterization of SiO_2@rGO

TGA and CHNS

The TGA analysis has been used to evaluate the degree of functionalization of SiO_2 with APTES and, secondly, to quantify r-GO in the hybrid filler SiO_2@rGO. The TGA thermographs of each product of the synthesis steps (i.e. SiO_2, SiO_2@APTES, SiO_2@GO and SiO_2@rGO) are reported in Figure 2.7 from 150 to 1000 °C.

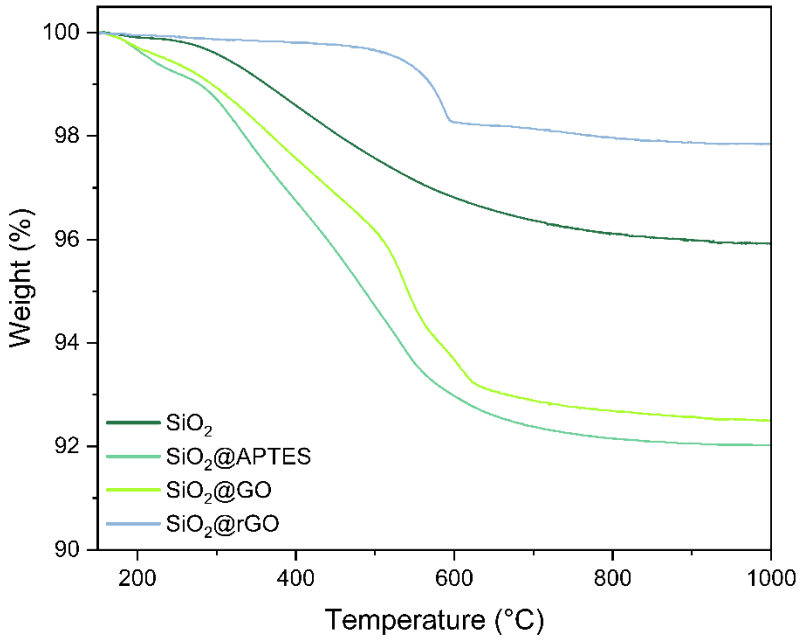

Figure 2.7 TGA thermograms of the products of each step of the SiO_2@rGO synthesis, reported between 150 and 1000 °C.

The estimation of the moles of APTES effectively deposited on SiO_2 surface is calculated taking into the account the weight loss of SiO_2@APTES between 150 and 1000 °C following the Equation A.20, deeply described in the appendix. In particular, the degree of functionalization, expressed as mass percentage and number of molecules per unit area, is reported in the Table 2.1 and demonstrates a good surface coverage of SiO_2 obtained with APTES.

Table 2.1 Functionalization degree of SiO_2@APTES.

	$wt.\%(Y)$	$\sigma[molecules/nm^2]$
SiO_2@APTES	4.23	7.39

The functionalization degree was further analysed by elemental CHNS measurements (Table 2.2). The nitrogen content has been used to calculate the amount of APTES expressed as $\sigma[molecules/nm^2]$, through the Equation A.21 from the appendix. Its value of 6.94 molecules nm^{-1} is consistent with the value obtained from the TGA, confirming the effective SiO_2 functionalization.

Table 2.2 CHNS elemental analysis results of SiO_2@APTES.

	C (wt.%)	H (wt.%)	N (wt.%)	S (wt.%)
SiO_2	0.27	1.3	0.08	0.292
SiO_2@APTES	3.72	1.477	1.00	0.247

It should be noted that the sample after the attachment of GO and before the reduction (i.e. SiO_2@GO) has an unexpected minor weight loss compared to the one of SiO_2@APTES. This phenomenon can be explained taking into account that the reaction environment used for the attachment of GO is water. In fact, after the functionalization with APTES, some molecules of silane can be just physiosorbed on the surface of the silica, without involving a covalent bond with the hydroxyl groups of silica. When the filler is dispersed in water for the attachment of GO, these APTES molecules undergo a condensation reaction to produce silica, decreasing the quantity of silane loss in the TGA analysis of SiO_2@GO and may be detached from the surface of silica. For this reason, SiO_2@APTES has been dispersed in water for a few hours without adding GO, to evaluate the quantity of silane lost or self-condensed on the surface. As shown in the Figure 2.8, the difference in the $\Delta wt.\%_{\,150-1000°C}$ is 2.06 ± 0.5 wt.%, confirming that part of APTES is effectively lost due to the dispersion of SiO2@APTES in water.

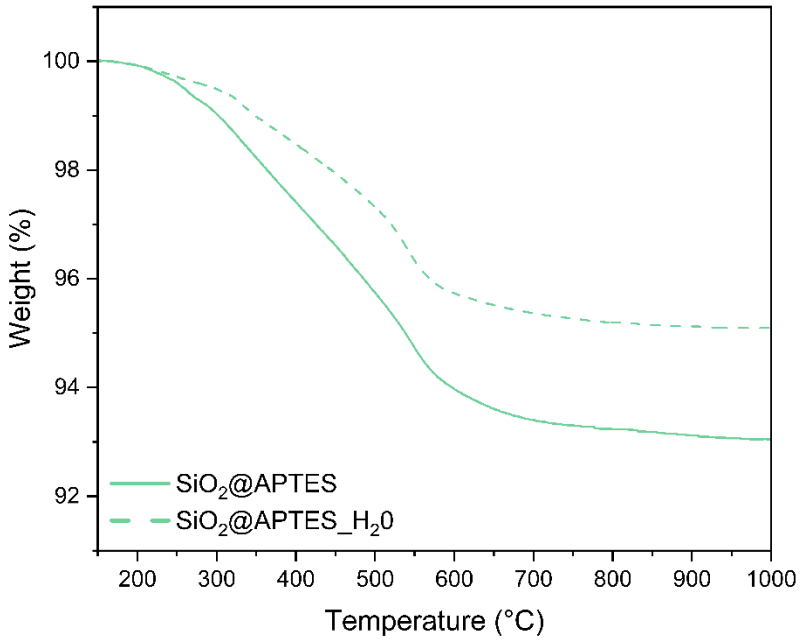

Figure 2.8 TGA thermograms of SiO_2@APTES and SiO_2@APTES_H_2O, reported between 150 and 1000 °C.

Moreover, the quantity of rGO attached to the filler can be calculated from the TGA thermogram of SiO_2@GO compared to SiO_2@APTES. In fact, during the reduction treatment, APTES is thermally degraded, while the GO has been partially reduced to rGO. Consequently, the $\Delta wt.\%_{150-1000°C}$ of SiO_2@rGO is due only to the degradation of r-GO which is 2.2 ± 0.2 wt.%, consistent with the nominal value of 2 wt.% used in the synthesis.

ATR-FTIR

The presence of APTES was further confirmed by ATR-FTIR analysis (Figure 2.9). The FTIR spectrum of SiO_2 NPs reveals characteristic vibrational features. The broad band in the 3700–3200 cm^{-1} region and the signal at 1633 cm^{-1} are assigned to O–H stretching and bending vibrations of physiosorbed water, respectively. The intense bands at 1060 and 805 cm^{-1} correspond to the symmetric and asymmetric Si–O–Si stretching, while the peak at 954 cm^{-1} is attributed to Si–OH stretching[6].

For SiO_2@APTES, additional signals confirm the successful surface modification with the APTES chains. The bands at 2980 and 2932 cm^{-1} arise from asymmetric C–H stretching of the -CH_2 groups of the APTES chains. Furthermore, the attenuation of the Si–OH stretching signal at 954 cm^{-1} indicates consumption of surface hydroxyl groups during the grafting reaction. Collectively, these spectral features qualitatively confirm the successful functionalization of silica with APTES.

The FTIR spectra of SiO_2@GO and SiO_2@rGO are not reported, as they do not show significant differences, likely due to the low GO and rGO content (2 wt.%), which is insufficient to generate new detectable peaks.

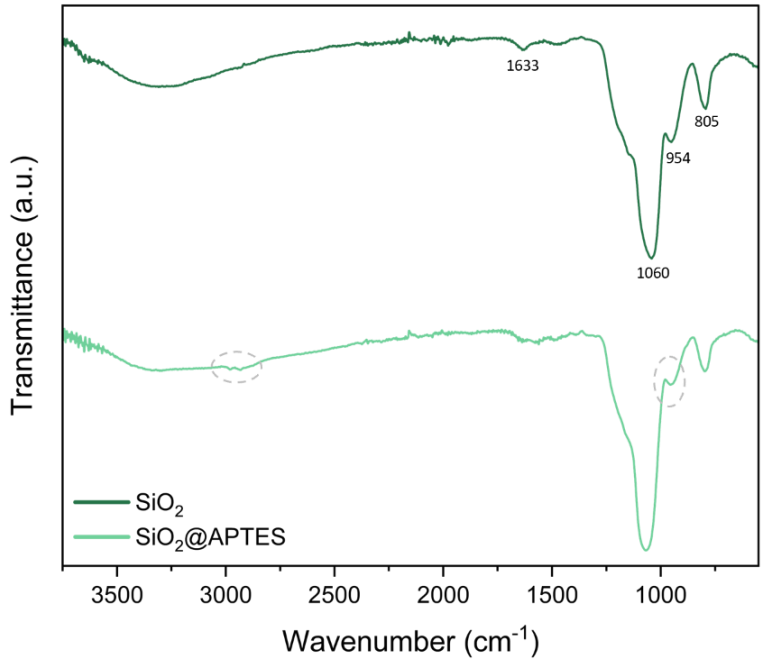

Figure 2.9 ATR-FTIR normalized spectra of bare SiO_2 NPs and SiO_2@APTES.

TEM

TEM analysis has been conducted to study the morphological features of the hybrid filler SiO_2@rGO compared to bare SiO_2 and SiO_2@APTES. First, the surface functionalization with APTES did not modify the morphological properties of SiO_2 NPs. The micrographs in Figure 2.10 clearly show the rGO sheet with the incorporated silica particles with same shape and dimension of the beginning, but the surface appears to be rough (blue narrow) with respect to the one of the naked filler (Figure 2.1). This phenomenon can be explained by the self-condensation of the physiosorbed APTES on the surface during the attachment of GO performed in water, as explained before in the TGA section. As Garcia et al.[7] reported in their study, when the grafting degree is high, the free chains of silane can self-condense to form silica nano-texturization in water, similarly to what happened during the SiO_2@rGO synthesis process.

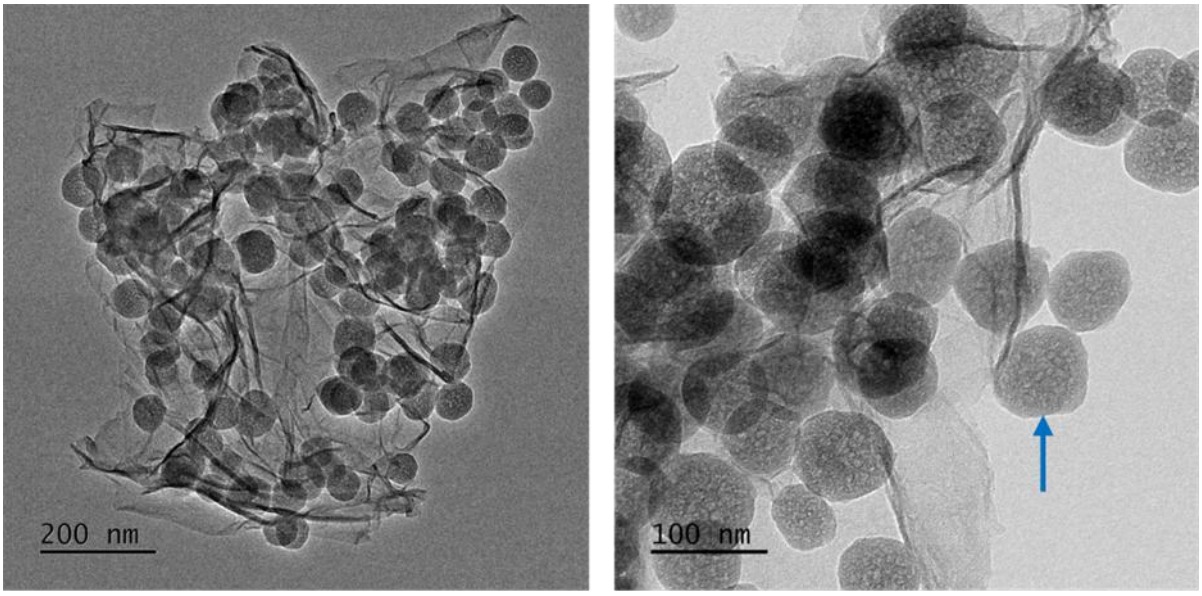

Figure 2.10 TEM images at different magnitudes of SiO_2@rGO.

Nitrogen physisorption

The nitrogen adsorption–desorption isotherm (77 K) was recorded for the SiO_2@rGO. As shown in Figure 2.11a, the isotherm exhibits characteristics of a type IV with a H3 hysteresis at high relative pressure, according to IUPAC classification[2]. This isotherm indicates a structure with a relatively low content of mesopores. At relative pressures (p/p_0) above 0.8, the sharp increase in adsorbed volume is attributed to the filling of interparticle voids. The SSA and the pore volume, calculated with BET and BJH models, are 58 ± 2 $m^2 g^{-1}$ and 0.439 cc g^{-1}. As expected, these values are not significantly different from the ones of the SiO_2 NPs (64 ± 3 $m^2 g^{-1}$, section 2.1.2).

Applying BJH model to the desorption curve, the pore size distribution has been derived revealing a distribution centred around at 24.1 nm, as shown in Figure 2.11b. This value is not related to the diameter of pores of the filler but is associated with interparticle voids generated by aggregation. In this case, a phenomenon of cavitation can be detected in the desorption branch of the isotherm and in the pore size distribution curve because of the artifact peak at 3.9 nm.

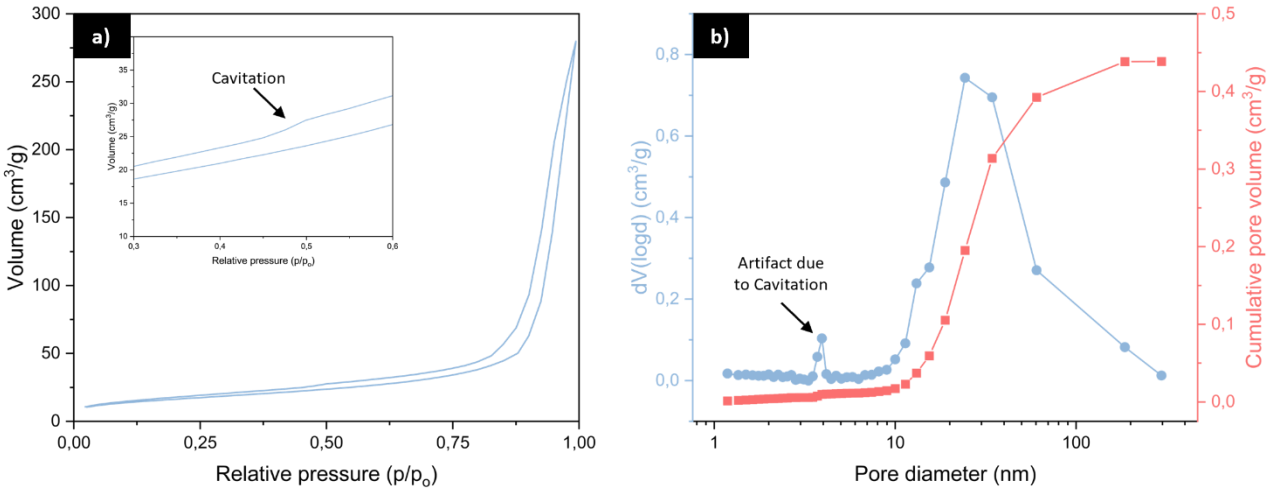

Figure 2.11 a) Nitrogen adsorption-desorption (77K) isotherms of SiO_2@rGO; b) Cumulative pore volume and pore size distribution curves of SiO_2@rGO calculated by BJH model for mesoporous analysis.

Raman

Raman spectroscopy has been used to characterize and evaluate possible differences in SiO_2@GO and SiO_2@rGO samples after the reduction treatment. In crystalline graphene, the characteristic Raman peaks are the G band and the 2D band, corresponding to first- and second-order Raman modes (≈1585 and 2700 cm^{-1}). The G band is the most intense and is related to the vibration mode E2g, characteristic of carbon-carbon vibration in the plane of the aromatic layers[8]. In the spectrum of GO, these peaks broaden due to the high concentration of defects introduced by oxidation. This structural disorder also gives rise to a strong D band (≈ 1350 cm^{-1}), associated with the A1g breathing mode defect-activated. The appearance of this band reflects the significant disruption of the graphene basal plane caused by oxidation and the subsequent partial reduction of GO[9].

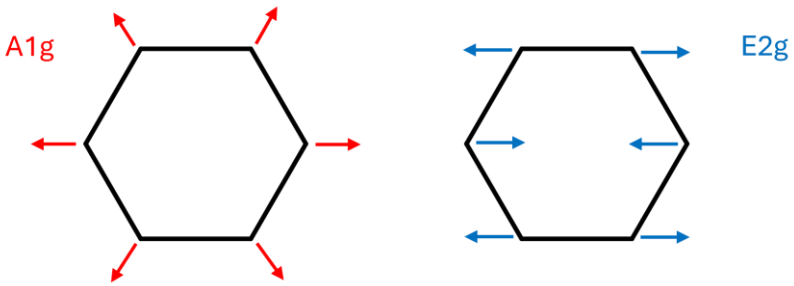

Figure 2.12 Representation of A1g and E2g vibration modes of GO.

In the spectra presented in Figure 2.13, the two bands G and D are set at 1600 and 1332 cm^{-1} respectively. The first one is representative of the domain of carbon sp^2 hybridization, while the second

of the C sp^3 hybridization. To evaluate the effectiveness of the reduction, Latorrata et al.[10] reports the variation of the intensities of the two bands (I_D/I_G). In this case, no significant variation is observed, which is reasonable since the reduction temperature is not high enough to induce the structural disorder that typically occurs above 1000 °C[11].

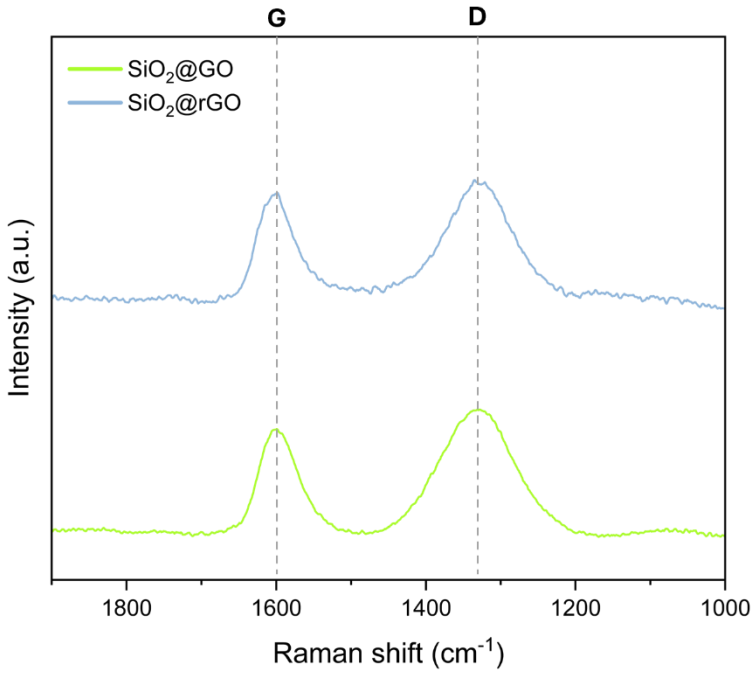

Figure 2.13 Raman spectra of SiO_2@GO and SiO_2@rGO.

XPS

XPS analysis has been used to evaluate the effectiveness of the reduction process performed on the hybrid filler. In fact, three different treatments have been executed for the reduction of X@GO: 400 °C in N_2, 600 °C in N_2, and 600 °C in H_2/N_2. For the fitting, a product of Gaussian and Lorentzian curves imposed to have the same FWHM (each sample) and an asymmetric Lorentzian curve to account for C sp^2 have been employed[12]. Deeply, the C1s signal has been fitted using 4 symmetric GL(30) and one asymmetric curve as reported in Figure 2.14. 3 GL(30) are attributed to different chemical arounds of carbon, 1 GL(30) is attributed to a mixed contribution attributable to both the graphitic C1s plasmon and to carbonates, and the asymmetric curve is used to identify the contribution of graphitic C sp^2. GL(30) curves are centered at 286.2 ± 0.1 eV (C-O bond of alcohols and ethers, violet), 287.5 ± 0.1 eV (carbon oxygen sp^2 bond of ketones and aldehydes, green), 288.8 ± 0.1 eV (carbon of carboxylic acids, blue) and one located at 290.9 ± 0.1 eV (yellow) related to carbonates and C sp^2 plasmon[13]. The asymmetric curve is placed at 284.5 ± 0.1 eV (C sp^2, red) and has been used to calibrate the spectrum[14–16].

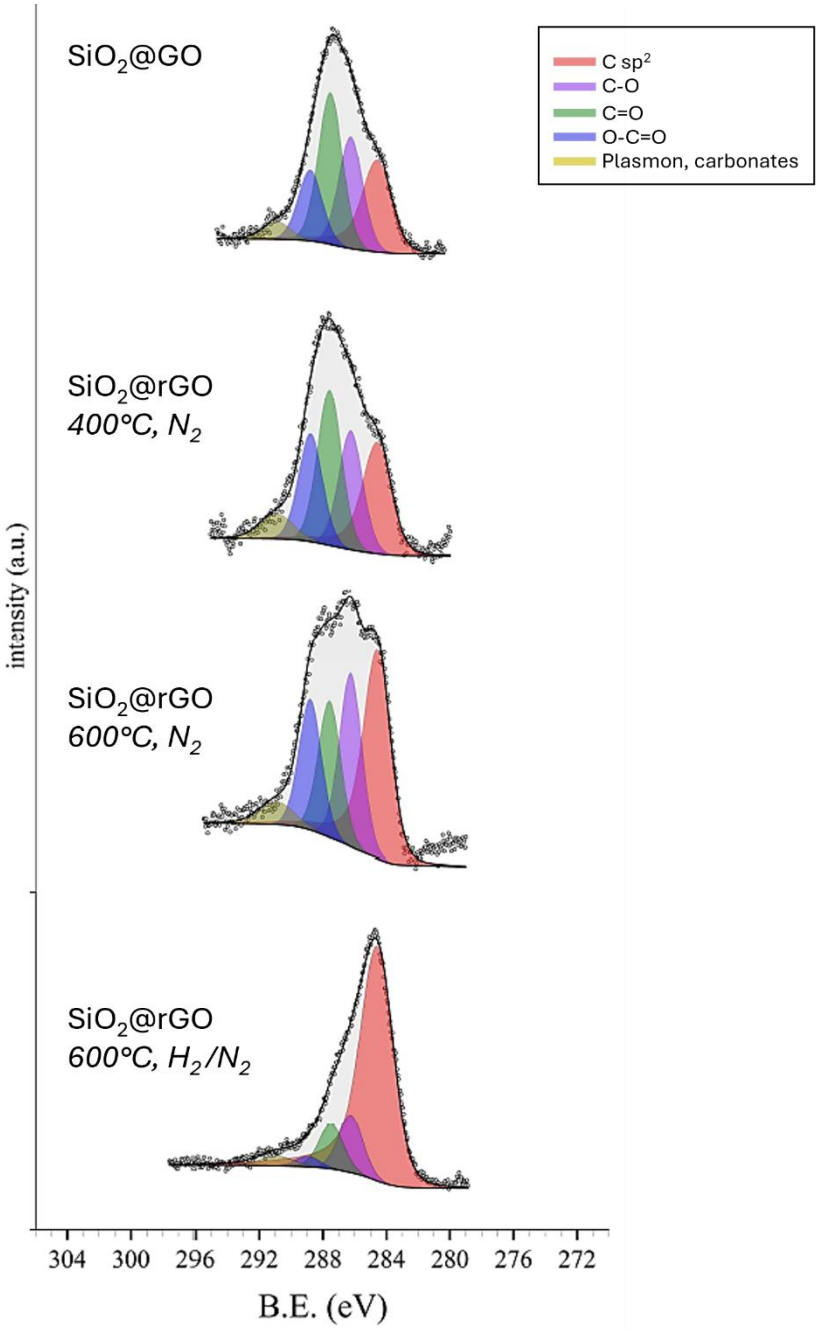

Figure 2.14 XPS spectra of C1s region for SiO_2@GO, SiO_2@rGO treated at 400 °C and 600 °C in N_2, and SiO_2@rGO treated at 600 °C in H_2/N_2.

The determination of the relative percentage of the 5 contributions is presented in Table 2.3 for all the samples analysed. Respect to the SiO_2@GO, all the sample reduced in nitrogen atmosphere did not present any significant differences, while the one reduced in H_2/N_2 atmosphere shows a clear increment in the C sp^2 contribute and a marked reduction in all the other components confirming the positive outcome of the reduction treatment.

Table 2.3 Relative percentage of the five contributions for the four samples investigated with XPS.

	SiO_2@GO	SiO_2@rGO (400 °C, N_2)	SiO_2@rGO (600 °C, N_2)	SiO_2@rGO (600 °C, H_2/N_2)
C sp^2 (red)	26.6	26.8	37.5	74.0
C-O (violet)	23.4	20.9	22.9	11.8
C=O (green)	31.3	27.5	18.0	9.2
O-C=O (blue)	14.7	19.0	17.3	2.2
Plasmon + carbonates (yellow)	4.0	5.8	4.3	2.8

2.2.3 Characterization of Hallo@rGO

TGA and CHNS

The TGA analysis has been used to evaluate the degree of functionalization with APTES and, secondly, to quantify the rGO in the filler Hallo@rGO, as already explained for SiO_2-based materials. The TGA thermographs of each product of the synthesis steps (i.e. Halloysite, Hallo@APTES, Hallo@GO and Hallo@rGO) are reported in Figure 2.15.

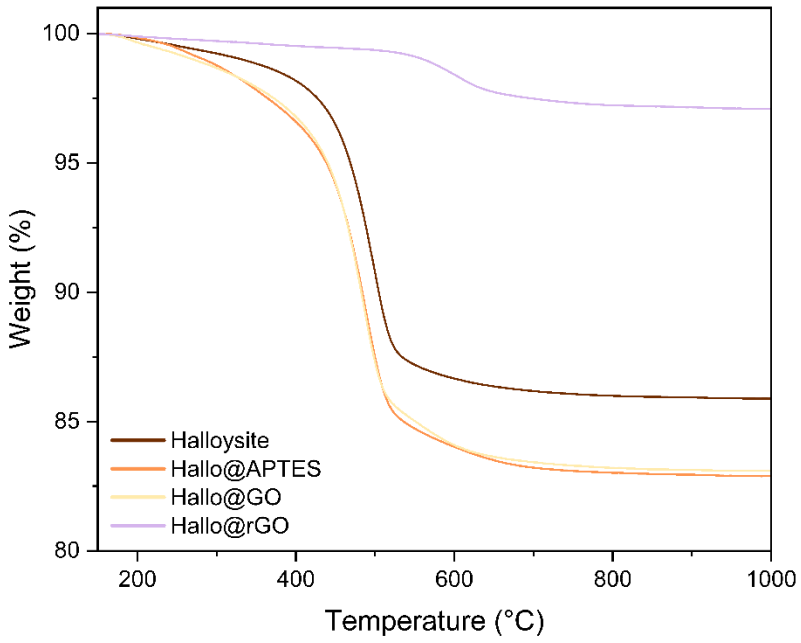

Figure 2.15 TGA thermograms of the products of each step of the Hallo@rGO synthesis, reported between 150 and 1000°C.

For the calculation of the functionalizing agent three percentages of weight loss (150-1000 °C) of halloysite has been used to calculate the OH_{sup} and, consequently, the moles of APTES to use in the reaction (Figure 2.16a). The TGA analysis has been performed but the difference in the functionalization is minimal, for this reason the moles of surface OH has been calculated starting from considering just the 50% of the $\Delta wt.\%_{150-1000°C}$ for the Equation A.18, in order to avoid high self-condensation of APTES.

In particular, the degree of functionalization, expressed as mass percentage and number of molecules per unit area, is reported in the Table 2.4.

Table 2.4 Functionalization degree of Hallo@APTES.

	$wt.\%(Y)$	$\sigma[molecules/nm^2]$
Hallo@APTES	3.74	8.24

CNHS measurements have been performed to confirm the functionalization degree (Table 2.5). The nitrogen content has been used to calculate, through the Equation A.2 from the appendix, the $\sigma[molecules/nm^2]$ which its value is 8.77 molecules nm^{-1}, consistent with the value obtained from the TGA.

Table 2.5 CHNS elemental analysis results of Hallo@APTES.

	C (wt.%)	H (wt.%)	N (wt.%)	S (wt.%)
Halloysite	0.43	1.652	0.45	0.353
Hallo@APTES	3.36	1.979	1.39	0.171

The TGA thermograms of Hallo@APTES and Hallo@GO in Figure 2.15 present a similar weight loss in the range 150-1000 °C. This phenomenon can be explained by considering the reaction environment during GO attachment. Following functionalization with APTES, some silane molecules may remain only physiosorbed on the surface, without forming covalent bonds with surface hydroxyl groups. Upon dispersion of the filler in water for GO grafting, these loosely bound APTES molecules undergo self-condensation reactions to form silica, thereby reducing the amount of silane loss observed in the TGA analysis of Hallo@GO. As shown in Figure 2.16b, Hallo@APTES_H_2O has been dispersed in water for a few hours in the absence of GO to evaluate the quantity of silane lost or self-condensed on the surface during the experimental treatment to anchor GO. The difference in the $\Delta wt.\%_{150-1000°C}$ is 2.01 wt.% which is the same percentage of GO added to the reaction, for this reason the two curves (Hallo@APTES and Hallo@GO) have almost the exact same weight loss.

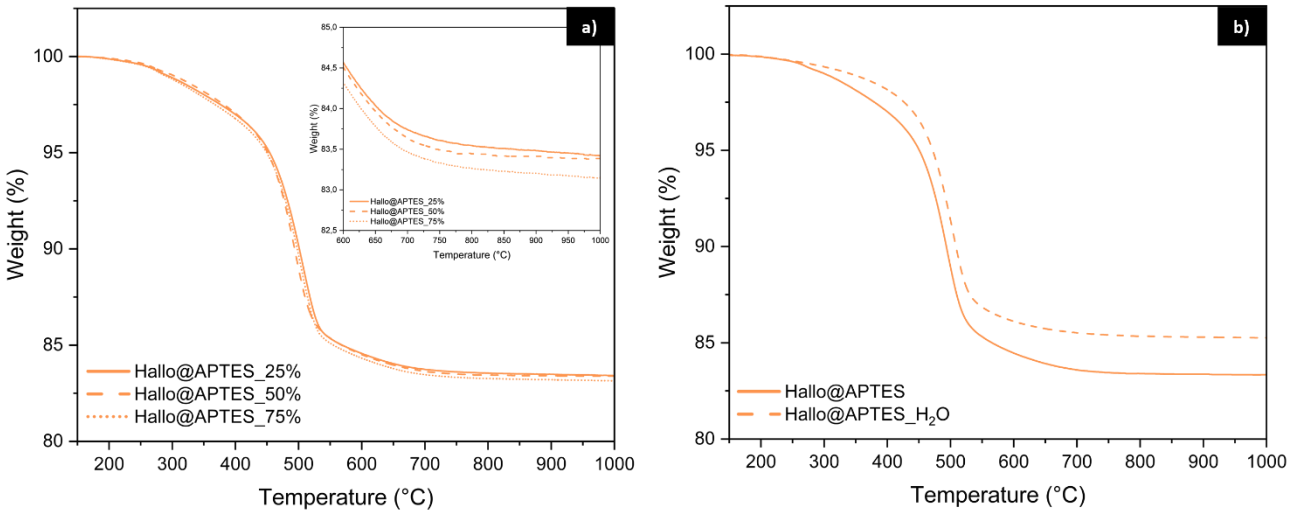

Figure 2.16 TGA thermograms reported between 150 and 1000°C of a) different ratios for functionalization of Hallo@APTES, and b) Hallo@APTES before and after been washed with distilled water.

Furthermore, the actual content of rGO in the filler can be quantified from the TGA thermogram (Figure 2.15). During the reduction treatment, APTES undergoes thermal degradation, while GO is partially reduced to rGO. As a result, the weight loss ($\Delta wt.\%_{(150-1000°C)}$) observed for Hallo@rGO is solely attributed to the degradation of reduced graphene oxide, amounting to 2.4 ± 0.3 wt.%, which is in good agreement with the nominal loading of 2 wt.%.

ATR-FTIR

The presence of APTES was further qualitatively confirmed by ATR-FTIR analysis (Figure 2.17). The FTIR spectrum of commercial halloysite nanoclay reveals characteristic vibrational features. The peaks at 3547 and 1647 cm^{-1} are assigned to O-H stretching of inner layer of water molecules. The intense bands at 3691 and 3622 cm^{-1} correspond to the inner-surface Al-OH stretching vibrations, while the Al-O-Si is at 525 cm^{-1}. The peaks at 1118 and 1005 cm^{-1} are related to the Si-O vibration and the Si-O-Si asymmetric stretching. The three peaks at lower wavenumber (795, 749 and 678 cm^{-1}) are assigned to Si-O stretching while the one at 908 cm^{-1} is related to external-surface OH stretching[17–19].

For Hallo@APTES, additional signals confirm the successful surface modification as observed for SiO_2 fillers. The bands around 2931 and 2887 cm^{-1} arise from asymmetric C–H stretching of silane. Furthermore, the attenuation of the Si–OH stretching signal at 903 cm^{-1} implies the consumption of OH_{sup} during the grafting reaction.

The FTIR spectra of Hallo@GO and Hallo@rGO are not reported, as they do not show significant differences, likely due to the low GO and rGO content (2 wt.%), which is insufficient to generate new detectable peaks.

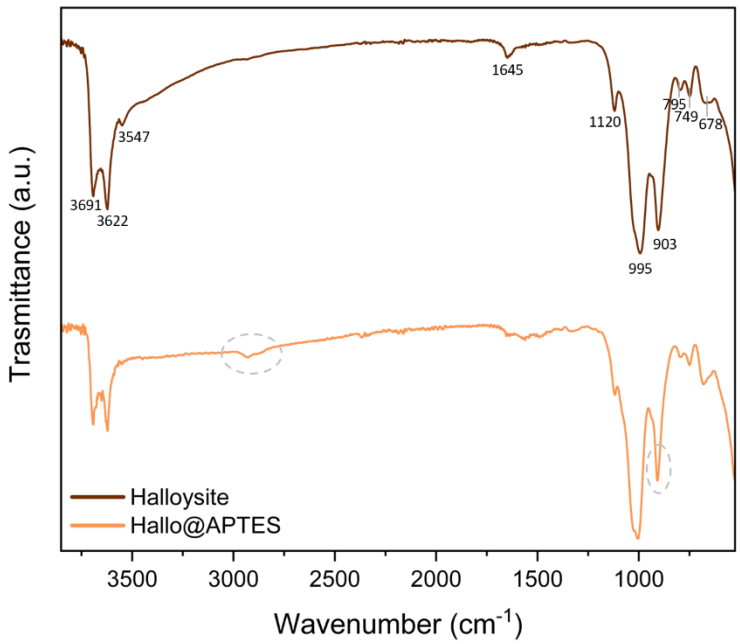

Figure 2.17 ATR-F TIR normalized spectra of commercial Halloysite and Hallo@APTES.

TEM

TEM analysis has been conducted to study the morphological features of the hybrid filler Hallo@rGO compared to bare Hallo and Hallo@APTES. As observed for SiO_2, no modifications on the morphology of halloysite structures were observed after the surface functionalization with APTES. The micrographs in Figure 2.18 show the rGO sheet (yellow arrow) with the incorporated halloysite. It's clearly notable that the structure of the nanoclay is in part disrupted because of the high temperature used for the reduction of the filler. Some of them maintained the same shape and dimensions (purple arrow), while others have a shorter length and an opened structure because of the loss of water molecules stuck in the channel (red arrow).

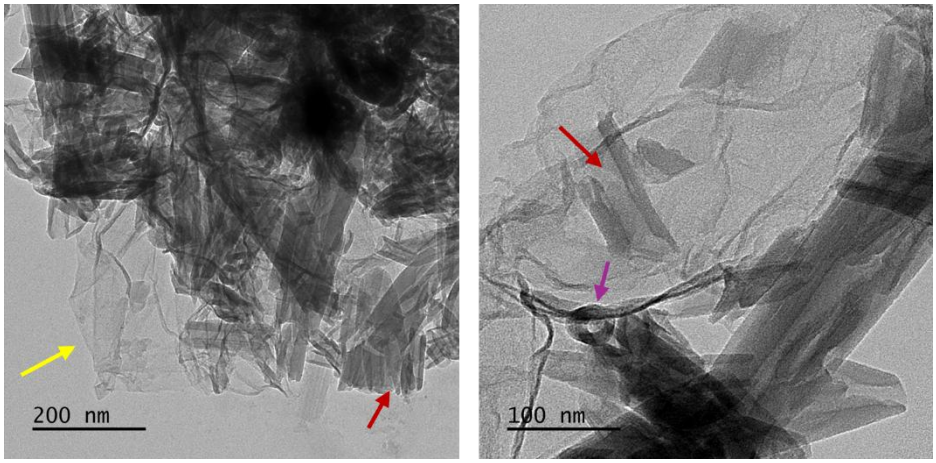

Figure 2.18 TEM micrographs at different magnitudes of Hallo@rGO.

Nitrogen physisorption

The nitrogen adsorption–desorption isotherm (77 K) was obtained for Hallo@rGO. As illustrated in Figure 2.19a, the curve corresponds to a type IV isotherm with an H3 hysteresis loop at high relative pressures, indicating the presence of a small fraction of mesopores. In addition, the sharp increase in adsorbed volume at $p/p_0 > 0.8$ is associated with the filling of interparticle voids. The SSA and the pore volume, calculated with BET and BJH models, are 62 ± 2 m^2 g^{-1} and 0.481 cc g^{-1}. As expected, these values are not significantly different from the ones of the commercial Halloysite nanoclay.

The pore size distribution is wider than the one of commercial halloysite. This can be explained by the thermal degradation of the structure of part of the filler during the reduction treatment. Moreover, also in this case cavitation is present in the isotherm and with an artifact peak in Figure 2.19b.

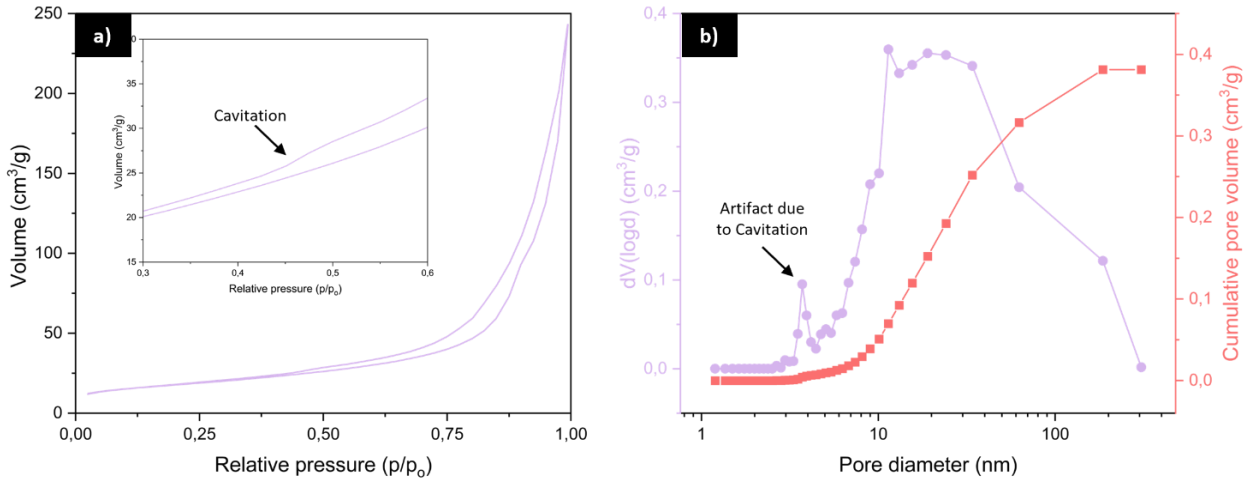

Figure 2.19 a) Nitrogen adsorption-desorption (77K) isotherms of Hallo@rGO; b) Cumulative pore volume and pore size distribution curves of Hallo@rGO calculated by BJH model for mesoporous analysis.

Raman

Raman spectroscopy was employed to characterize and compare Hallo@GO and Hallo@rGO samples. As shown in Figure 2.20, the spectra display two characteristic bands: the G band at ≈1600 cm^{-1}, associated with sp^2 carbon domains, and the D band at ≈ 1332 cm^{-1}, related to sp^3 hybridized carbon. As discuss for the silica-based filler, no significant variation of the ratio I_D/I_G has been detected probably due to the lower temperatures that do not affect the structural disorder.

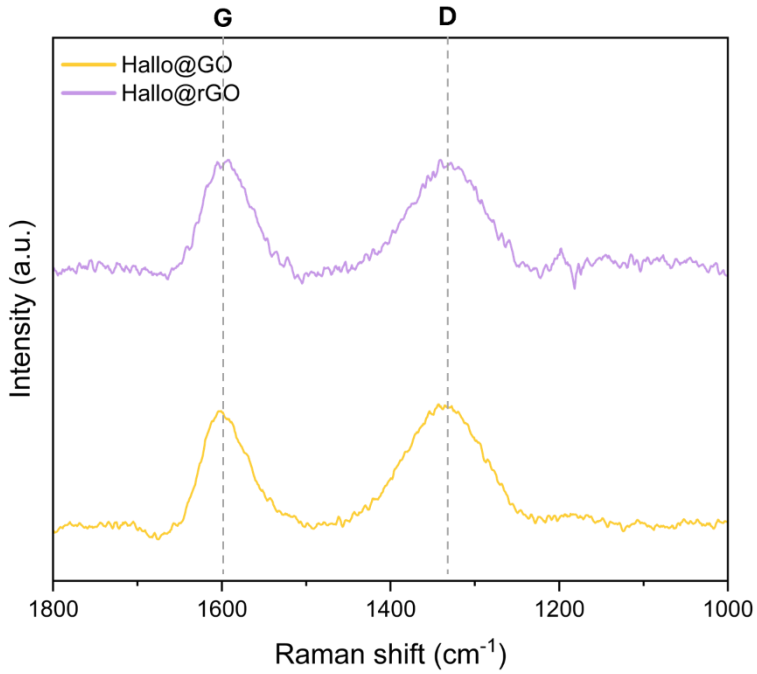

Figure 2.20 Raman spectra of Hallo@GO and Hallo@rGO.

2.3 Functional properties of polymer composite

In this Section, the incorporation of the hybrid filler X@rGO into a PDMS matrix was evaluated and their functional behaviour in terms of mechanical and conductive properties has been widely discussed. The production of the polymer composite was made through a solvent casting process where the polymer is dissolved in a suitable solvent, the filler is embedded and then the mixture is molded forming a uniform layer and then dried to evaporate the solvent. This is done with the use of suitable temperature to favourite the curing of the matrix.

The resulting materials were characterized in terms of their mechanical, thermal, and dielectric properties, revealing that the incorporation of rGO-modified fillers affects the crosslinking behaviour, enhances electrical conductivity, and influences interfacial polarization processes.

2.3.1 Experimental procedure of the composite

Materials

Sylgard 184 Silicone Elastomer Kit (PDMS) was purchased from Dow Corning. Dichloromethane (DCM). rGO powder was purchased from Sixth Element.

Procedure

In a round-bottom flask, 2.0 g of PDMS were dispersed in 4 mL of DCM by ultrasonication for 15 min. The curing agent (10:1) has been added and sonicated for 15 min more. After that, X@rGO and rGO powder is added with different loading and sonicated for 30 min. The solution mixture was cast in a Teflon mold with a diameter of 7 cm and let the solvent evaporate under the hood for 24 h. The film is then cured at 105 °C for 5 h and one hour more with controlled vacuum (pressure of 250 mbar).

Different loadings of X@rGO have been used to make the composite and summarized in the Table 2.6. These amounts (expressed as wt.%) are calculated with respect of the mass of PDMS used for the film preparation.

Table 2.6 Different loadings of the filler X@rGO for all the composites produced with the PDMS matrix.

	PDMS (g)	Curing agent (g)	SiO_2@rGO (wt.%)	Hallo@rGO (wt.%)	rGO powder (wt.%)
PDMS	2	0.2	-	-	-
SiO_2@rGO15%	2	0.2	15	-	-
SiO_2@rGO30%	2	0.2	30	-	-
SiO_2@rGO30%_2%rGO	2	0.2	30	-	2
Hallo@rGO15%	2	0.2	-	15	-
Hallo@rGO30%	2	0.2	-	30	-
Hallo@rGO30%_2%rGO	2	0.2	-	30	2

2.3.2 Characterization of the composite

TGA

TGA analysis has been used to evaluate the thermal stability of the composites and to calculate the effective loading of the fillers in the final materials. This is done by comparing the weight loss measured between 30 and 1000 °C obtained for the nanocomposites prepared with X@rGO to the one measured for bare PDMS. Results are summarized in Figure 2.21 and in Table 2.7.

The thermal profile of bare PDMS displays the typical degradation pathway already observed in the literature[20] with a residual weight of 50 wt.%, probably deriving from silica formation induced by the TGA thermal treatment. For Hallo@rGO composites, a significant decrease in the thermal stability is detectable (Fig. 2.21a), ascribable to the scarce filler-matrix interaction or to segregation phenomena. Accordingly, the expected filler content matches with the values retrieved from TGA weight loss at 1000 °C. Conversely, the thermal stability of SiO_2@rGO15%, SiO_2@rGO30% and SiO_2@rGO30%_2%rGO samples remains almost similar to that of PDMS, suggesting a better affinity between the hybrid filler and the siloxane polymer. This may explain the discrepancy among the nominal residual masses and those obtained at the end of the thermal degradation, which results similar and lower for each hybrid filler loading. In particular, we may infer that the enhanced filler-rubber interaction inhibit PDMS degradation and transformation into silica, finally leading to a minor inorganic content. These results find support in the enhanced mechanical properties of SiO_2@rGO composites if compared to Hallo@rGO composites (see next section).

Table 2.7 Weight loss percentages from the TGA analysis and calculated from the nominal loading of X@rGO.

	Expected weight loss (wt%)	Calculated weight loss during TGA (wt.%)
SiO_2@rGO15%	57.5	56.9
SiO_2@rGO30%	65	57.6
SiO_2@rGO30%_rGO2%	64	57.0
Hallo@rGO15%	57.5	57.4
Hallo@rGO30%	65	64.9
Hallo@rGO30%_rGO2%	64	61.0

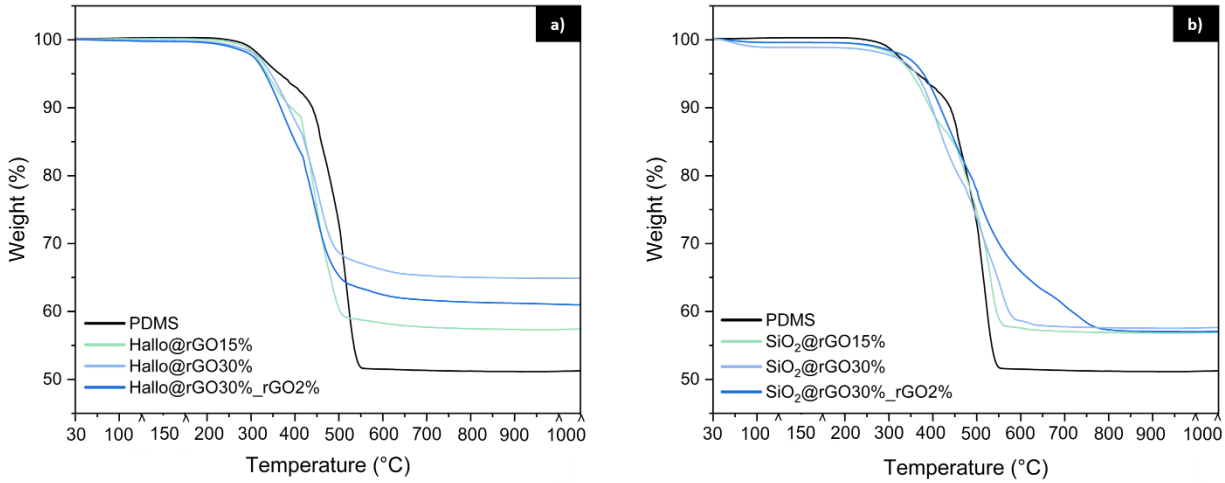

Figure 2.21 TGA curves of a) SiO_2@rGO and (b) Hallo@rGO composites.

DSC

Dynamic differential scanning calorimetry was employed to analyse the curing kinetics of nanocomposite mixtures made of silicone-based matrix containing X@rGO hybrid filler. In literature, the typical exothermic peak of the PDMS curing reaction occur in the range from 90 to 110°C[21]. The curves related to the curing of PDMS in presence of SiO_2@rGO are reported in Figure 2.22a. The addition of different filler contents results in a slight, though not meaningful, shift toward higher. Controversy, the presence of Hallo@rGO shifts the exothermic peak significantly to higher temperatures and a marked decrease in the peak area is observed (Figure 2.22b) in respect to pure PDMS. This behaviour can be attributed to a reduced filler-matrix compatibility, which leads to a delayed curing of the PDMS in the presence of the halloysite-based hybrid filler. This phenomenon is commonly observed when the filler partially inhibits the polymer crosslinking process [22,23].

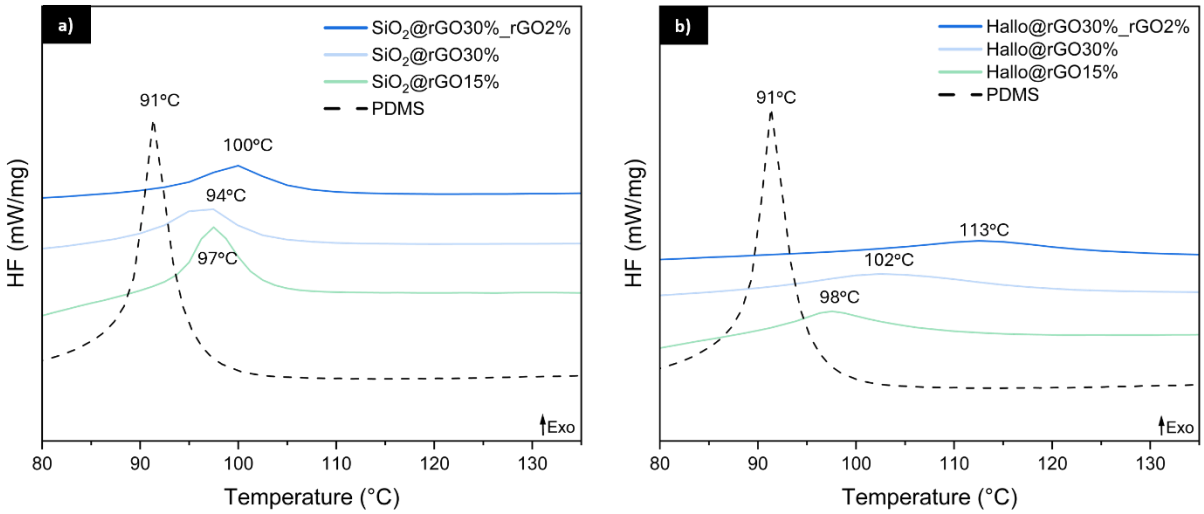

Figure 2.22 DSC curves of in-situ curing of PDMS in the presence of a) SiO_2@rGO and b) Hallo@rGO.

2.3.3 Functional properties of the composite

Dielectric Spectroscopy

Dielectric spectroscopy has been used to study the electrical properties of the composites. The hybrid filler X@rGO has been dispersed in a polymeric matrix (i.e. PDMS) with different loading to evaluate the formation of a conductive network. In Figure 2.23b is reported the real part of the conductivity, σ', for all samples at room temperature. For the PDMS neat, the conductivity reached a plateau at low frequencies ($\approx 10^{-14}$ S cm^{-1}) due to ionic conductivity of the matrix. Also, samples SiO_2@rGO30%_rGO2% and Hallo@rGO30%_ rGO2% show a plateau but at higher value of σ' due to the electronic conductivity of rGO[24]. The elevated conductivity of these samples is further evidenced by their high ε' values (Figure 2.23a). This behaviour clearly indicates the formation of a continuous conductive network in the PDMS composite. The rest of the samples do not exhibit a plateau in conductivity with values similar to the one of neat matrix. In this case, the conductive pathway is not formed in the composite, though certain conductivity-related phenomena lead to increased absolute values most likely associated with interfacial polarization[25]. In Figure 22a, the real part of the dielectric permittivity is reported for all the samples at room temperature. For insulating materials, ε' is frequency independent, except at low frequencies where conductivity effects prevail[26]. In contrast, nanocomposites that are conductive or near the electrical percolation threshold show higher and frequency-dependent ε' values, primarily due to interfacial polarization and conductivity-related processes. For PDMS neat ε' is constant at ≈ 3.5, while for the other samples the values are higher but exhibit similar behaviour of the matrix. Only SiO_2@rGO30%_rGO2% and Hallo@rGO30%_rGO2% values are significantly higher and increase in a non-linear way with the frequency resulting in the only two composites with electrical properties.

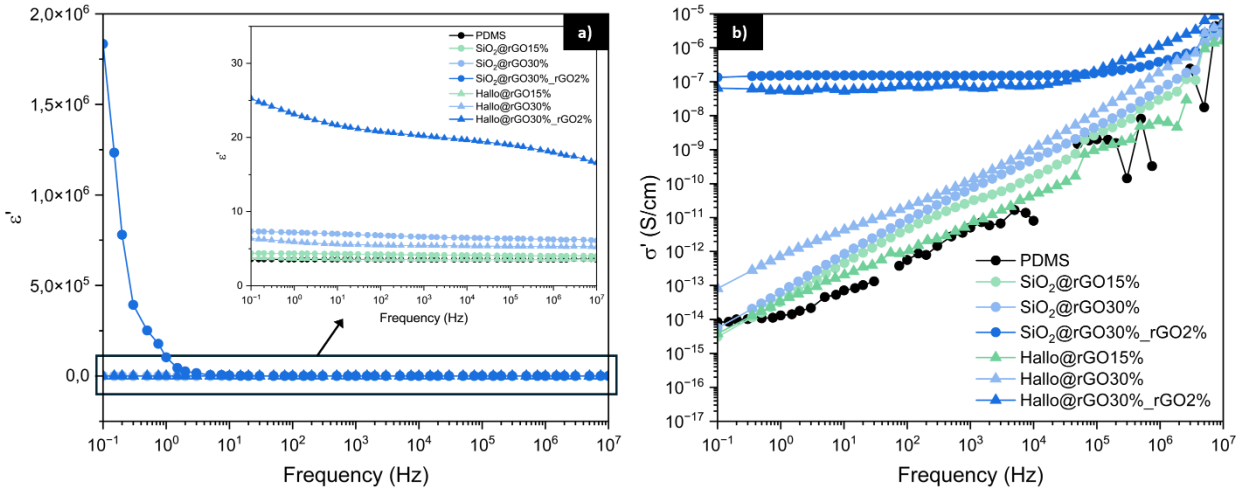

Figure 2.23 Dielectric permittivity (a) and conductivity (b) of the X@rGO/PDMS composites as a function of frequency.

DMA

Dynamic Mechanical Analysis has been performed to evaluate the viscoelastic properties of the composites with different loadings of X@rGO. Figure 2.24a illustrates Tanδ as a function of temperature. The neat PDMS sample gives a main transition corresponding to the glass transition temperature, T_g, at ≈ -120 °C and a relaxation peak at ≈ -50 °C. The same behaviour can be detected for all the other samples except for SiO_2@rGO30%_rGO2% and Hallo@rGO30%_rGO2%. In this case, a shift to higher temperature can be observed for the second relaxation peak (i.e. -50 °C) corresponding to the formation of conglomerates or clusters arising from the interaction between rGO and the polymer chains of the matrix[27]. These interactions shift the polymer relaxation peak to higher temperatures, as the increased network constraints restrict the molecular mobility of the polymer chains[28,29]. The second peak arising at ≈ -90 °C for these two composites may be also linked to an interaction of the rGO content and PDMS matrix.

Storage Modulus, E', has been reported in Figure 2.24b as a function of the temperature. It is clearly notable that increasing the loading of X@rGO filler in the composite results in a higher value of E'. These trends provide clear evidence of the reinforcing effect imparted by both silica and halloysite-based fillers to the polymeric matrix.

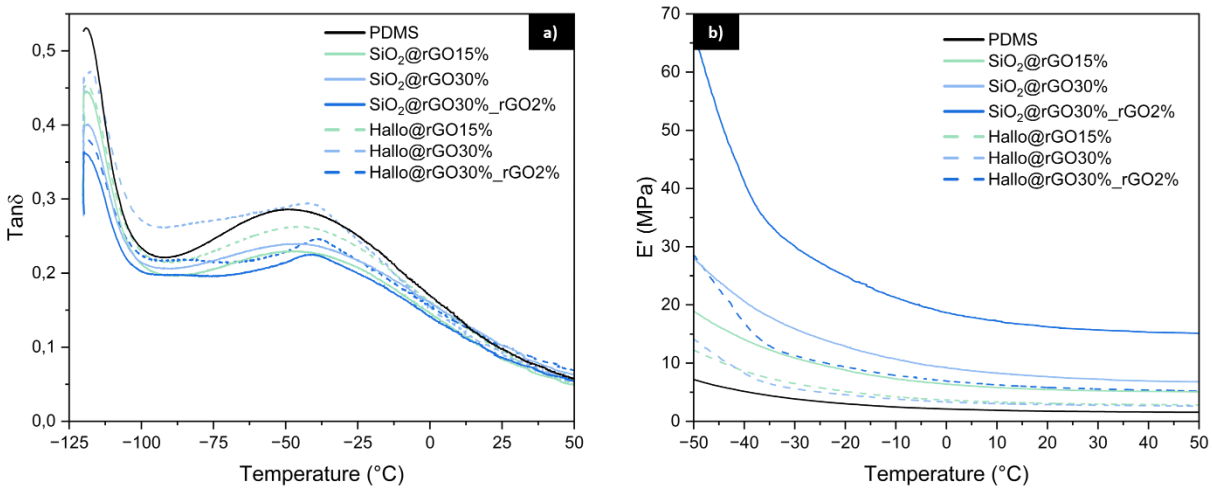

Figure 2.24 Tangent Delta (a) and Storage Modulus (b) of the X@rGO/PDMS composites as a function of temperature.

2.4 Introduction of SiO_2@rGO in GFRPs

Glass fiber-reinforced polymer composites are extensively employed in structural and transportation applications due to their outstanding strength-to-weight ratio. In these materials, the mechanical performance is largely dictated by the fiber–matrix interphase, which is the critical zone between fiber surface and the polymer matrix chains that must be strategically designed and precisely engineered to achieve optimal mechanical properties of the final composite. The single-fiber push out test represents a powerful micromechanical technique for evaluating the fiber–matrix interfacial properties in GFRPs under conditions closely resembling those encountered in real engineering applications. This method enables quantitative assessment of parameters such as interfacial shear strength (IFSS), debonding energy, and interfacial frictional stress, which are critical for understanding load transfer mechanisms at the microscale.

Parizi M. et al.[30] reported in their work the modification of the fiber surface with silica coatings with different porosity to evaluate the improvement on the adhesion fiber-matrix. They discovered that the introduction of a mesoporous silica coating on the glass fiber surface led to the highest specific surface area, pore size, and adhesion energy, resulting in a significant enhancement of the composite's mechanical performance. The modified fibers provided up to a 31% increase in Young's and flexural modulus compared to composites reinforced with untreated woven GFs. This improvement is attributed to more efficient stress distribution and uniform load transfer across the polymer–GF interphase, facilitated by the mesoporous coating.

Moreover, the introduction of fillers in the matrix has been deeply studied in literature to enhance the interfacial adhesion in GFRPs. The observed improvements can be attributed to the toughening effect of the nanoparticle-reinforced matrix, which mitigates stress concentrations and enhances energy dissipation during deformation, thereby promoting more efficient stress transfer and greater resistance to interfacial debonding. Gorbatikh L. et al[31] studied the influence of CNTs dispersed in the matrix onto the interfacial properties. IFSS value of GFRPs increase from 57 to 84 MPa adding carbon nanotube resulting in a moderate enhancing of the adhesion GF-epoxy matrix. Tian Y. et al[32] studied the influence on the interfacial shear strength of silica content mixed in the epoxy matrix in carbon fiber reinforced polymers (CFRPs). IFSS, analysed with a micro-droplet test, increased by 38% after the addition of 20 wt.% silica NPs. The SEM analysis of the CF surface showed that, as the silica content increases, a greater amount of matrix residue adheres to the fiber surface, indicating a stronger interfacial adhesion between the carbon fiber and the silica-modified epoxy matrix.

Starting from these considerations on the effects of surface coatings and the addition of fillers in the epoxy matrix, five different samples have been tested micromechanically:

- Neat GF
- Silica coated GF
- Silica coated GF with SiO_2@rGO hybrid filler embedded in the epoxy matrix
- Silica coated GF with SiO_2 NPs and rGO powder embedded in the epoxy matrix
- Silica coated GF with rGO powder embedded in the epoxy matrix

2.4.1 Silica coating of GF

2.4.1.1 Experimental procedure

Materials

(1-Hexadecyl)trimethyl-ammonium bromide (CTAB, 98%) and sodium hydroxide pellets (NaOH, 98 %) were purchased from Alfa Aesar. Tetramethyl orthosilicate (TMOS, ≥98.0%) was purchased from Fluka. Ammonia solution (NH_4OH, 25 %) was purchased from Sigma-Aldrich. Hydrochloric acid (HCl, 37%) was purchased from VWR Chemicals. Ethanol (EtOH, ≥99.8%) was purchased from Carlo Erba.

Procedure

A piece of wGF (6x6 cm) was immersed in a 1 M NaOH/EtOH solution overnight to clean the surface. The GF was then washed in acetone, later in ethanol, and finally in water. GF was dried in an oven at 80 °C for 10 min. CTAB (160 mg) was dissolved in a mixture of water (70 mL) and ethanol (30 mL) by sonication for 15 min. After the CTAB was completely dissolved, ammonia solution (60 µL) and TMOS (480 µL) were added sequentially under stirring. The solution was stirred for only 10 s before increasing the temperature up to 60 °C and immersing the wGF. After 24 h of reaction, the coated wGF was gently rinsed with water and immersed in a 0.1 M HCl/EtOH solution for 10 min to completely remove any trace of CTAB. Finally, the sample was dried in an oven at 80 °C overnight.

2.4.1.2 Characterization of Silica coated GF

SEM

SEM analysis has been used to evaluate the morphological features of the silica coated GF. As shown in Figure 2.25, the procedure successfully coated all the GF surface with a homogeneous amorphous layer decorated with a superficial layer of spherical SiO_2 NPs with a diameter of 352 ± 21 nm.

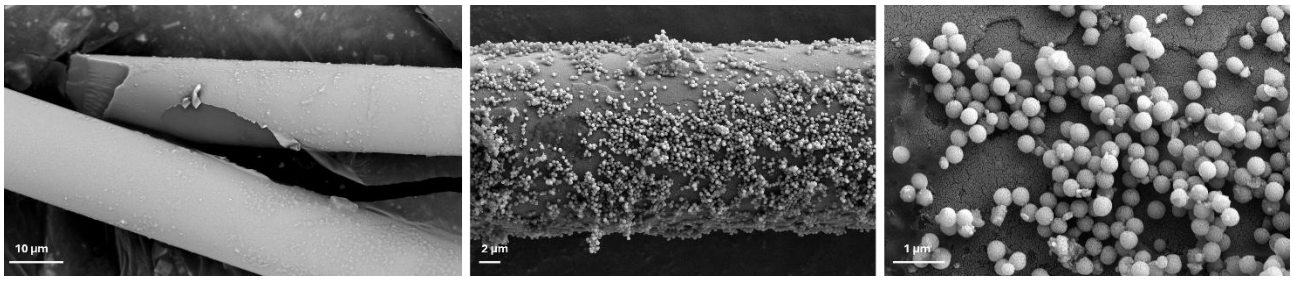

Figure 2.25 SEM micrographs at different magnitudes of silica coated GF.

2.4.2 Push out test

Test procedure

To prepare the specimens for push out test (Figure 2.26), a thin cross-sectional slice of the composite is extracted such that the fibers are oriented perpendicular to the surface. The slicing process must be conducted with high precision to minimize mechanical or thermal damage to the surrounding matrix. The thickness of the slice is a key parameter: it must be sufficiently small to allow the embedded fibers to be completely pushed through without bending or fracture, yet thick enough to preserve interfacial integrity and representative mechanical behaviour.

During testing, the specimen is carefully positioned on a supporting stage with a micro-fabricated groove or aperture beneath the targeted fiber. This configuration ensures that the fiber, once dislodged, can move freely into the open space, thereby eliminating any counterforce that could artificially increase the measured load.

A flat-ended conical punch is then aligned coaxially with the selected fiber using an optical microscope and the punch is advanced at a controlled displacement rate. From the resulting curve, the interfacial shear strength can be derived using appropriate micromechanical models that consider the fiber radius, embedded length, and applied force. In this way, the single-fiber pushout test provides a quantitative and reproducible method for probing the local interfacial behaviour in composite materials, enabling direct correlation between microstructural features (e.g., surface treatments, coatings, or interphases) and macroscopic composite performance.

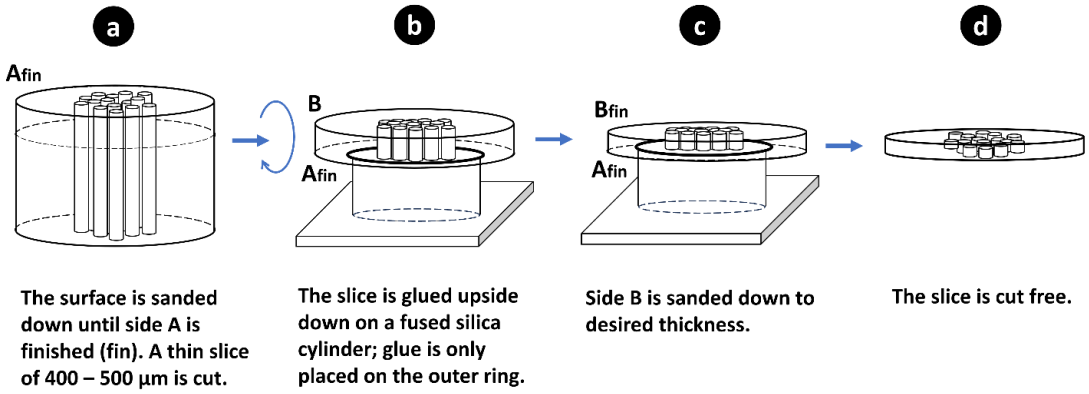

Figure 2.26 Schematic representation of the preparation of the specimen for push out test.

Experimental results

The results of the samples tested with push out method are reported in Figure 2.27 in terms of Interfacial Shear Strength. Firstly, the presence of the silica coating on the glass fibers (blue circle), compared to the neat GF, didn't increase the adhesion fiber-matrix, but in fact decreased the IFSS. This feature may be addressed to a non-effective infiltration by the epoxy due to a limited porosity of the silica coating.

The sample with SiO_2@rGO embedded in the matrix (red triangle) shows a significant improvement in IFSS suggesting a compatibilizer role inside the matrix. Differently, the sample with the same amount of SiO_2 and rGO but non bounded in a hybrid structure (yellow star) result in a lower value of IFSS. This trend can be explained considering that in the hybrid filler, silica may act as a carrier for rGO in the matrix, preventing separation phase and agglomeration of the two components. In this way rGO results to be more dispersed and with a more extensive sheet structure, increasing the contact surface with the epoxy resin improving the fracture toughness in shear mode[33].

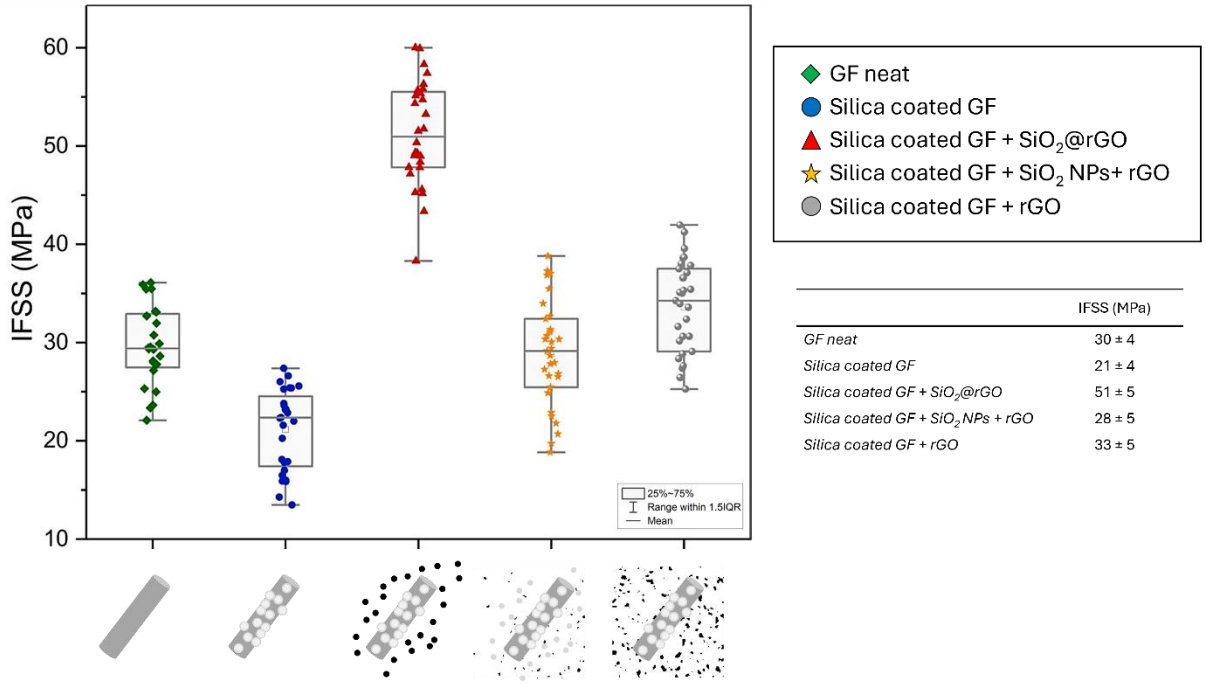

	IFSS (MPa)
GF neat	30 ± 4
Silica coated GF	21 ± 4
Silica coated GF + SiO_2@rGO	51 ± 5
Silica coated GF + SiO_2 NPs + rGO	28 ± 5
Silica coated GF + rGO	33 ± 5

Figure 2.27 IFSS values reported for the five samples tested though push out method.

2.5 Conclusions

In this chapter, a hybrid filler based on reduced graphene oxide (X@rGO, with X = SiO_2 nanoparticles or Halloysite nanoclay) was successfully synthesized, thoroughly characterized, and incorporated into a PDMS polymer matrix to assess its structural and functional properties.

The preparation of bare fillers highlights their intrinsic morphological and textural features: silica nanoparticles with uniform spherical shape (≈ 70 nm) and halloysite with tubular morphology (45 ± 15 nm diameter, 0.5 – 2 μm length).

The hybridization pathway consists of three steps: APTES functionalization, attachment of GO and subsequent thermal reduction to rGO. TGA, CHNS, ATR-FTIR, TEM, BET, Raman, and XPS analyses confirmed the successful deposition of APTES, the effective anchoring of GO, and its partial reduction under a H_2/N_2 atmosphere. For both SiO_2@rGO and Hallo@rGO, a rGO content of ≈ 2 wt.% is retrieved, in line with nominal values, while morphological analyses reveal the preservation of SiO_2 structure and a partial degradation of halloysite during high-temperature treatment.

When incorporated into PDMS, the hybrid fillers impart improved thermal degradation and reinforcement as well as electrical conductivity. TGA allows to assess the effective filler loading, while DMA analysis shows that, increasing X@rGO content, the storage modulus generally increases, proving the reinforcing capability of the novel fillers. Moreover, in composites containing an additional small fraction of free rGO, a shift in the polymer relaxation peak toward higher temperatures is detected, evidencing filler–matrix interactions that constrain chain mobility.

Dielectric spectroscopy further demonstrates that only for SiO_2@rGO30%_rGO2% and Hallo@rGO30%_rGO2% composites a continuous conductive network is developed, as testified by their high conductivity and frequency-dependent permittivity. The other samples behave similarly to neat PDMS, with interfacial polarization effects contributing only marginally to their dielectric response.

Finally, the micromechanical investigation through the single-fiber push-out test highlights the crucial influence of interfacial engineering on the adhesion behaviour of GFRP composites. The application of a silica coating on glass fibers, despite improving surface coverage, does not enhance the interfacial shear strength, likely due to limited porosity hindering proper epoxy infiltration. On the other hand, the incorporation of SiO_2@rGO hybrid fillers into the epoxy matrix leads to a remarkable increase in IFSS, confirming the synergistic effect between silica nanoparticles and graphene oxide. In the hybrid structure, silica acts as a carrier, improving rGO dispersion and preventing agglomeration, which promotes stronger interfacial bonding and more efficient stress transfer. These results demonstrate that combining surface modification with tailored hybrid nanofillers represents an effective strategy to

optimize the fiber–matrix interphase and enhance the overall mechanical performance of GFRP composites.

In conclusion, these findings provide a solid foundation for the design of multifunctional smart nanocomposites that exploit synergistic effects between inorganic carriers and graphene-derived nanostructures. Moreover, the exploitation of X@rGO in GFRPs may be a suitable way to obtain composite with electrical conductivity and enhanced mechanical properties, trough the increase of adhesion GF-matrix, for structural monitoring applications.

References

[1] Stöber W, Fink A, Bohn E. Controlled growth of monodisperse silica spheres in the micron size range. *J Colloid Interface Sci*. 1968;26(1):62-69. doi:10.1016/0021-9797(68)90272-5

[2] Thommes M, Kaneko K, Neimark A V., Olivier JP, Rodriguez-Reinoso F, Rouquerol J, et al. Physisorption of gases, with special reference to the evaluation of surface area and pore size distribution (IUPAC Technical Report). *Pure and Applied Chemistry*. 2015;87(9-10):1051-1069. doi:10.1515/pac-2014-1117

[3] Schlumberger C, Thommes M. Characterization of Hierarchically Ordered Porous Materials by Physisorption and Mercury Porosimetry—A Tutorial Review. *Adv Mater Interfaces*. 2021;8(4):2002181. doi:10.1002/admi.202002181

[4] Thommes M. Chapter 15 - Textural Characterization of Zeolites and Ordered Mesoporous Materials by Physical Adsorption. In: Čejka J, van Bekkum H, Corma A, Schüth F, eds. *Studies in Surface Science and Catalysis*. Vol 168. Elsevier; 2007:495-XIII. doi:10.1016/S0167-2991(07)80803-2

[5] Huang L, Zhu P, Li G, (Daniel) Lu D, Sun R, Wong C. Core–shell SiO2@RGO hybrids for epoxy composites with low percolation threshold and enhanced thermo-mechanical properties. *J Mater Chem A Mater*. 2014;2(43):18246-18255. doi:10.1039/C4TA03702B

[6] Jesionowski T, Klapiszewski Ł, Milczarek G. Kraft lignin and silica as precursors of advanced composite materials and electroactive blends. *J Mater Sci*. 2014;49. doi:10.1007/s10853-013-7822-7

[7] García N, Guzmán J, Benito E, Esteban-Cubillo A, Aguilar E, Santarén J, et al. Surface Modification of Sepiolite in Aqueous Gels by Using Methoxysilanes and Its Impact on the Nanofiber Dispersion Ability. *Langmuir*. 2011;27(7):3952-3959. doi:10.1021/la104410r

[8] Sardinha AF, Almeida DAL, Ferreira NG. Electrochemical impedance spectroscopy correlation among graphene oxide/carbon fibers (GO/CF) composites and GO structural parameters produced at different oxidation degrees. *Journal of Materials Research and Technology*. 2020;9(5):10841-10853. doi:10.1016/j.jmrt.2020.07.082

[9] Claramunt S, Varea A, López-Díaz D, Velázquez MM, Cornet A, Cirera A. The Importance of Interbands on the Interpretation of the Raman Spectrum of Graphene Oxide. *The Journal of Physical Chemistry C*. 2015;119(18):10123-10129. doi:10.1021/acs.jpcc.5b01590

[10] Latorrata S, Cristiani C, Basso Peressut A, Brambilla L, Bellotto M, Dotelli G, et al. Reduced Graphene Oxide Membranes as Potential Self-Assembling Filter for Wastewater Treatment. *Minerals*. 2021;11(1). doi:10.3390/min11010015

[11] Schuepfer DB, Badaczewski F, Guerra-Castro JM, Hofmann DM, Heiliger C, Smarsly B, et al. Assessing the structural properties of graphitic and non-graphitic carbons by Raman spectroscopy. *Carbon N Y*. 2020;161:359-372. doi:10.1016/j.carbon.2019.12.094

[12] Major GH, Avval TG, Patel DI, Shah D, Roychowdhury T, Barlow AJ, et al. A discussion of approaches for fitting asymmetric signals in X-ray photoelectron spectroscopy (XPS), noting the importance of Voigt-like peak shapes. *Surface and Interface Analysis*. 2021;53(8):689-707. doi:10.1002/sia.6958

[13] Gengenbach T, Major G, Linford M, Easton C. Practical guides for x-ray photoelectron spectroscopy (XPS): Interpreting the carbon 1s spectrum. *Journal of Vacuum Science & Technology A*. 2021;39:013204. doi:10.1116/6.0000682

[14] Rella S, Giuri A, Corcione CE, Acocella MR, Colella S, Guerra G, et al. X-ray photoelectron spectroscopy of reduced graphene oxide prepared by a novel green method. *Vacuum*. 2015;119:159-162. doi:10.1016/j.vacuum.2015.05.008

[15] Moeini B, Linford MR, Fairley N, Barlow A, Cumpson P, Morgan D, et al. Definition of a new (Doniach-Sunjic-Shirley) peak shape for fitting asymmetric signals applied to reduced graphene oxide/graphene oxide XPS spectra. *Surface and Interface Analysis*. 2022;54(1):67-77. doi:https:10.1002/sia.7021

[16] Salvo P, Calisi N, Melai B, Cortigiani B, Mannini M, Caneschi A, et al. Temperature and pH sensors based on graphenic materials. *Biosens Bioelectron*. 2017;91:870-877. doi:10.1016/j.bios.2017.01.062

[17] Wei H, Wang H, Chu H, Li J. Preparation and characterization of slow-release and water-retention fertilizer based on starch and halloysite. *Int J Biol Macromol*. 2019;133:1210-1218. doi:10.1016/j.ijbiomac.2019.04.183

[18] Nambiar AP, Pillai R, Sanyal M, Vadikkeettil Y, Shrivastav PS. A starch based sustainable bio-hybrid composite for surface assimilation of methylene blue: preparation, characterization, and adsorption study. *Environmental Science: Advances*. 2023;2(6):861-876. doi:10.1039/D2VA00274D

[19] Luo P, Zhao Y, Zhang B, Liu J, Yang Y, Liu J. Study on the adsorption of Neutral Red from aqueous solution onto halloysite nanotubes. *Water Res*. 2010;44(5):1489-1497. doi:10.1016/j.watres.2009.10.042

[20] Łapińska A, Grochowska N, Antonowicz J, Michalski P, Dydek K, Dużyńska A, et al. Influence of the filler distribution on PDMS-graphene based nanocomposites selected properties. *Sci Rep*. 2022;12(1):19038. doi:10.1038/s41598-022-23735-3

[21] Toto E, Laurenzi S, Santonicola MG. Flexible nanocomposites based on polydimethylsiloxane matrices with dna-modified graphene filler: Curing behavior by differential scanning calorimetry. *Polymers (Basel)*. 2020;12(10):1-20. doi:10.3390/polym12102301

[22] Tao K, Yang S, Grunlan JC, Kim YS, Dang B, Deng Y, et al. Effects of carbon nanotube fillers on the curing processes of epoxy resin-based composites. *J Appl Polym Sci*. 2006;102(6):5248-5254. doi:10.1002/app.24773

[23] Xu J, Razeeb KM, Roy S. Thermal properties of single walled carbon nanotube-silicone nanocomposites. *J Polym Sci B Polym Phys*. 2008;46(17):1845-1852. doi:10.1002/polb.21519

[24] Ketikis P, Koutsoumpis S, Bokobza L, Georgopoulos D, Georgousis G, Kontou E, et al. *Molecular Dynamics and Thermal Transitions in PDMS/ CNTs Nanocomposites*.; 2016.

[25] Logakis E, Pissis P, Pospiech D, Korwitz A, Krause B, Reuter U, et al. Low electrical percolation threshold in poly(ethylene terephthalate)/multi-walled carbon nanotube nanocomposites. *Eur Polym J*. 2010;46(5):928-936. doi:10.1016/j.eurpolymj.2010.01.023

[26] Pissis P, Klonos P, Kripotou S, Kyritsis A. *Thermal Transitions and Segmental Dynamics in Polymer Nanocomposites*.; 2013.

[27] Sahoo S, Bhowmick AK. Influence of ZnO nanoparticles on the cure characteristics and mechanical properties of carboxylated nitrile rubber. *J Appl Polym Sci*. 2007;106(5):3077-3083. doi:10.1002/app.24832

[28] Laskowska A, M. Z, Boiteux G, Gain O, Marzec A, Maniukiewicz W. Ionic Elastomers Based on Carboxylated Nitrile Rubber (XNBR) and Magnesium Aluminum Layered Double Hydroxide. *Express Polym Lett*. 2014;8:374-386. doi:10.3144/expresspolymlett.2014.42

[29] Cai JH, Huang ML, Chen XD, Wang M. Controllable construction of cross-linking network for regulating on the mechanical properties of polydimethylsiloxane and polydimethylsiloxane/carbon nanotubes composites. *J Appl Polym Sci*. 2022;139(19):52113. doi:10.1002/app.52113

[30] Parizi MJG, Shahverdi H, Roa JJ, Pipelzadeh E, Martinez M, Cabot A, et al. Improving Mechanical Properties of Glass Fiber Reinforced Polymers through Silica-Based Surface Nanoengineering. *ACS Appl Polym Mater*. 2020;2(7):2667-2675. doi:10.1021/acsapm.0c00295

[31] Gorbatikh L, Lomov S V., Verpoest I. Nano-engineered composites: A multiscale approach for adding toughness to fibre reinforced composites. In: *Procedia Engineering*. Vol 10. Elsevier Ltd; 2011:3252-3258. doi:10.1016/j.proeng.2011.04.537

[32] Tian Y, Zhang H, Zhang Z. Influence of nanoparticles on the interfacial properties of fiber-reinforced-epoxy composites. *Compos Part A Appl Sci Manuf*. 2017;98:1-8. doi:10.1016/j.compositesa.2017.03.007

[33] Godara A, Gorbatikh L, Kalinka G, Warrier A, Rochez O, Mezzo L, et al. Interfacial shear strength of a glass fiber/epoxy bonding in composites modified with carbon nanotubes. *Compos Sci Technol*. 2010;70(9):1346-1352. doi:10.1016/j.compscitech.2010.04.010

3. CNTs@ZnO smart nanocomposite for self-healing applications

This chapter provides a comprehensive overview of the materials, synthesis procedures, and characterization techniques employed to develop smart nanocomposites, based on the use of an innovative filler composed of CNTs decorated with ZnO NPs (CNTs@ZnO). Thus, the development of this new hybrid filler and its incorporation in a carboxylate polymer matrix (XNBR) for self-healing applications is herein described.

The chapter is divided in three sections. Section 3.1 presents the synthesis and characterization of CNTs@ZnO through a soft-chemistry approach starting from a zinc precursor that hydrolyses and condensates on the CNTs surface. Section 3.2 investigates the interaction between this hybrid filler and the carboxylic group terminations of stearic acid, used as a polymer model compound to assess the availability of ZnO to form zinc stearate-like complexes, through thermal calorimetric studies (DSC). Lastly, in Section 3.3 CNTs@ZnO were embedded in a XNBR matrix and the resulting nanocomposites were tested in terms of mechanical, electrical and self-healing properties. All the results of the chapter are then summarized in Section 3.4.

3.1 Synthesis of CNTs@ZnO

The synthesis conditions for the preparation of CNTs@ZnO were optimized starting from a literature protocol[1] that employs a soft-chemistry approach to surface functionalize CNTs with ZnO NPs, as illustrated in Scheme 3.1.

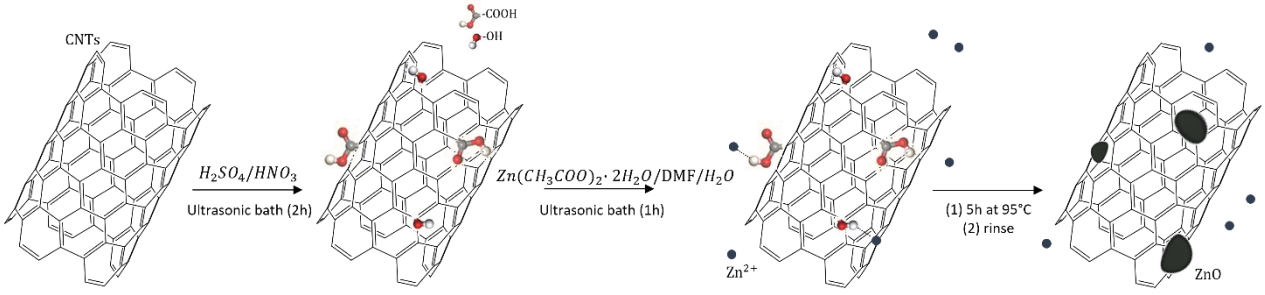

Scheme 3.1 Scheme reaction of CNTs@ZnO synthesis.

The optimized procedure involves two main steps. In the first step, CNTs undergo an acid treatment, necessary to introduce oxygen-containing functional groups (such as hydroxyl, carbonyl, and carboxyl groups) onto their surface, thereby improving their reactivity and ability to interact with the inorganic species. In the second step, ZnO nanocrystals are anchored onto the CNT surface through a precipitation process, starting from a Zn(II) precursor solution. A crucial step is the addition of distilled water into the reaction mixture to promote the transformation of the stable complexes formed between

Zn(II) ions and the solvent (dimethylformamide, DMF)[2], that otherwise hinder the precipitation of ZnO NPs. In fact, the addition of water promotes the hydrolysis reaction of these Zn(II) complexes into the respective hydroxide form, followed by their condensation, ultimately leading to the formation of ZnO NPs, as illustrated in Scheme 3.2.

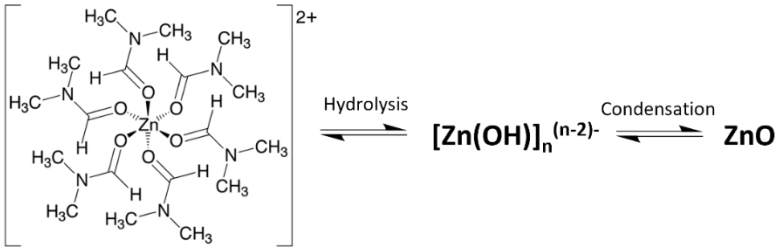

Scheme 3.2 Schematic representation of the hydrolysis and condensation of Zn^{2+} ions upon water addition.

3.1.1 Experimental procedure of CNTs@ZnO

Materials

Carbon Nanostructure Pellets ATHLOS100 (CNTs) were purchased from Cabot Corporation. N,N-Dimethylformamide (DMF, 99 %) was purchased from Thermo Fisher Scientific. Sulfuric acid (H_2SO_4, 95-97 %) was purchased from Sigma Aldrich. Nitric acid (HNO_3, 68 % v/v) was purchased from VWR Chemicals. Zinc acetate dihydrate ($Zn(CH_3COO)_2{\cdot}2H_2O$, 98.0-101.0 %) and sodium hydroxide pellets (NaOH, 98 %) were purchased from Alfa Aesar. Hydrophilic PTFE membranes (diameter 47 mm, pores 0.2 µm) were purchased from Pall Corporation.

Synthesis

In a single-neck round-bottom flask, 500 mg of pristine CNTs were dispersed in 47 mL of a solution of H_2SO_4/HNO_3 in a ratio 3:1 v/v using an ultrasonic bath for 2 h. The reaction mixture was filtrated in a vacuum filtration system with a hydrophilic PTFE membrane and washed with an aqueous solution of NaOH 0.1 M, till the CNTs aqueous dispersion reached neutral pH. The resulting product (CNTs_TA) was then dried overnight in a vacuum oven at 80 °C.

For the second step, in a round-bottom flask, 40 mg of CNTs_TA were dispersed in 200 mL of DMF and a suitable amount of distilled water by ultrasonication (Table 3.1). Then, two different amounts of $Zn(CH_3COO)_2{\cdot}2H_2O$ were added to the reaction mixture (Table 3.1) and sonicated for 1 h. The amounts of Zn(II) precursor were selected in order to obtain a final ZnO loading equal to 80 and 90 weight percentage (wt.%) of the total sample weight ($CNTs@ZnO_{80\%}$ and $CNTs@ZnO_{90\%}$, respectively). The flask was heated at 95 °C and left under stirring for 5 h. The reaction mixture was filtered in a vacuum filtration

system with a hydrophilic PTFE membrane and washed several times with distilled water and EtOH. The final product was dried in a vacuum oven at 80 °C overnight.

Table 3.1 Resume of reagents quantity used for the synthesis of CNTs@$ZnO_{90\%}$ and CNTs@$ZnO_{80\%}$, starting from 40 mg of CNTs_TA.

	H_2O (mL)	$Zn(CH_3COO)_2 \cdot 2H_2O$ (g)
CNTs@$ZnO_{90\%}$	8.0	0.92
CNTs@$ZnO_{80\%}$	4.5	0.46

3.1.2 Characterization of CNTs@ZnO

FTIR

The effective modification of the CNTs surface through the acid treatment has been evaluated by FTIR analysis, by comparing the spectrum of CNTs_TA with that of bare CNTs (Figure 3.1).

In both spectra, the main features result from the O–H vibrations at 3444 cm^{-1} and 1640 cm^{-1}, which are assigned respectively to the stretching and bending mode of the O–H groups of adsorbed water. The peak at 1398 cm^{-1} observed in both spectra can be connected to the C=C aromatic vibrations typical for the CNTs structure. Besides, the intense peaks at 1091 and 802 cm^{-1} can be assigned to the symmetric and asymmetric Si–O–Si stretching of the fiberglass contained in the CNTs (< 7% from the Technical Data Sheet).

After the oxidative treatment, the main difference is connected to the appearance of a new peak with low intensity at 1736 cm^{-1}, likely due to the carbonyl stretching of the arising -COOH groups. Besides, the intensity of the peak at 1261 cm^{-1}, refereed to the O–C=O vibration of oxygen-based groups, increases, suggesting that a higher amount of these groups is formed.

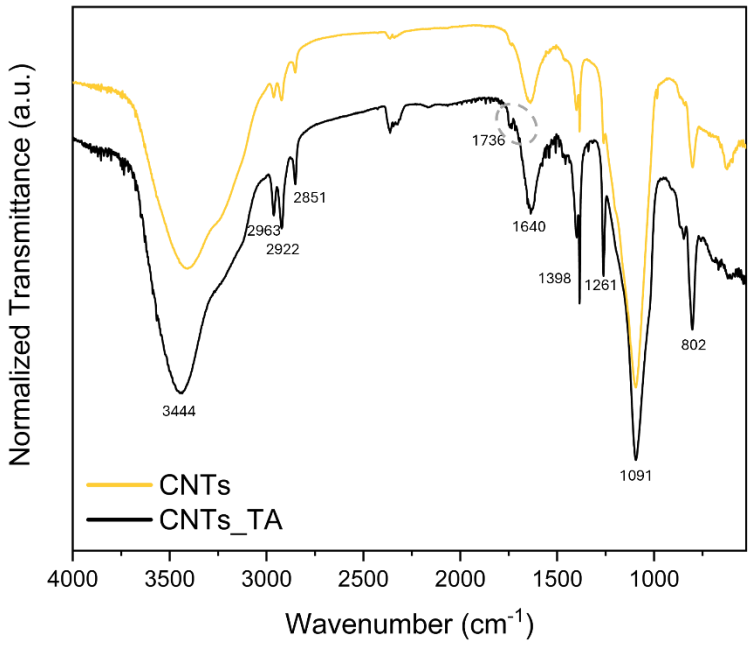

Figure 3.1 ATR-FTIR spectra of pristine CNTs and CNTs_TA.

TEM

TEM images were first collected on bare CNTs (Figure 3.3 a-b), showing a smooth surface structure with a diameter of 9 ± 2 nm and a length greater than 5 µm, in according to the Technical Data Sheet provided by Cabot. After the surface functionalization with ZnO, TEM micrographs of CNTs@ZnO evidence the formation of additional NPs on the surface of CNTs with an average size of 20 ± 3 nm by using both the ZnO loadings (Figure 3.2 b-c). No phase separation or segregation was detected in both CNTs@ZnO samples, meaning that the growth of ZnO NPs mainly occurs on the surface of CNTs.

To validate the experimental procedure used to prepare CNTs@ZnO and in particular highlight the key role of water in the growth of ZnO NPs, TEM analysis was also performed on CNTs@ZnO prepared without adding H_2O during the synthesis of ZnO NPs. Interestingly, as shown in Figure 3.2a, no ZnO NPs were obtained, confirming that water is crucial to promote the condensation of the zinc precursor to ZnO on the CNTs surface.

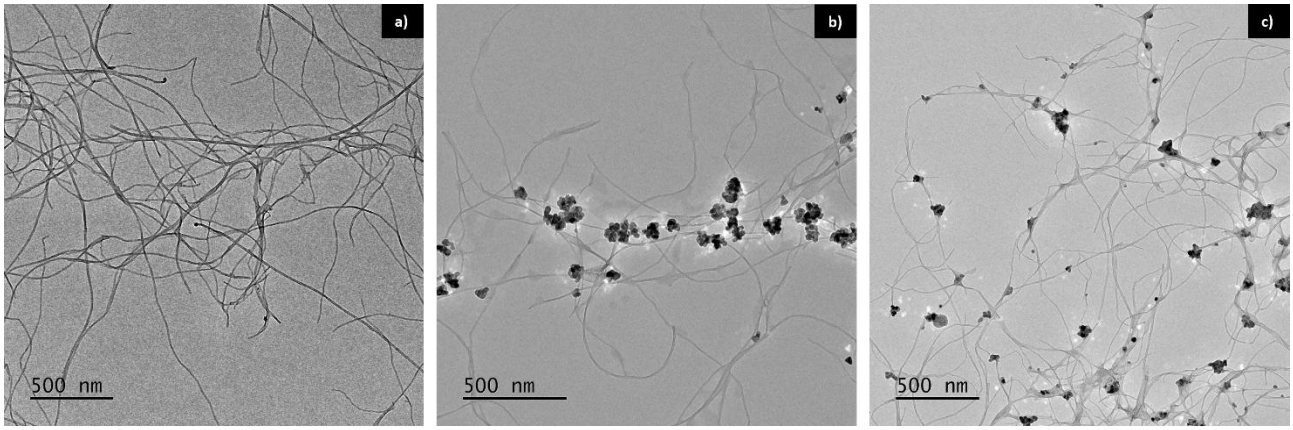

Figure 3.2 TEM images of CNTs@ZnO synthesis without water (a) or with the addition of X mL of H_20 for $CNTs@ZnO_{90\%}$ (b) and $CNTs@ZnO_{80\%}$ (c).

Only for $CNTs@ZnO_{90\%}$ sample, the growth of ZnO NPs was also investigated as a function of the reaction mixture at different time intervals after 1 h of sonication starting when the temperature is increased (t = 0 min, 30 min, 1 h, 2 h, 5 h). The NPs formation and their morphological evolution during the reaction (T = 95 °C) was followed by TEM analysis. At the initial stage (t = 0), the CNTs are mainly coated with an amorphous phase (green arrows), while only a few ZnO (yellow arrows) can be observed (Figure 3.3 c–d), in contrast to the clean surface of the pristine CNTs_TA shown in Figure 3.3 a–b. After 30 minutes, the amorphous phase is still present; however, Figures 3.3e–f reveal the formation of aggregates exhibiting a flower-like morphology (brown arrows), indicating the onset of ZnO crystal growth. At 1 h, these aggregates spread across the CNT surface, and well-defined crystalline ZnO NPs with an average diameter of ≈ 20 nm become clearly distinguishable (Figure 3.3 g–h). After 2 h, the NPs progressively assemble into larger aggregates (blue arrows, Figure 3.3 i–j) yielding in ZnO NPs with diameters exceeding 50 nm at 5 h of reaction (purple arrows, Figure 3.3 k–l).

This TEM time-analysis highlights the progressive evolution from amorphous phases to crystalline ZnO nanostructures, with particle size and morphology strongly dependent on the reaction time. Such findings provide important insight into the nucleation and growth mechanism of ZnO on CNTs, suggesting a transition from isolated nuclei to aggregated crystalline domains.

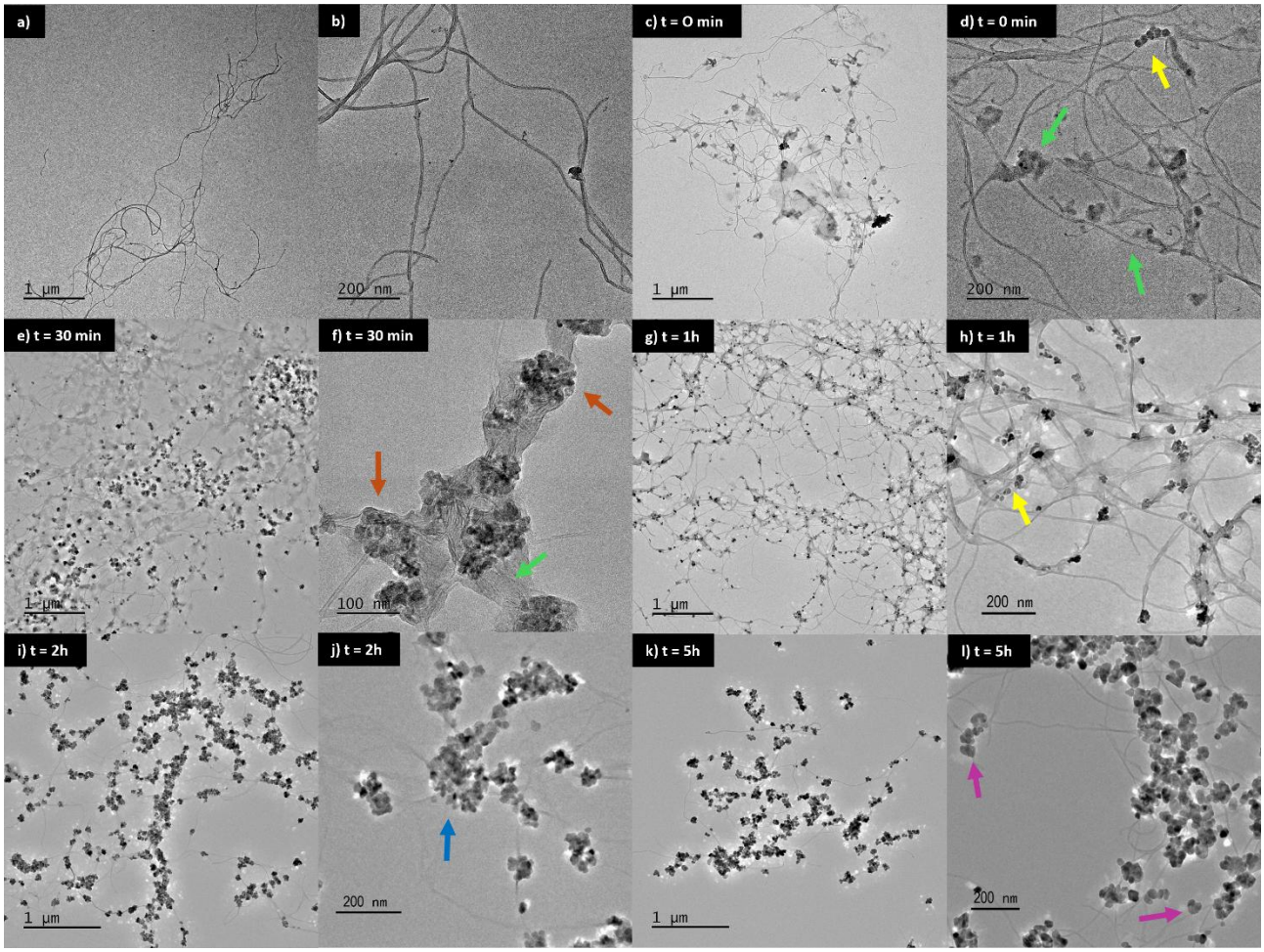

Figure 3.3 TEM micrographs at two different magnifications of a-b) CNTs_TA and CNTs@$ZnO_{90\%}$ at different reaction times: c-d) 0 min; e-f) 30 min; g-h) 1h; i-j) 2h; k-l) 5h.

XRD

The structural characterization of CNTs@ZnO has been performed using powder-XRD. Although CNTs are generally classified as non-crystalline materials, their periodic structure produces a characteristic XRD pattern (Figure 3.4) with two distinct large peaks around 25.6° and 42.8°. The peak at ≈ 25°, known as the Bragg reflection (002), is typically sharper and more intense than the (100) peak at ≈ 43° [3,4]. The XRD patterns of both CNTs@$ZnO_{90\%}$ and CNTs@$ZnO_{80\%}$ additionally display the characteristic peaks of ZnO, consistent with the crystalline wurtzite phase belonging to the hexagonal $P6_3mc$ space group[5].

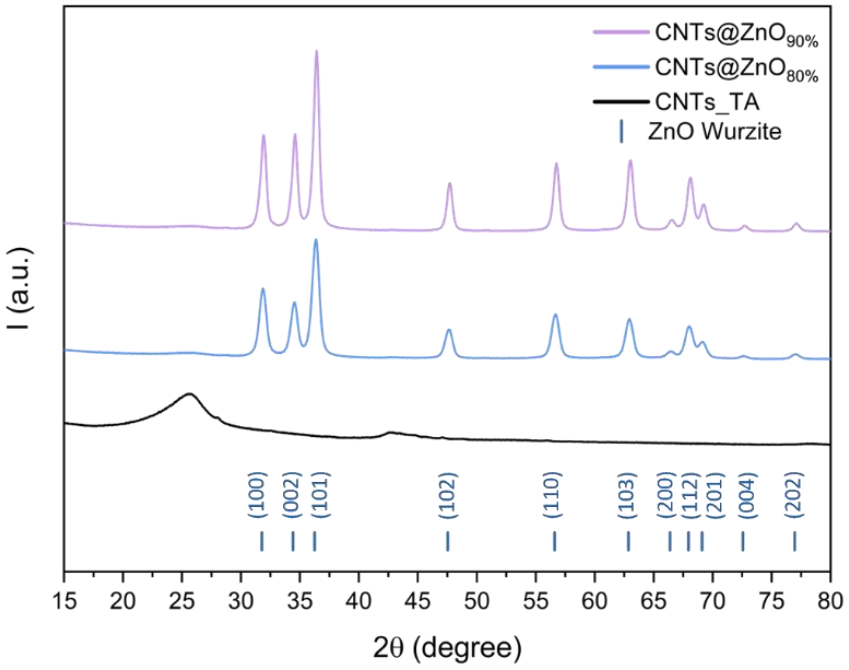

Figure 3.4 XRD pattern of CNTs_TA, CNTs@$ZnO_{90\%}$ and CNTs@$ZnO_{80\%}$. At the bottom, reference diffractograms of ZnO Wurtzite is reported.

XRF

XRF analysis has been performed to investigate the composition of both bare CNTs and CNTs@ZnO. According to the spectra shown in Figure 3.5, the most intense peaks in the spectra of CNTs and CNTs_TA are observed at 6.40 and 7.06 keV and correspond to Kα1 and Kβ1 signals of iron. Besides, small traces of calcium and nickel can be detected from the peaks at 3.69 and 7.48 keV, respectively, as shown in Figure 3b. These metal traces may be derived from the catalyst used for the CNTs synthesis through chemical vapor deposition process[6]. In the case of CNTs@ZnO, the two major peaks are related to the presence of zinc (8.64 and 9.57 keV, Kα1 and Kβ1 respectively) and the intensities of the other metals become very low, confirming the predominant presence of zinc in the functionalized samples and the successful surface functionalization.

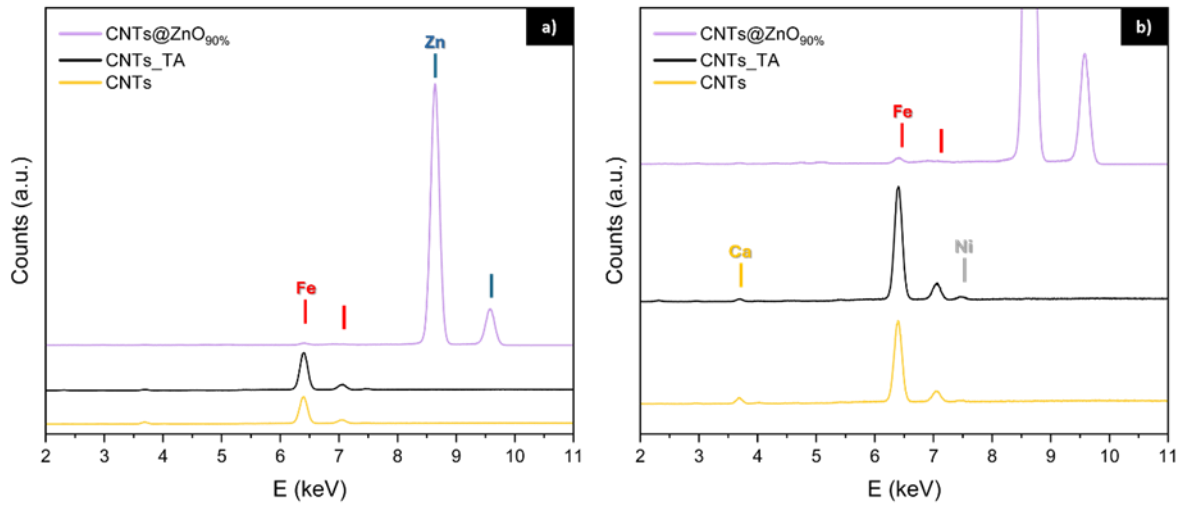

Figure 3.5 a) XRF spectra of CNTs, CNT_TA and CNTs@$ZnO_{90\%}$ reported as an example for functionalized CNTs@ZnO samples; b) magnification of the spectra on the y-axis to highlight low intensity peaks.

ICP-OES and TGA

ICP-OES analysis has been performed to quantify the amount of ZnO anchored on the CNTs structure. In Table 3.2 are reported the nominal moles and weight percentages of zinc and zinc oxide, calculated with respect to the final weight of the filler, starting from the nominal amount of zinc precursor used in the reaction. These nominal values of Zn and ZnO perfectly fit with those obtained by ICP-OES analysis.

Moreover, TGA analysis has been used to evaluate both the thermal stability of the CNTs and to confirm the effective amount of ZnO loaded onto CNTs in both CNTs@$ZnO_{90\%}$ and CNTs@$ZnO_{80\%}$ samples (Figure 3.6). Regarding their thermal stability, virgin CNTs show a significant weight loss at temperatures of 600-700 °C and a residual mass of ≈ 5 wt.% at 1000 °C. This observation suggests the presence of inorganic species that do not degrade at high temperatures and can be reasonably connected to metal-based species (mainly oxides) that are formed starting from the metal contaminations already highlighted by XRF results. Moreover, from the Technical Data Sheet, a low content of fiberglass (< 7 wt.%) which remains at the end of the analysis is present in the samples. Differently, CNTs_TA shows an initial step of weight loss till 150 °C where the weight loss is related to the release of physically adsorbed water. Then, the dominant weight loss (start ≈ 250 °C) occurs at lower temperature with respect to the bare CNTs and is ascribable to the loss of the oxygen in the functional groups and, at higher temperature, to the decomposition of the structure[7]. The residual mass for CNTs_TA is almost 10 wt.% and may be partially assigned to the metal contaminations and the fiberglass content, as observed before. Moreover, the acid treatment could leave some inorganic salts (e.g. Na_2SO_4) that degrade at temperature higher than 1000 °C and is responsible for this higher inorganic residue at 1000 °C.

After the addition of ZnO, the residual mass at 1000 °C further increases, due to the presence of a higher content of inorganic material in the total mass of the samples. In these materials it can be assumed that this residual at 1000 °C is for the vast majority connected to ZnO NPs, whereas the contributions due to metal traces and the fiberglass content become negligible, based on the amount of Zn precursor used in the synthesis; moreover, it can be reasonably supposed that the salt sulphate detected in CNTS_TA has been probably fully eliminated with the additional washing steps performed during the ZnO anchoring procedure. Thus, based on these assumptions, the TGA thermographs were used to estimate the amount of ZnO in the CNTs@ZnO samples starting from the residual mass at 1000 °C. The TGA results confirmed the values obtained from the ICP-OES analysis on both the samples with different ZnO content, as shown in Table 3.2.

Table 3.2 Nominal and calculated (ICP and TGA) content of Zn (expressed in mmol) and ZnO (expressed as weight percentage, wt.%) for CNTs@$ZnO_{90\%}$ and CNTs@$ZnO_{80\%}$.

	Zn		*ZnO*		
	Nominal (mmol)	Measured ICP (mmol)	Nominal (wt.%)	Measured ICP (wt.%)	Measured TGA (wt.%)
CNTs@$ZnO_{90\%}$	3.5 ± 0.1	3.7 ± 0.2	89.0 ± 0.4	90.8 ± 0.3	88.9 ± 0.1
CNTs@$ZnO_{80\%}$	1.9 ± 0.2	1.8 ± 0.1	79.7 ± 0.3	78.3 ± 0.5	79.4 ± 0.2

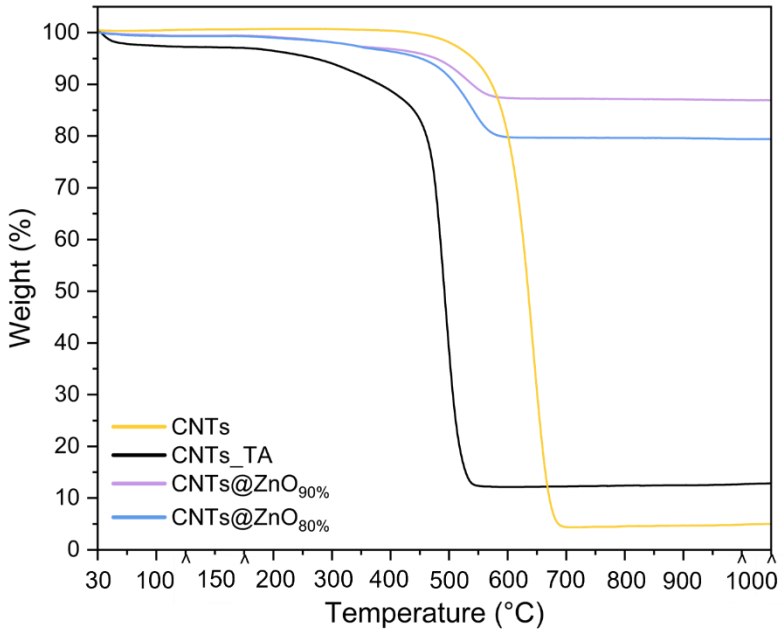

Figure 3.6 TGA thermograms of CNTs bare, CNTs_TA, CNTs@$ZnO_{90\%}$ and CNTs@$ZnO_{80\%}$.

Nitrogen physisorption

The nitrogen adsorption–desorption isotherms of CNTs_TA, CNTs@$ZnO_{90\%}$ and CNTs@$ZnO_{80\%}$ are presented in Figure 3.7.

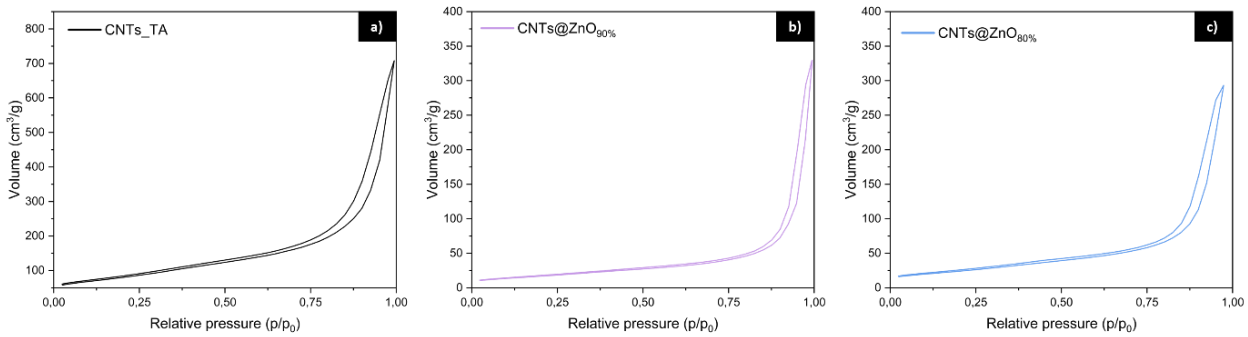

Figure 3.7 Nitrogen adsorption-desorption (77K) isotherms of a) CNTs_TA; b) CNTs@$ZnO_{90\%}$; c) CNTs@$ZnO_{80\%}$.

According to the IUPAC classification[8], the isotherms correspond to type IV with an H3-type hysteresis at high relative pressures. This behaviour indicates the presence of a limited amount of mesopores, most likely arising from interparticle voids within the network structure and CNTs agglomerates. For p/p_0 values above 0.8, a marked increase in adsorbed volume is observed, which can be attributed to the filling of these interparticle spaces. None of the three curves reach a plateau at a relative pressure of 1, suggesting incomplete mesopore filling.

The specific surface area (SSA) and pore volume were calculated using the Brunauer–Emmett–Teller (BET) and Barrett-Joyner-Halenda (BJH) models, and the results are reported in Table 3.3. The SSA of CNTs_TA confirms the value (i.e. 150-350 $m^2\ g^{-1}$) given by the data sheet of the commercial CNTs used for the synthesis of the filler. However, the SSA values of both CNTs@$ZnO_{90\%}$ and CNTs@$ZnO_{80\%}$ strongly decreases compared to CNTs_TA, most likely due to the gathering of some of the CNTs in bundles during the growth of ZnO NPs, as well as a reduction in the cumulative pore volume.

Table 3.3 Specific surface area and cumulative pore volume of the samples based on BET and BJH models.

	CNTs_TA	CNTs@$ZnO_{90\%}$	CNTs@$ZnO_{80\%}$
SSA_{BET} (m^2/g)	290 ± 7	64 ± 2	90 ± 2
Pore volume (cc/g)	1.092	0.517	0.462

In fact, the pore size distribution, obtained from the BJH model applied to the desorption branch, shows the average pore diameters of 24, 34, and 21 nm for CNTs_TA, CNTs@$ZnO_{90\%}$, and CNTs@$ZnO_{80\%}$, respectively (Figure 3.8). These values are probably related to some holes in the network formed by the aggregation of the CNTs, that can be occluded after ZnO NPs decoration.

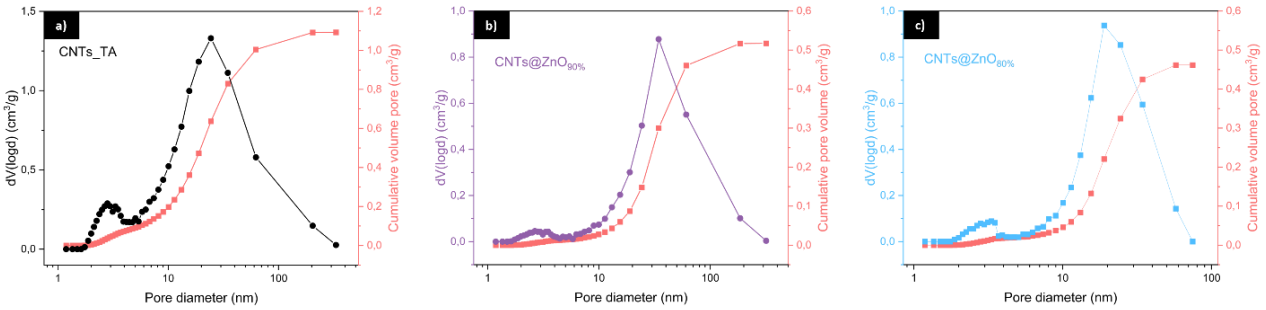

Figure 3.8 Cumulative pore volume and pore size distribution curves of a) CNTs_TA; b) CNTs@$ZnO_{90\%}$; c) CNTs@$ZnO_{80\%}$ calculated by BJH model for mesoporous analysis.

XPS

The XPS spectra were acquired for CNTs_TA and CNTs@ZnO to study the surface chemistry of the samples giving information about the elements and their chemical state.

The Zn $2p_{3/2}$ core level (Figure 3.9e) exhibits a significant positive binding-energy shift of approximately + 1.2 eV relative to bulk ZnO, compatible with the + 0.9 eV shift previously reported for similar systems[9], and indicative of strong interactions at the ZnO/CNT interface. This shift is commonly attributed to the partial surface reduction and oxygen-deficient regions generated by the reactive carbon precursor, accompanied by the formation of interfacial Zn–C–O species. The presence of two characteristic loss features at 1035 and 1037.2 eV confirms that ZnO remains in the hybrid structure. The C 1s spectrum of CNTs@ZnO (Figure 3.9b) further reveals a chemically heterogeneous interface. The dominant component at 284.4 eV is characteristic of sp^2 carbon associated with the graphitic backbone of the nanotubes (grey curve). A distinct feature at 285.2 eV (blue curve) is assigned to an interfacial state arising from electronic coupling between CNTs and ZnO, providing direct spectroscopic evidence of charge transfer across the heterointerface and consistent with the Zn 2p BE shift. Additional contributions at 286.0 and 289.8 eV (green and yellow curves) correspond to C–O/COOH and C=O species, respectively, likely originating from oxygenated groups of CNT surface. The O 1s core level (Figure 3.9d) corroborates this picture, showing a main component at 531.2 eV (blue curve) attributable to lattice oxygen in ZnO and confirming the retention of the oxide framework despite strong interfacial interactions. Higher-BE components provide additional evidence of chemical modification: 533.0 and 534.1 eV assigned to C–O/COOH and C=O groups, respectively (green and grey curves).

The spectra of CNTs_TA confirm that the features ascribed to the ZnO/CNT interface disappear in the absence of ZnO. In the C 1s region (Figure 3.9a), the envelope is dominated by the sp^2 peak at 284.4 eV (grey curve), and the interfacial component at 285.2 eV is absent, confirming its origin in ZnO–CNT coupling. Acid oxidation instead produces a strong contribution at ≈ 286.0 eV from C–O/COOH groups and only a weak high-BE tail at ~289.8 eV associated with C=O species, reflecting the introduction of hydroxyl, ether, and carboxyl functionalities on the CNT surface. The O 1s spectrum (Figure 3.9c) mirrors this behaviour: it is dominated by oxygen bound to carbon, including a prominent C–O/COOH peak near 533 eV and a higher-BE feature at 534.1 eV attributable to carbonyl or anhydride species. The Zn–O lattice signal at ~ 531.2 eV, prominent in the hybrid filler, is absent here. A minor feature at ≈ 531.3 eV is likely due to quinone-like C=O groups rather than Zn–O.

Overall, these results demonstrate that after the acid treatment an extensive oxidative functionalization of the CNT surface is detected. Besides, the presences of the 285.2 eV C 1s component in the hybrid filler reinforces the successful decoration of CNTs with ZnO NPs and the ZnO/CNT interfacial interaction.

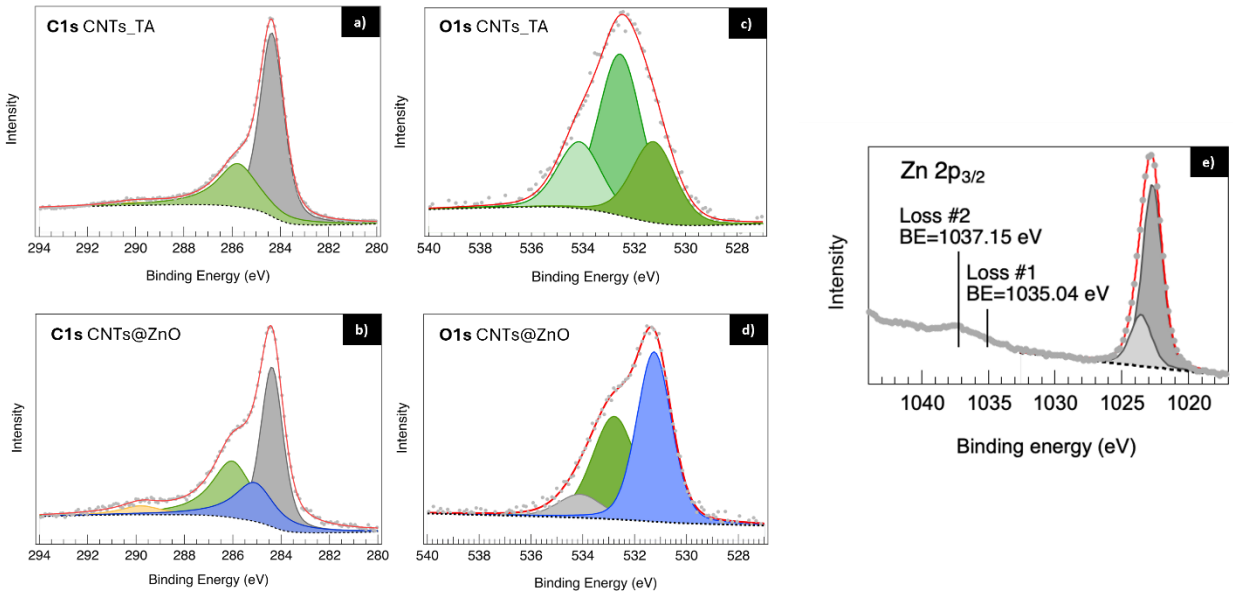

Figure 3.9. XPS spectra of C1s region for a) CNTs_TA and c) CNTs@ZnO; O 1s region for c) CNTs_TA and d) CNTs@ZnO; and Zn $2p_{3/2}$ region for CNTs@ZnO.

3.2 Interaction of CNTs@ZnO with SA

To assess the availability of ZnO NPs attached to the CNTs surface to interact with the carboxylic groups of a polymeric matrix, stearic acid (SA) was selected as a model compound representative of a simple carboxylate-terminated polymer. The interaction was investigated using differential scanning calorimetry (DSC) which enables the detection of thermal transitions and the evaluation of possible reaction products[10].

Procedure

SA (purchased from Sigma Aldrich) and CNTs@$ZnO_{90\%}$ (1:1 molar ratio) were mixed in a mortar to obtain a homogeneous powder. Samples of 5–8 mg were weighed on a microbalance, compressed to ensure good thermal contact, and sealed in 40 µL aluminum pans with pierced lids. The DSC program consisted of six steps: (i) heating from 30 to 200 °C at 5 °C min^{-1}; (ii) isothermal step at 200 °C for 2 min; (iii) cooling to 30 °C at 5 °C min^{-1}; (iv) isothermal step at 30 °C for 2 min; (v) second heating to 200 °C at 5 °C min^{-1}; (vi) second cooling to 30 °C at 5 °C min^{-1}. All measurements were performed under a nitrogen flow of 50 mL min^{-1}. A TGA analysis has been also performed on the mixture CNTs@ZnO/SA (1:1) and on three different references helpful to evaluate the different contributions: SA, CNTs@ZnO and commercial zinc stearate (purchased from Sigma Aldrich). The TGA program is reported in the Appendix.

3.2.1 Results of SA+CNTs@ZnO

DSC

To investigate the interaction between ZnO NPs anchored on CNTs and the carboxylate groups of a polymeric matrix, the complexation of ZnO with SA was examined as a model system using DSC, after mechanically mixing. The results were compared to that obtained by the interaction of bare ZnO and SA[10]. During the first heating ramp, a weak endothermic peak between 55–60 °C was detected, likely associated with water evaporation. This was followed by a more pronounced endothermic event at ≈ 70 °C, corresponding to the melting of free SA (Figure 3.10a, grey band)[11]. Notably, the SA melting was followed by an exothermic peak at 102 °C, attributed to surface interactions between molten SA and ZnO, initiated as the liquid acid approached the filler surface (purple band). Finally, an additional endothermic peak near 133 °C was assigned to the melting of reaction product (i.e zinc stearate–like complex) formed through the surface interaction between ZnO NPs and SA (light blue band).

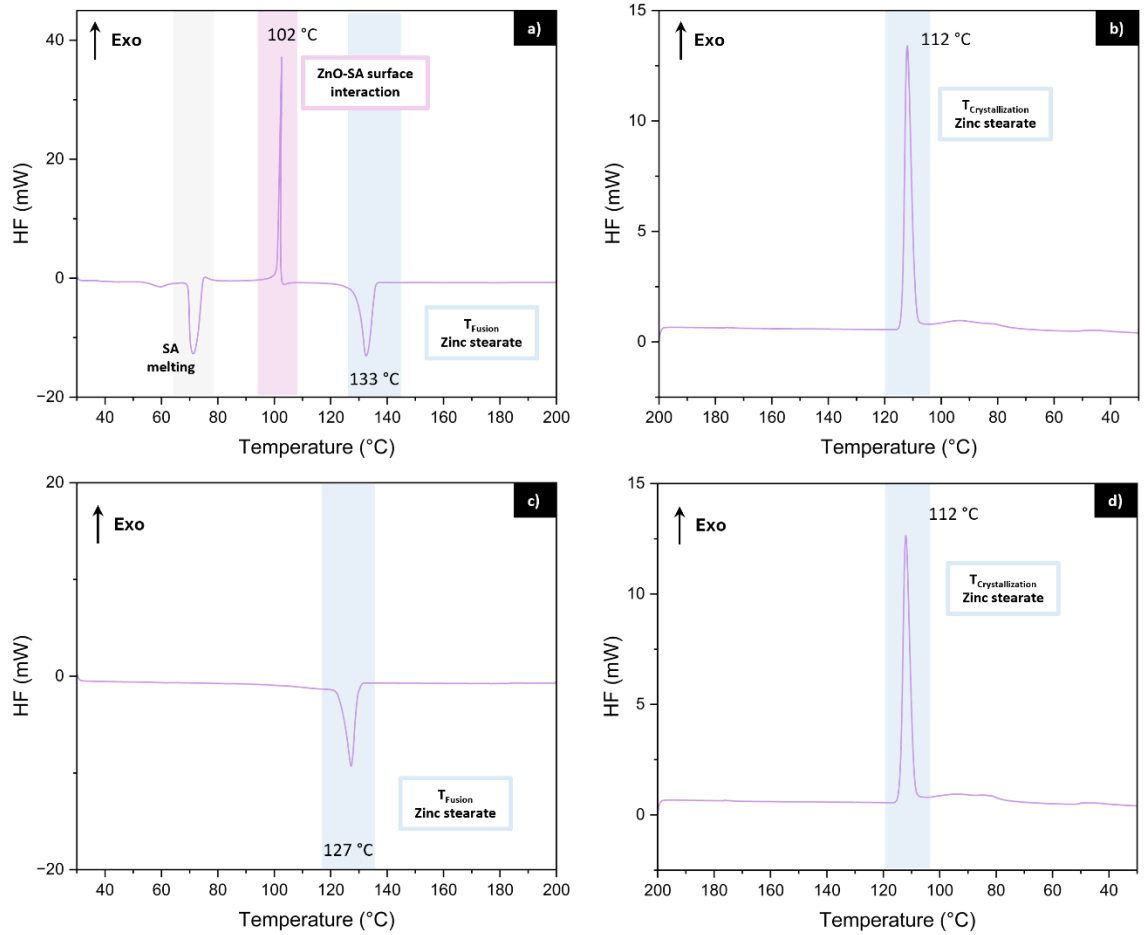

Figure 3.10 DSC curves of heating and cooling ramps of first (a-b) and second (c-d) cycle of CNTs@$ZnO_{90\%}$ mixed with stearic acid (1:1 molar ratio).

During the cooling ramp (Figure 3.10b), the DSC curve displayed a sharp endothermic peak at ≈112 °C (light blue band), attributed to the crystallization of the Zn–SA complex. Interestingly, no crystallization peak of unreacted SA has been detected, suggesting the complete consumption of it in the zinc stearate formation process. Similar behaviour has been observed in the following heating and cooling cycles, proving the stability of the complex (Figure 3.10 c-d).

Overall, these findings demonstrate that ZnO NPs decorating the CNT framework can interact with carboxylate groups, thereby anticipating their potential reactivity with -COOH groups of the matrix.

TGA

To further elucidate the nature of the reaction products formed through the ZnO–SA interaction, TGA analysis was carried out on the mixture CNTs@ZnO/SA to evaluate the different contributions. The resulting TGA thermogram was compared to that of bare SA, bare CNTs@ZnO and commercial zinc stearate (purchased from Sigma Aldrich), that may arise as reaction product between ZnO and SA. These TGA profiles are reported in Figure 3.11.

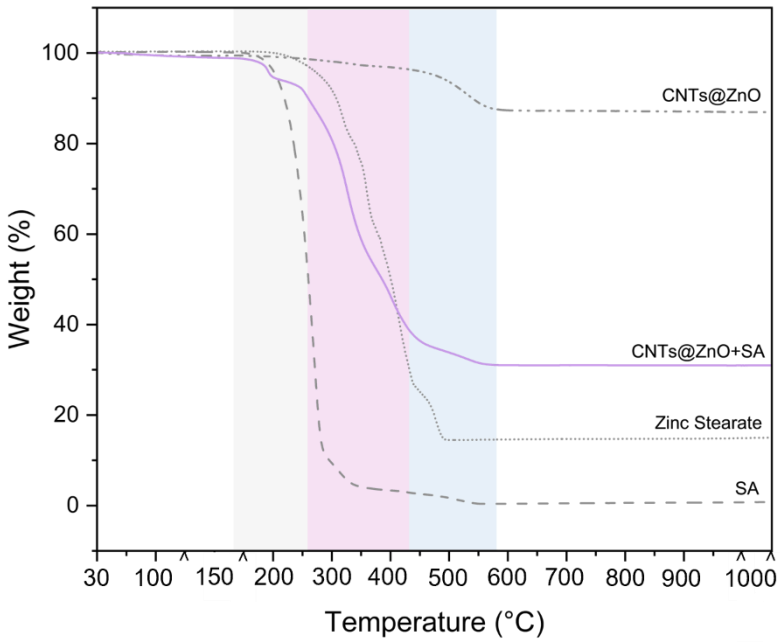

Figure 3.11 Thermal degradation profiles of the mixture CNTs@ZnO+SA compared to SA, zinc stearate and bare CNTs@ZnO.

In detail, TGA curve of CNTs@ZnO interacting with SA reveals three different contributions to the weight loss. The one at higher temperature (light blue band) refers to the hybrid filler CNTs@ZnO degradation (T_{onset} = 450 °C). The one at lower temperature (grey band) is ascribable to a small amount of residual SA (T_{onset} = 150 °C) that did not completely interact with ZnO. Interestingly, also a contribution related to zinc stearate (T_{onset} = 240 °C) is detected in after CNTs@ZnO/SA interaction, suggesting the formation of zinc stearate-like complexes during the interaction between ZnO NPs decorating the filler surface and carboxylic groups of stearic acid[10].

3.3 Functional properties of XNBR composite

This section provides a detailed description of the synthesis of the CNTs@ZnO polymer composite and the evaluation of its self-healing properties. The composite was fabricated using a solvent casting method, in which the filler was dispersed within the polymer matrix before the mixture was poured into a mold [12]. Under controlled temperature conditions, solvent evaporation was promoted, leading to the curing of the matrix.

As a suitable polymer matrix, a commercial carboxylated acrylonitrile butadiene natural rubber latex (XNBR), in which the polymer component is 41 wt.% (from the technical data sheet) was selected. For this reason, water has been chosen as solvent and PEG-1500 was added to facilitate the dispersion of the filler[12,13]. The curing of the matrix occurs thanks to the presence of ZnO NPs anchored on the CNTs structure which promote ionic interactions between Zn^{2+} species and the carboxylate groups of the matrix.

Two different hybrid filler loadings (1 and 2 wt.%) were employed in the preparation of the CNTs@ZnO/XNBR composites. For comparison, a reference sample was also prepared by directly mixing ZnO nanoparticles and CNTs_TA into the XNBR matrix (denoted as CNTs+ZnO/XNBR). The quantities of the two fillers were adjusted to ensure that the ZnO content in the reference compound matched that of the CNTs@ZnO/XNBR composites.

The intrinsic self-healing mechanism, as described in Section 1.2.2.1, is based on a thermoreversible association–dissociation process involving Zn^{2+}–COOH ionic clusters. Accordingly, the self-healing behaviour of the composites was evaluated by introducing controlled damage (i.e., a macroscopic cut) and subsequently applying a thermal healing protocol designed to promote the reformation of ionic pairs within the polymer matrix.

3.3.1 Experimental procedures

Materials

Chemigun® Latex 550 (XNBR) was purchased from Synthomer. Zinc oxide (ZnO, wurtzite) was purchased from Zincol Ossidi. Polyethylene glycol (PEG-1500) was purchased from BASF Pharma.

Composites preparation

In a becker, PEG and filler were dispersed in distilled water using an ultrasonic probe for 15 minutes. Subsequently, XNBR latex has been added to the suspension under stirring and let for 1.5 h. The mixture

was transferred in a Teflon mode and put in an oven at 80°C overnight. The quantities of all reagents used in the different formulations are resumed in Table 3.4.

Table 3.4 Content of all the reagents employed in the XNBR composite formulations.

				Fillers		
	XNBR latex (mL)	H_2O (mL)	PEG (mg)	ZnO (mg)	CNTs_TA (mg)	CNTs@ZnO (wt.%)
CNTs@ZnO_1	10	5	100	-	-	1
CNTs@ZnO_2	10	7	200	-	-	2
CNTs+ZnO_1	10	5	100	0.0375	0.0042	-
CNTs+ZnO_2	10	7	200	0.0751	0.0083	-

DMA analysis and healing protocol

For the self-healing procedure, the samples were cut in half macroscopically, then placed in contact inside a petri dish and finally treated in an oven at 80 °C for 5 hours (Figure 3.12).

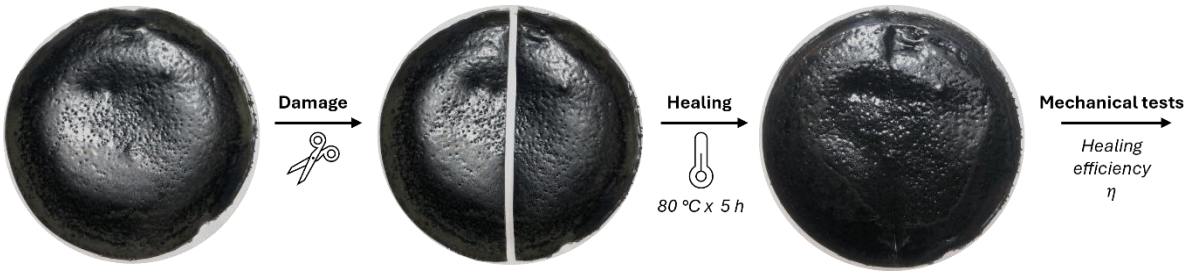

Figure 3.12 Protocol utilized for healing efficiency determination.

The healing efficiency of the polymer composites was calculated as the retention of mechanical properties (storage modulus value, E', derived from DMA analysis) of healed sample compared with those of the virgin material:

$$\eta\ (\%) = \frac{E'_{healed}}{E'_{virgin}} * 100 \qquad \text{(Eq.1)}$$

DMA was performed by an apparatus working in tensile mode. A pre-load of 0.1 N was applied to all the samples, and then an isothermal time sweep test (30 °C for 5 min) has been carried out applying a sinusoidal strain with frequency of 1 Hz and amplitude of 0.2 %. All the values of storage modulus, E', and the calculated healing efficiency, η, are reported in Table 3.5.

3.3.2 Characterization of XNBR nanocomposite with CNTs@ZnO filler

The CNTs@ZnO system was selected to facilitate ionic crosslinking via interactions between the carboxyl groups of XNBR and the Zn^{2+} ions of the oxide nanoparticles. During curing, ionic domains are formed that function as active crosslinking sites. These clusters immobilize segments of the polymer chains, thereby governing the mechanical response of the material.

Figure 3.13 presents the ATR-FTIR spectra of pristine XNBR latex and of all the composite formulations investigated in this study.

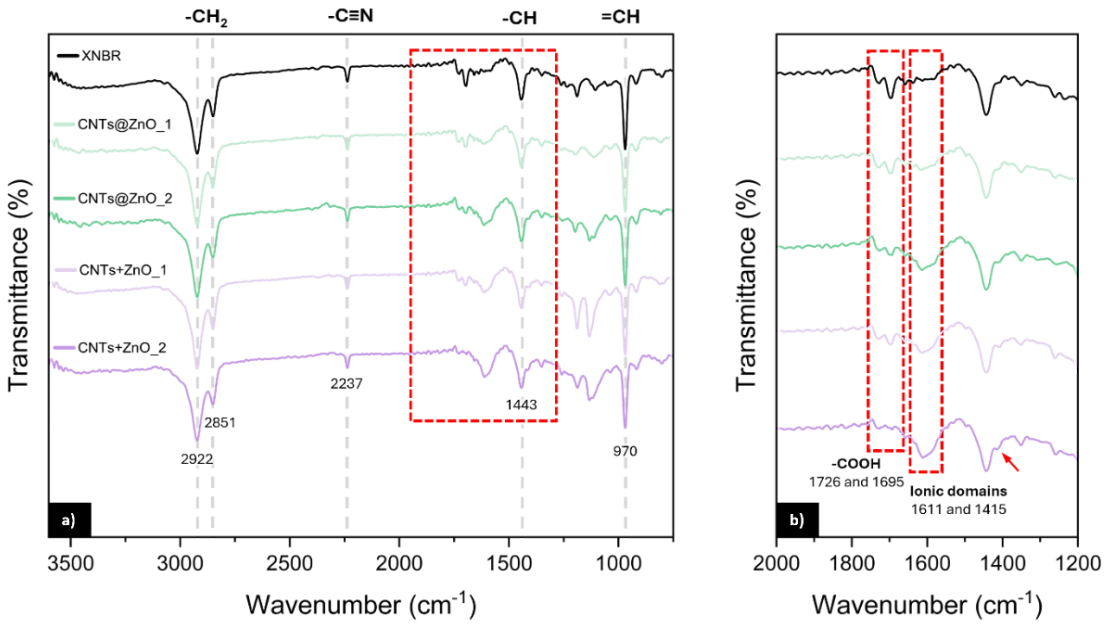

Figure 3.13 (a) ATR-FTIR spectra of pristine XNBR and of all formulations containing CNTs@ZnO hybrid filler or ZnO nanoparticles combined with CNTs_TA (CNTs+ZnO); (b) Enlarged view of the spectral region associated with carboxylate functional groups and the formation of ionic domains.

In the XNBR matrix, several characteristic absorption bands can be identified: the asymmetric and symmetric $–CH_2$ stretching vibrations at 2922 and 2851 cm^{-1}, respectively; the nitrile –C≡N stretching at 2237 cm^{-1}; the C=O stretching of –COOH groups at 1726 cm^{-1}; the band at 1695 cm^{-1} associated with intramolecularly hydrogen-bonded carboxylic acids; the –CH in-plane deformation of methylene groups at 1443 cm^{-1}; and the peak at 970 cm^{-1} corresponding to the out-of-plane deformation of =CH groups linked to C=C double bonds[14,15].

Following curing in the presence of varying loadings of CNTs@ZnO hybrid filler or ZnO nanoparticles combined with CNTs_TA dispersed in the matrix, a noticeable decrease in the intensity of the absorption bands associated with –COOH groups at 1726 and 1695 cm^{-1} is observed (Figure 7b). In addition, two new bands appear at 1611 and 1415 cm^{-1}, which can be assigned to the asymmetric and symmetric stretching vibrations of zinc carboxylate ion pairs[16,17]. Although these bands exhibit relatively low

intensity, likely due to the modest ZnO content employed (1–2 wt.%), their presence confirms the interaction between Zn^{2+} ions, originating from both ZnO nanoparticles and ZnO anchored onto the CNT structure, and the carboxylic groups of XNBR.

3.3.3 Functional properties of the composite

In order to assess the capability of the designed filler in imparting self-repairing properties to the XNBR elastomeric material, the recovery of the storage modulus was measured by DMA analysis.

The results firstly revealed that, increasing the filler loading, the storage modulus increases thus unveiling the reinforcement capability of the CNTs@ZnO hybrid filler (Figure 3.14). Moreover, the E' value after healing was retained after the repairing process, resulting in calculated healing efficiencies (η) generally satisfactory for all the tested compounds (Table 3.5).

Table 3.5 Values of storage modulus, E', and healing efficiency, η, for the XNBR composites.

	E' (MPa)	η (%)
CNTs@ZnO_1	2.59 ± 0.03	97.3
CNTs@ZnO_1_healed	2.52 ± 0.05	
CNTs@ZnO_2	2.77 ± 0.02	85.4
CNTs@ZnO_2_healed	2.34 ± 0.02	
CNTs+ZnO_1	2.33 ± 0.04	98.7
CNTs+ZnO_1_healed	2.30 ± 0.03	
CNTs+ZnO_2	2.54 ± 0.02	107.0
CNTs+ZnO_2_healed	2.72 ± 0.02	

Specifically, the CNTs@ZnO_1 sample exhibits a healing efficiency (η) close to 100%, whereas a slightly reduced value is observed for the CNTs@ZnO_2 composite containing 2 wt.% hybrid filler. This decrease can be attributed to the higher filler content, which may induce inhomogeneous dispersion and less efficient interfacial compatibilization, underscoring the need for further optimization of both synthesis and incorporation processes.

In the case of CNTs+ZnO/XNBR composites, only the CNTs+ZnO_2 formulation shows a deviation from this trend, displaying a healing efficiency exceeding 100%. This suggests that the healing process may actually reinforce the material's structural integrity. Such behaviour is likely due to additional crosslinking reactions or enhanced interfacial interactions promoted during thermal treatment, leading to improved mechanical performance [18].

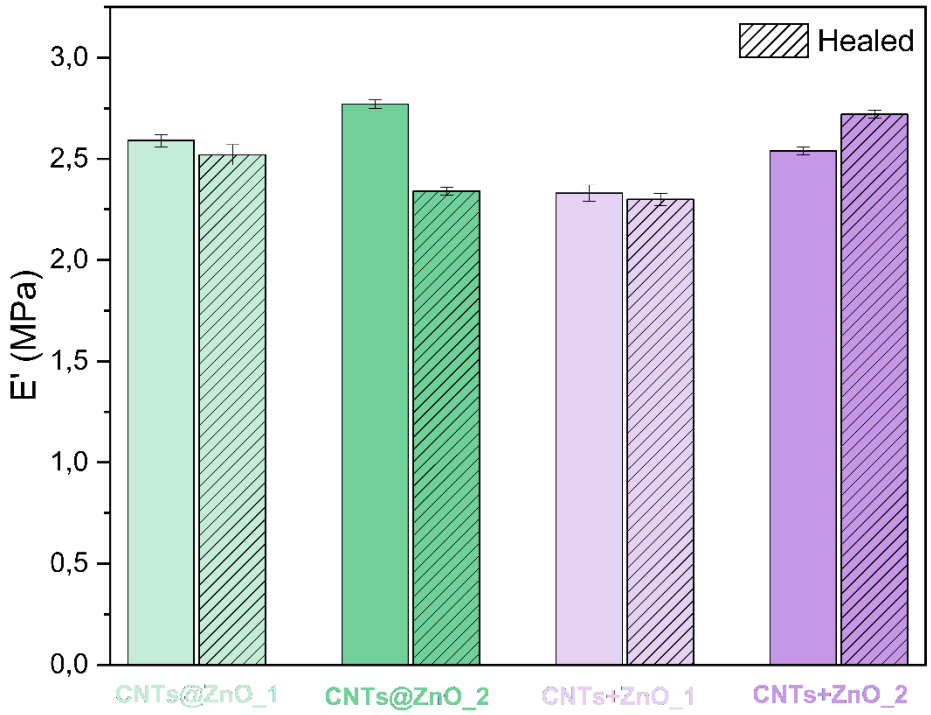

Figure 3.14 Storage modulus values obtained for the composites before and after the healing protocol.

Notably, the storage moduli of these composites are lower than those of materials incorporating CNTs@ZnO fillers with comparable ZnO contents (Figure 3.14). This observation highlights the synergistic contribution of the hybrid filler, whose overall performance exceeds that of the individual constituents. The enhanced mechanical behaviour is attributed to the effective dispersion of ZnO nanoparticles throughout the polymer matrix, promoted by the CNT network, which serves as a conductive scaffold and an efficient carrier for Zn species. As a result, ZnO aggregation is minimized, leading to a more homogeneous distribution and increased effectiveness of the inorganic phase.

3.4 Conclusion

In this chapter, a novel hybrid filler based on carbon nanotubes decorated with zinc oxide nanoparticles (CNTs@ZnO) was successfully synthesized, characterized, and incorporated into a carboxylated nitrile butadiene rubber (XNBR) matrix for the development of self-healing nanocomposites. The synthesis via a soft-chemistry route enables the homogeneous growth of ZnO nanoparticles on the CNT surface, as confirmed by TEM, XRD, XPS, and TGA analyses. The results demonstrate that water addition plays a crucial role in promoting ZnO nucleation and crystallization, while maintaining good dispersion and intimate interfacial contact between the two components. The chemical and structural investigations confirm strong interfacial interactions between CNTs and ZnO, as evidenced by the binding energy shifts in XPS spectra and the reduced surface area observed by BET analysis. The DSC and TGA studies carried out on the CNTs@ZnO–stearic acid model system further demonstrate the capability of ZnO sites to react with carboxylic groups, forming zinc–carboxylate complexes analogous to zinc stearate.

When embedded in the XNBR matrix, CNTs@ZnO significantly improves the mechanical properties of the composites, confirming its reinforcing effect. The hybrid filler also acts as an in-situ curing agent, promoting ionic crosslinking between Zn^{2+} and –COOH groups. Dynamic mechanical analysis reveals excellent self-healing efficiency for all the composites. However, slightly lower healing efficiencies are observed at higher filler loadings (2 wt.%), likely due to reduced dispersion and interfacial compatibility, suggesting the need for optimization of the synthesis and processing parameters.

Overall, this study demonstrates that CNTs@ZnO is an effective multifunctional filler capable of imparting both reinforcement and self-healing functionality to elastomeric matrices. The synergistic interaction between the conductive CNT framework and the ionic ZnO domains provides a promising foundation for the development of next-generation smart elastomeric nanocomposites with autonomous repair capability and potential applications in flexible and dynamic engineering components such as O-rings and seals.

References

[1] Lu MM, Cao WQ, Shi HL, Fang XY, Yang J, Hou ZL, et al. Multi-wall carbon nanotubes decorated with ZnO nanocrystals: mild solution-process synthesis and highly efficient microwave absorption properties at elevated temperature. *J Mater Chem A Mater*. 2014;2(27):10540-10547. doi:10.1039/C4TA01715C

[2] ITO M, MITSUHASHI R, MIKURIYA M, SAKIYAMA H. Crystal Structure of a Trigonally Compressed Hexakis-DMF Zinc(II) Complex. *X-ray Structure Analysis Online*. 2016;32:21-22. doi:10.2116/xraystruct.32.21

[3] Abdulrazzak F, Alkaim A, Hussein F. Behavior of X-Ray Analysis of Carbon Nanotubes. In: ; 2019:90. doi:10.5772/intechopen.85156

[4] Das R, Abd Hamid SB, Ali M, Yongzhi W. Carbon Nanotubes Characterization by X-ray Powder Diffraction – A Review. *Curr Nanosci*. 2015;11. doi:10.2174/1573413710666140818210043

[5] Morkoç H, Özgür Ü. *Zinc Oxide: Fundamentals, Materials and Device Technology*.; 2009. doi:10.1002/9783527623945

[6] Vir Singh M, Kumar Tiwari A, Gupta R. Catalytic Chemical Vapor Deposition Methodology for Carbon Nanotubes Synthesis. *ChemistrySelect*. 2023;8(32):e202204715. doi:https://doi.org/10.1002/slct.202204715

[7] Krieg AS, King JA, Odegard GM, Leftwich TR, Odegard LK, Fraley PD, et al. Mechanical Properties and Characterization of Epoxy Composites Containing Highly Entangled As-Received and Acid Treated Carbon Nanotubes. *Nanomaterials*. 2021;11(9). doi:10.3390/nano11092445

[8] Thommes M, Kaneko K, Neimark A V., Olivier JP, Rodriguez-Reinoso F, Rouquerol J, et al. Physisorption of gases, with special reference to the evaluation of surface area and pore size distribution (IUPAC Technical Report). *Pure and Applied Chemistry*. 2015;87(9-10):1051-1069. doi:10.1515/pac-2014-1117

[9] Biyela PN, Ndwandwe OM, Rigoni F, Pagliara S, Sangaletti L, Carlino E, et al. Controlled synthesis of carbon nanostructures using aligned ZnO nanorods as templates. *Carbon N Y*. 2012;50. doi:10.1016/j.carbon.2012.07.034

[10] Mostoni S, Milana P, D'Arienzo M, Dirè S, Callone E, Cepek C, et al. Studying stearic acid interaction with ZnO/SiO2 nanoparticles with tailored morphology and surface features: A benchmark for better designing efficient ZnO-based curing activators. *Ceram Int*. 2023;49(14):24312-24321. doi:10.1016/j.ceramint.2022.12.013

[11] Kruger FWH, McGill WJ. A DSC study of curative interactions. I. The interaction of ZnO, sulfur, and stearic acid. *J Appl Polym Sci*. 1991;42(10):2643-2649. doi:10.1002/app.1991.070421002

[12] Bhirde A, Patel S, Sousa A, Patel V, Molinolo A, Ji Y, et al. Distribution and Clearance of PEG-Single-Walled Carbon Nanotube Cancer Drug Delivery Vehicles in Mice. *Nanomedicine (Lond)*. 2010;5:1535-1546. doi:10.2217/nnm.10.90

[13] Sun Y, Li Z. Aqueous dispersion of single walled carbon nanotubes stabilized by PEG modified diperylene bisimide and their application as an antibacterial agent. *RSC Adv*. 2017;7(42):26125-26129. doi:10.1039/C7RA03570E

[14] Jin SH, Park YB, Yoon KH. Rheological and mechanical properties of surface modified multi-walled carbon nanotube-filled PET composite. *Compos Sci Technol*. 2007;67(15):3434-3441. doi:10.1016/j.compscitech.2007.03.013

[15] Thommes M, Kaneko K, Neimark A, Olivier J, Rodriguez-Reinoso F, Rouquerol J, et al. Physisorption of gases, with special reference to the evaluation of surface area and pore size distribution (IUPAC Technical Report). *Pure and Applied Chemistry*. 2015;87. doi:10.1515/pac-2014-1117

[16] Long DA. Infrared and Raman characteristic group frequencies. Tables and charts. *Journal of Raman Spectroscopy*. 2004;35(10):905. doi:10.1002/jrs.1238

[17] Utrera-Barrios S, Araujo-Morera J, Pulido de Los Reyes L, Verdugo Manzanares R, Verdejo R, López-Manchado MÁ, et al. An effective and sustainable approach for achieving self-healing in nitrile rubber. *Eur Polym J*. 2020;139:110032. doi:10.1016/j.eurpolymj.2020.110032

[18] Utrera-Barrios S, Martínez MF, Mas-Giner I, Verdejo R, López-Manchado MA, Hernández Santana M. New recyclable and self-healing elastomer composites using waste from toner cartridges. *Compos Sci Technol*. 2023;244:110292. doi:https://doi.org/10.1016/j.compscitech.2023.110292

4. GFRPs: spray-coating modification with rGO and EMAA

Over the past decade, incorporating thermoplastic additives has emerged as an effective strategy for developing self-healing fiber-reinforced polymers (FRPs). These materials heal through molecular interdiffusion of thermoplastic chains when heated above their glass transition temperature (Tg)[1]. This approach offers several advantages, including compatibility with commercial resins, multiple healing cycles, and ease of implementation.

Depending on the miscibility between the thermoplastic and thermoset phases, systems can be classified as miscible or immiscible. Among immiscible systems, poly(ethylene-co-methacrylic acid) (EMAA) is one of the most widely used self-healing agents. EMAA can form covalent bonds with epoxy matrices and, upon heating, expands significantly more than the resin, generating pressure and flow that promote crack filling and interfacial rebonding.

Various techniques have been developed to integrate EMAA into composites, including the use of particles, meshes, membranes, films, patches, and fibers[2–5]. The most effective configuration involves embedding EMAA between fiber layers, which enhances both stiffness and healing capability. However, industrial scalability remains a challenge due to complex processing steps (e.g. cryogenic grinding or extrusion) and non-uniform EMAA distribution, which can limit healing to localized regions[6].

In this work, the physical surface modification of GF has been reached through a versatile spray coating technique with rGO, to impart electrical conductivity to the system, and with EMAA that act as healing agent in the composite[7]. EMAA pellets are first dissolved with rGO in tetrahydrofuran (THF) and then precipitated in an ice batch, yielding a stable nanoparticle suspension suitable for spray application. After the GF modification, three different laminates have been produced through Hand Lay-up method: GF neat (as a reference), GF sprayed with EMAA and rGO (sGF), and GF sprayed with EMAA and rGO with also rGO embedded in the matrix (sGF/rGO). All the steps of the process are schematized in Figure 4.1.

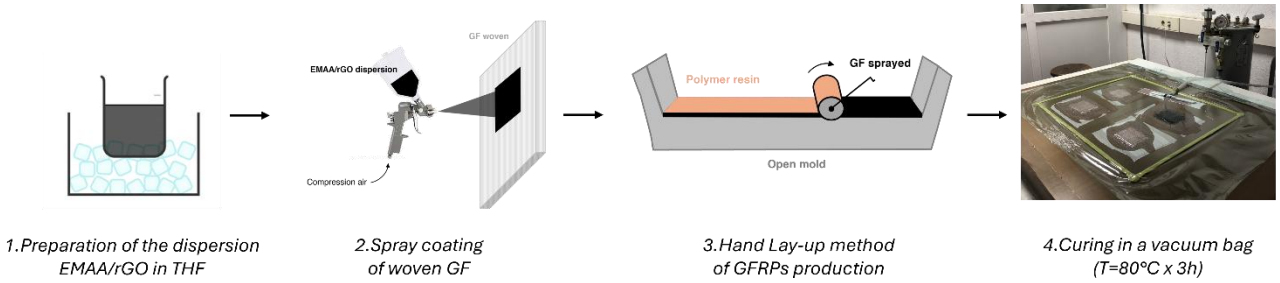

Figure 4.1 Schematic representation of all the steps of manufacturing process of the GFRPs.

The matrix chosen for the production of the laminates (Resoltech 1050) is an epoxy resin of bisphenol F diglycidyl ether (DGEBF 50–80%), bisphenol A diglycidyl ether (DGEBA 10–40%) and 1,6-hexanediol diglycidyl ether (Figure 4.2), and an amine curing agent based on a mixture of polyoxyalkane amine, aminoethylpiperazine and diethylenetriamine (Resoltech 1053S), with a ratio of 100:35. This system was chosen for its low viscosity (251 mPa*s) resulting in an effortlessly fiber impregnation by manual lamination, infusion or injection of large parts.

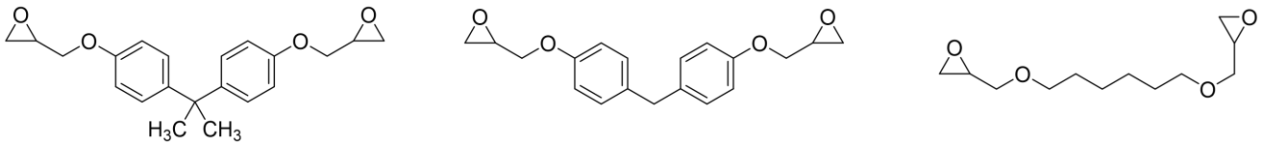

Figure 4.2 Mixture of the epoxy matrix Resoltech 1050 employed in the laminates production.

4.1 Experimental procedure of sprayed GFRPs composites

Materials

Reduced graphene oxide (AV-70, rGO) was purchased from Avanzare Materials. NUCREL™ 925 (Ethylene Methacrylic Acid Copolymer, EMAA) was purchased from Dow Corning. Epoxy resin and Hardener 1050/1053S were purchased from Resoltech. Tetrahydrofuran (99.5 %, THF) was purchased from Thermo Scientific. E-Glass fibers (LT600 E10B-0/90 BIAXIAL E GLASS FABRIC-127CM) were purchased from Metyx Composites.

Procedure

The first step in the procedure involves the spray-coating modification of the GFs. 1.04 g of rGO (3 wt.% relative to the resin) was dispersed in 288.6 mL of THF. Then, 1.728 g of EMAA (5 wt.% relative to the resin) was added to the mixture (0.006 g mL^{-1}) and dispersed using an ultrasonic bath at 60 °C for 30 min. Once the polymer was dissolved, the mixture was cooled in an ice bath turning from black to milky grey, indicating the formation of EMAA nanoparticles[8]. Consequently, the solution was sprayed onto the glass fiber surface (bidirectional woven of 15 x 20 cm cut with electrical scissors) using an air spray gun AB931 (RS PRO) with a 0.22 L tank and a 0.3 mm nozzle. The solution was maintained dispersed through sonication during the coating process to prevent agglomeration and sedimentation. The air gun was cleaned after every two or three sprays to prevent the nozzle from clogging. The coated GF (sGF) was dried at 60 °C in an oven for 2 h.

The second step of the procedure is the 4-ply laminates production through the Hand Lay-up method. Firstly, the mixture epoxy/hardener was prepared though mixing and sonication to eliminate air trapped that leads to voids inside the final composite compromising the mechanical properties. In the case of the laminate with rGO dispersed in the matrix, the mixture (i.e. rGO/epoxy/hardener) was mixed with an asymmetrical centrifuge (FlackTek SpeedMixer™, model DAC 150.1 FVZ-K) for 4 cycles of 2 min at 1800 rpm to reach a good homogeneity. The quantity of matrix to use in the manufacturing process was calculated with a ratio 70:30 of GF and epoxy, respectively. After the manual impregnation of the fibres conducted with the support of a rolling pin, the 4-ply laminates were set on a heated mould and cured at 80 °C for 3 h with vacuum bag to compact the laminate and remove the excess of matrix, as shown in Figure 4.1.

The laminates were then cut with a precision cutting machine with cooling system, NEURTEK BRILLANT 220, equipped with a diamond cutting disc with a thickness of 1.20 mm. The test specimens were cut for the healing and mechanical tests (i.e. three-point flexural, interlaminar shear strength and impact). All the standards and specimen's dimensions for the different tests are reported in the specific sections of the Appendix.

Table 4.1 Composition of the three different laminates produced with spray coating method (* weight percentage referred to the resin).

	Sprayed		*In the matrix*
	EMAA (wt.%)*	**rGO (wt.%)***	**rGO (wt.%)***
GF	-	-	-
sGF	5	3	-
sGF/rGO	5	3	2

4.2 Characterizations of the laminates

SEM

The morphology of the EMAA and rGO dispersion, before being exploited in spray coating process, has been studied with SEM analysis considering rGO as a reference. The typical wrinkled, thin and smooth surface of reduced graphene oxide flakes is highlighted in Figure 4.3 a-b (yellow arrows). Contrarily, the presence of EMAA leads to the formation of a thicker layer with a rougher and less-wrinkled surface full of prominences (red arrows) that may indicate the formation of a continuous amorphous phase of polymer and rGO (Figure 4.3 c-d).

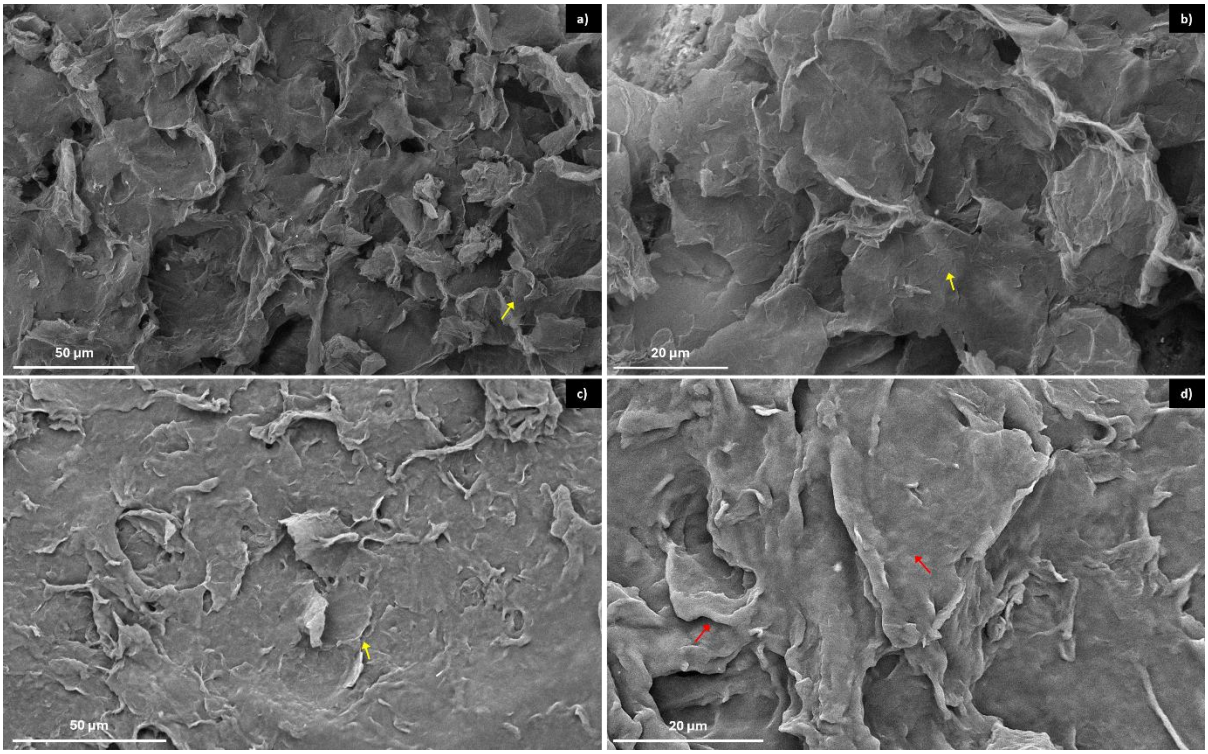

Figure 4.3 SEM images at different magnifications of a-b) rGO, and c-d) EMAA/rGO dispersion.

Taking into account this morphological aspect, the EMAA/rGO coating on the GF surface has been evaluated. The single fibers are uniformly coated with a continuous polymer/rGO layer, creating a continuous and homogeneous surface covering (Figure 4.4a). Moreover, EMAA/rGO mixture is visible both on the fiber surfaces and as aggregates bridging between them (Figure 4.4b) as expected from a coating technique applied directly to a bidirectional woven. This evidence indicates that the spray-coating process not only enhanced the surface roughness of the fibers but also offered a scalable and efficient method for incorporating EMAA/rGO into the GF composite.

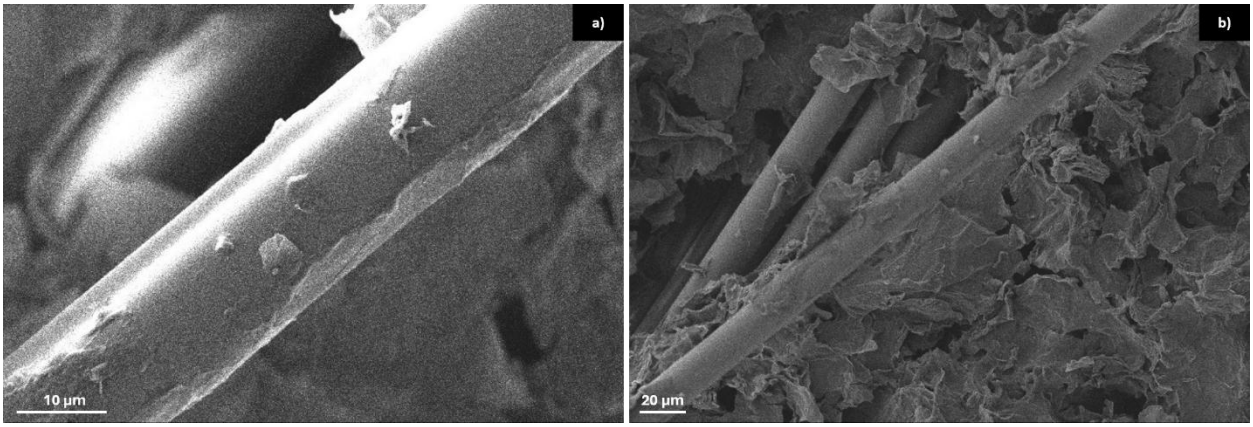

Figure 4.4 SEM images at different magnifications of sGF.

Mechanical tests

The mechanical properties of the laminates were studied to evaluate the effect of the EMAA/rGO modification. For each sample, five specimens were tested, and the average values are presented in Table 4.2 with the GF weight percentage and the thickness of the laminates. The curves for F3P and ILSS are shown in Figure 4.6.

Table 4.2 Mechanical properties of the three samples prepared through Hand Lay-up method.

	% GF	Thickness (mm)	*F3P*		*ILSS*	*Impact*
			σ_{max} (MPa)	E_f (MPa)	τ_{12} (MPa)	a_{cu} (kJ m^{-2})
GF	72.8	2.51 ± 0.04	257 ± 15	11 ± 1	22 ± 3	35 ± 4
sGF	69.7	2.52 ± 0.06	207 ± 32	11 ± 1	20 ± 1	17 ± 3
sGF/ rGO	59.1	3.7 ± 0.2	149 ± 14	4.2 ± 0.4	16 ± 2	11 ± 3

The analysis of the fiber content in the laminates reveals that the GF wt.% closely matches the nominal 70 wt.% for all samples, except for the laminate containing rGO dispersed within the matrix. In this latter case, the increased viscosity of the epoxy/rGO mixture (i.e. 2072 mPa*s) likely hindered proper resin flow and fiber impregnation during the lay-up process and restricted compaction and excess resin removal during vacuum bagging[9]. This resulted in poorer fiber wetting, reduced fiber packing density, and retention of more matrix in the laminate, leading to a higher overall matrix content and, consequently, an increased laminate thickness. This observation suggests that the addition of rGO significantly affects the rheological behaviour of the resin system, which can in turn influence the fiber–matrix ratio, the degree of void formation, and the overall mechanical performance of the composite. Therefore, controlling the dispersion state of rGO and the processing viscosity becomes critical to ensure uniform impregnation and to avoid structural inhomogeneities in the final laminate.

The mechanical characterization of the modified laminates provides important insights into the effects of rGO and EMAA on the structural performance of GFRPs. The incorporation of EMAA and rGO through spray-coating did not significantly alter the mechanical response of the composites compared to the neat reference, as the variations in flexural strength (σ_{max}), flexural modulus (E_f) and interlaminar shear strength (τ_{12}) remained within experimental uncertainty. This indicates that the spray-coating process itself does not compromise the fiber–matrix interfacial adhesion or the overall load transfer efficiency.

However, when rGO was also introduced into the epoxy matrix (sGF/rGO), a notable reduction in both flexural modulus and interlaminar shear strength was observed. This behavior can be attributed to the increased viscosity of the epoxy/rGO mixture, which likely hindered complete fiber impregnation,

leading to the presence of voids and microstructural heterogeneities. These defects, together with potential rGO agglomeration, may have acted as stress concentrators, reducing the effective stiffness and promoting interlaminar delamination[10].

The Charpy impact results follow a similar trend: the incorporation of EMAA and rGO slightly decreases the impact resistance (a_{cu}), further supporting the hypothesis of reduced interfacial bonding and possible structural imperfections within the laminate. Moreover, the visual analysis of the specimens after the test suggests that a different type of damage occurred. Both samples sGF and sGF/rGO show a delamination of the composite (Figure 4.5 b-c, yellow arrows), while GF sample displays a crack in the middle of the specimen.

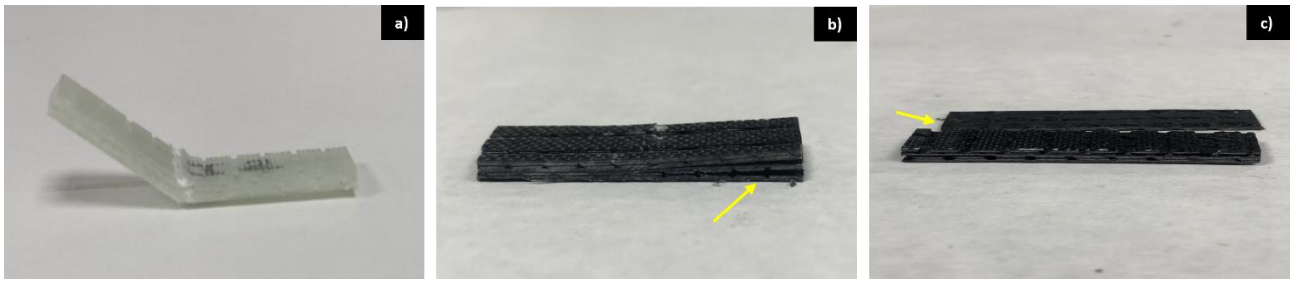

Figure 4.5 Specimens of a) GF, b) sGF, and c) sGF/rGO after the Charpy impact test.

Overall, the mechanical tests demonstrate that while rGO and EMAA surface modification does not significantly reinforce the mechanical strength of GFRPs, it enables functional enhancements without critically compromising their structural integrity. Optimization of the dispersion process and control of viscosity during lamination could further improve the mechanical performance of such multifunctional composites.

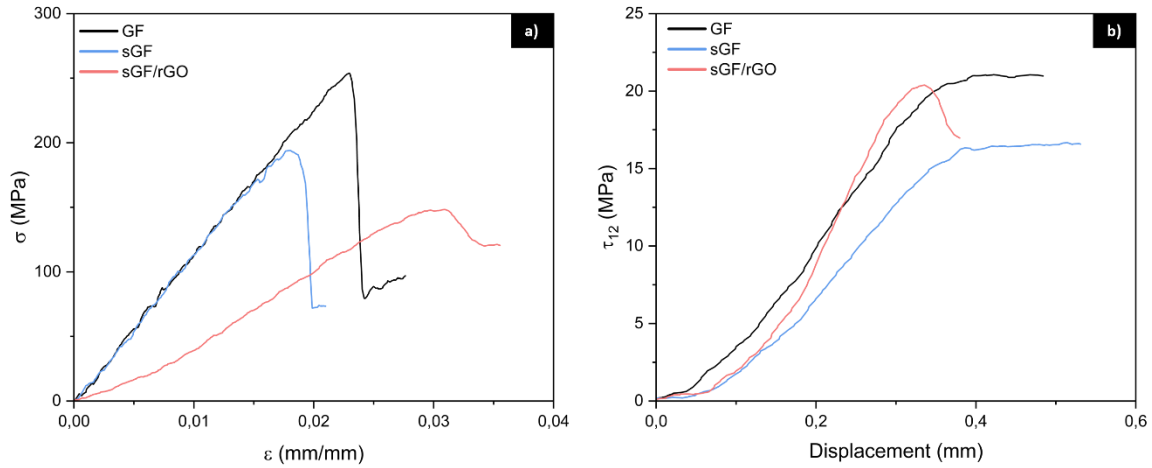

Figure 4.6 a) F3P and b) ILSS representative curves for the samples GF, sGF, and sGF/rGO.

Electrical conductivity

To perform resistivity measurements, a four-probe model was used: the outer probes inject a constant current at the desired intensity, while the inner probes measure the potential difference that develops. The contact between the probe and the sample must be stable and offer low resistance to current flow. Thus, copper strip electrodes were used to ensure proper electrical contact as direct connection using the crocodile clips commonly used in multimeters was found to be inadequate due to the sample's thickness and surface roughness. The electrodes were fixed to the sample using an adhesive mixed with silver conductive paint, forming stable and highly conductive interfaces (Figure 4.7).

The distance between the probes measuring the potential difference is highly significant. It is necessary to always maintain the same distance so that the results are comparable. In this work, the central electrodes were placed at a centre-to-centre distance of 10 mm, corresponding to the characteristic length used for calculating resistivity. This spacing ensured uniform current distribution within the measurement region while minimizing edge effects and contact interference. Meanwhile, the position of the outer electrodes does not affect the measurement. Once the measurements have been obtained, the resistivity value for each laminate is calculated using the following expression:

$$\rho = \frac{V*s}{I*l} \qquad \text{(Eq.4.1)}$$

where V is the average voltage obtained for each current value (I). s is the cross-sectional area of the test piece calculated by multiplying the thickness of the test piece by its width, while l is the distance between the internal electrodes.

The power source used to introduce the current was a KEITHLEY 2400 multimeter operating in four-point mode. For data collection, all samples were subjected to different current intensities (1, 10, 20, 30, 40, 50, 60, 70, 80, and 100 μA), and the voltage circulating within them was measured. The experiment was repeated three times.

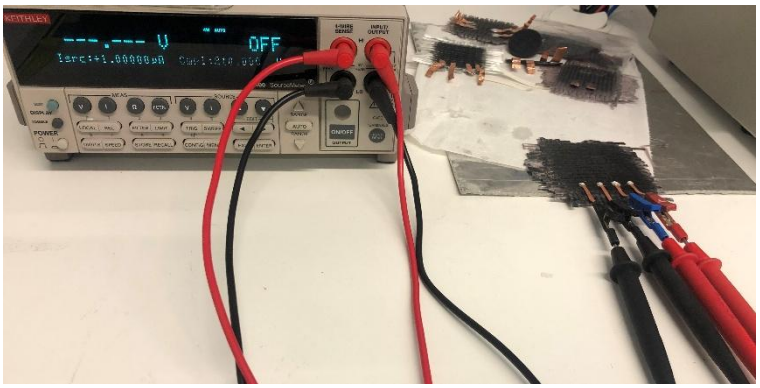

Figure 4.7 Arrangement of electrodes and instrument used for measuring resistivity.

The values of resistivity obtained for sGF and sGF/rGO are 6.6 ± 0.6 and 0.9 ± 0.3 kΩ·m, respectively. The curves of resistivity as a function of current are reported in Figure 4.8. For the sample sGF, ρ reached a plateau at higher values of current indicating that the conductive network is poorly interconnected and becomes fully activated only under strong electric fields, likely due to field-assisted tunnelling or local Joule heating[11–13]. In addition, the presence of a thin epoxy resin layer between the modified glass fibers and the measurement electrodes likely increases the overall resistivity by introducing an additional insulating barrier at the contact interface. Consequently, part of the applied voltage may drop across this layer until higher fields are reached, further contributing to the observed current dependence. The variability of the resistivity–current response among nominally identical samples indicates that the rGO conductive network lies close to the percolation threshold. Small differences in rGO dispersion or interfacial contact leads to distinct current-induced behaviours resulting in an increased error bar.

Conversely, the sample sGF/rGO exhibits a plateau at lower current, confirming the formation of a more continuous percolated network that supports charge transport even at low applied fields. In this case, the presence of rGO throughout the matrix eliminates the insulating barrier between the glass fibers and the electrodes, allowing more efficient charge transfer. Resistivity changes at high current may reveal that the electrical network is being altered by the applied current (or by the side effects of that current): electrode contact drift, self-heating, field-assisted tunnelling/contact improvement, microstructural rearrangement, or damage/oxidation[14,15].

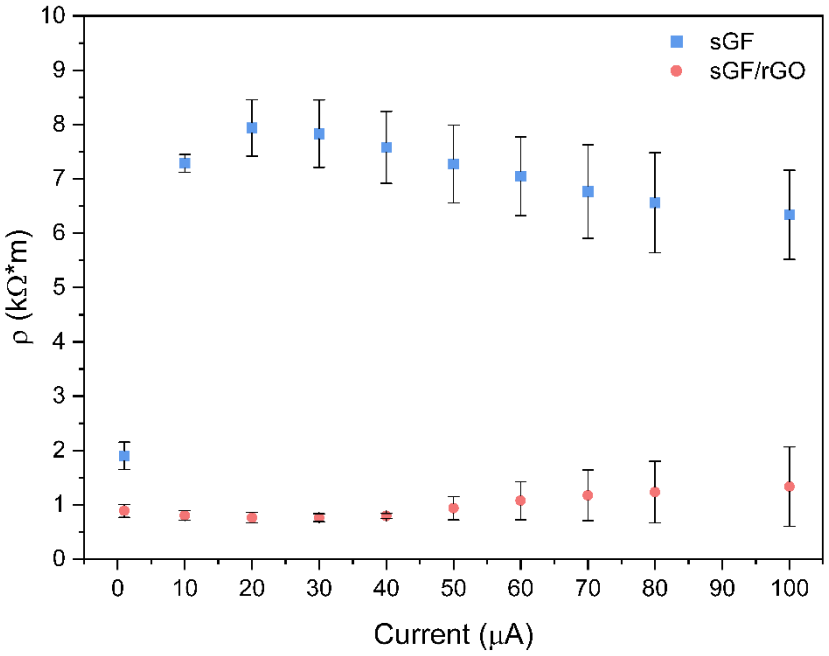

Figure 4.8 Resistivity curves as a function of current for samples sGF and sGF/rGO.

4.3 Self-healing

The damaged was made through a F3P test, stopping the machine right after the maximum of the stress-strain curve. Afterwards, the damaged specimen was healed in a hydraulic press at 140 °C for 1 h and a low pressure (2 bar) was applied to ensure contact between the cracked surfaces. The healed sample was then tested with the three-point flexural test to evaluate the restoring of the mechanical properties. Healing efficiency was calculated as the ratio between the flexural strength in the repaired and virgin state:

$$\eta\ (\%) = \frac{\sigma_{max}HEALED}{\sigma_{max}VIRGIN} * 100 \qquad \text{(Eq.4.2)}$$

The curves obtained from the F3P test are reported in Figure 4.9 a-b. The darker curves represent the test made on the virgin material that cause the damage to the specimen, while the lighter ones refer to the healed sample. The values of healing efficiency for sGF and sGF/rGO are 85 ± 4 and 109 ± 1 %, respectively (Figure 4.9c). In both case the healing efficiency results suggest that healing protocol repairs the laminates lead to high values of flexural strength and modulus comparable with the ones of the virgin materials. When the damaged material is subjected to pressure and temperature, the thermoplastic material (EMAA) flows through the crack, and ligaments are formed between the two damaged surfaces reducing the stress acting on the crack during testing and leading to an increase in fracture toughness[16].

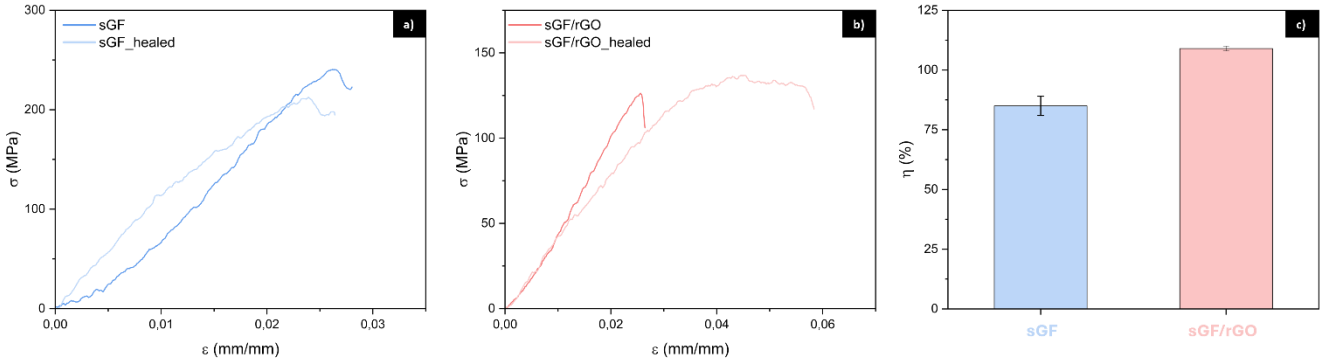

Figure 4.9 F3P representative curves pre and post healing process of a) sGF, and b) sGF/rGO; c) healing efficiency values for both laminates.

4.4 Conclusions

In this work, a novel approach for manufacturing self-healing and electrically conductive glass fiber–reinforced polymer (GFRP) laminates were developed through a simple and scalable spray-coating technique using a mixture of rGO and EMAA. This process enabled the simultaneous integration of a thermoplastic healing phase and conductive nanofillers onto the fiber surface without altering the conventional hand lay-up fabrication process.

Morphological and mechanical characterization confirmed that the spray-coating treatment did not adversely affect the fiber–matrix interface or the structural integrity of the laminates. The inclusion of EMAA and rGO on the glass fibers maintained mechanical performance comparable to that of the neat reference composite, indicating good interfacial compatibility and efficient load transfer. However, when rGO was also dispersed within the epoxy matrix, the resulting increase in viscosity hindered fiber impregnation, leading to the presence of voids and reduced flexural and interlaminar shear strength. This highlights the importance of optimizing rGO dispersion and controlling resin rheology to ensure uniform impregnation and minimize structural defects.

Electrical measurements demonstrated that the incorporation of rGO significantly reduced the composite resistivity, from approximately 6.6 ± 0.6 kΩ·m for sGF to 0.9 ± 0.3 kΩ·m when rGO was also embedded in the matrix, sGF/rGO. The latter configuration exhibited a more stable and well-percolated conductive network, enabling efficient charge transport even at low applied currents. These findings confirm the successful introduction of an electrically conductive pathway, which is essential for potential self-sensing applications.

The self-healing experiments revealed excellent recovery of mechanical properties after thermal treatment at 140 °C under low pressure. The healing efficiencies reached 85 ± 4% for sGF composite and 109 ± 1% for sGF/rGO. The latter even surpassed the initial flexural strength, suggesting enhanced stress redistribution and improved interfacial bonding during the healing process. This behaviour is attributed to the synergistic action of EMAA's thermoplastic flow and rGO's thermal conductivity, which together promote uniform heat distribution and efficient crack closure.

Overall, the results demonstrate that the rGO/EMAA spray-coating modification represents a versatile and effective strategy to impart both self-healing and electrical functionality to conventional GFRPs without compromising their structural integrity. With further optimization of filler dispersion and processing parameters, this method holds strong potential for scalable fabrication of multifunctional composite materials for structural, sensing, and damage-repair applications.

References

[1] Islam S, Bhat G. Progress and challenges in self-healing composite materials. *Mater Adv*. 2021;2(6):1896-1926. doi:10.1039/d0ma00873g

[2] Hargou K, Pingkarawat K, Mouritz AP, Wang CH. Ultrasonic activation of mendable polymer for self-healing carbon–epoxy laminates. *Compos B Eng*. 2013;45(1):1031-1039. doi:10.1016/j.compositesb.2012.07.016

[3] Pingkarawat K, Wang CH, Varley RJ, Mouritz AP. Mechanical properties of mendable composites containing self-healing thermoplastic agents. *Compos Part A Appl Sci Manuf*. 2014;65:10-18. doi:10.1016/j.compositesa.2014.05.015

[4] Pingkarawat K, Wang CH, Varley RJ, Mouritz AP. Self-healing of delamination cracks in mendable epoxy matrix laminates using poly[ethylene-co-(methacrylic acid)] thermoplastic. *Compos Part A Appl Sci Manuf*. 2012;43(8):1301-1307. doi:10.1016/j.compositesa.2012.03.010

[5] Varley RJ, Parn GP. Thermally activated healing in a mendable resin using a non woven EMAA fabric. *Compos Sci Technol*. 2012;72(3):453-460. doi:10.1016/j.compscitech.2011.12.007

[6] Chen B, Cai H, Mao C, Gan Y, Wei Y. Toughening and rapid self-healing for carbon fiber/epoxy composites based on electrospinning thermoplastic polyamide nanofiber. *Polym Compos*. 2022;43:3124-3135. doi:10.1002/pc.26605

[7] Peñas-Caballero M, Chemello E, Grande AM, Hernández Santana M, Verdejo R, Lopez-Manchado MA. Poly(ethylene-co-methacrylic acid) coated carbon fiber for self-healing composites. *Compos Part A Appl Sci Manuf*. 2023;169. doi:10.1016/j.compositesa.2023.107537

[8] Huang H chin, Zacharia NS. Layer-by-Layer Rose Petal Mimic Surface with Oleophilicity and Underwater Oleophobicity. *Langmuir*. 2015;31(2):714-720. doi:10.1021/la504095k

[9] Vázquez-Moreno JM, Sánchez-Hidalgo R, Sanz-Horcajo E, Viña J, Verdejo R, López-Manchado MA. Preparation and Mechanical Properties of Graphene/Carbon Fiber-Reinforced Hierarchical Polymer Composites. *Journal of Composites Science*. 2019;3(1). doi:10.3390/jcs3010030

[10] Yalcinkaya MA, Sozer EM, Altan MC. Effect of external pressure and resin flushing on reduction of process-induced voids and enhancement of laminate quality in heated-VARTM. *Compos Part A Appl Sci Manuf*. 2019;121:353-364. doi:10.1016/j.compositesa.2019.03.040

[11] Can-Ortiz A, Laudebat L, Valdez-Nava Z, Diaham S. Nonlinear Electrical Conduction in Polymer Composites for Field Grading in High-Voltage Applications: A Review. *Polymers (Basel)*. 2021;13(9). doi:10.3390/polym13091370

[12] Xue Y, Huang S, Sun B, Gu B. Electro-thermal coupling behavior and temperature distribution of 3-D braided composite under direct current. *Compos Sci Technol*. 2021;216:109043. doi:10.1016/j.compscitech.2021.109043

[13] Zhu D, Bin Y, Matsuo M. Electrical conducting behaviors in polymeric composites with carbonaceous fillers. *J Polym Sci B Polym Phys*. 2007;45(9):1037-1044. doi:10.1002/polb.21115

[14] Mousavi SR, Estaji S, Kiaei H, Mansourian-Tabaei M, Nouranian S, Jafari SH, et al. A review of electrical and thermal conductivities of epoxy resin systems reinforced with carbon nanotubes and graphene-based nanoparticles. *Polym Test*. 2022;112:107645. doi:10.1016/j.polymertesting.2022.107645

[15] Zhu R, Wang G, Lin Y, Long J, Du L, Du X, et al. The Electric–Thermal Effect of a Carbon-Fibre-Reinforced Epoxy Composite and Its Corresponding Mechanical Properties. *Polymers (Basel)*. 2022;14(21). doi:10.3390/polym14214489

[16] Meure S, Varley RJ, Wu DY, Mayo S, Nairn K, Furman S. Confirmation of the healing mechanism in a mendable EMAA–epoxy resin. *Eur Polym J*. 2012;48(3):524-531. doi:10.1016/j.eurpolymj.2011.11.021

5. Concluding remarks

The research presented in this thesis has focused on the design, synthesis, and characterization of multifunctional hybrid composites capable of combining structural reinforcement with self-sensing and self-healing functionalities. The work was developed along three main research streams, each contributing to a broader understanding of how hybrid nanostructures and tailored interfaces can provide polymer-based materials with intelligent and adaptive properties.

In the first part, a hybrid nanofiller based on reduced graphene oxide (X@rGO, with X = SiO_2 nanoparticles or Halloysite nanoclay) was synthesized, characterized, and incorporated into a PDMS matrix to evaluate its structural and functional performance. The bare fillers exhibited distinct morphologies: spherical SiO_2 nanoparticles (≈ 70 nm) and tubular halloysite (45 ± 15 nm diameter, 0.5–2 μm length). Hybridization followed a three-step process—APTES functionalization, GO attachment, and thermal reduction—confirmed by TGA, CHNS, ATR-FTIR, TEM, BET, Raman, and XPS analyses. Both SiO_2@rGO and Hallo@rGO contained ≈ 2 wt.% rGO, consistent with nominal values; morphological analysis indicated structural integrity of SiO_2 and partial degradation of halloysite at high temperature. When embedded in PDMS, the hybrid fillers provided clear reinforcement and tuneable electrical properties. TGA verified correct loading, while DMA showed that increasing X@rGO content enhanced the storage modulus, confirming the reinforcing action of both ceramic phases. In composites containing an additional small fraction of free rGO, the polymer relaxation peak shifted to higher temperatures, suggesting strong filler–matrix interactions that restrict chain mobility. Dielectric spectroscopy revealed that only SiO_2@rGO30%_2%rGO and Hallo@rGO30%_2%rGO achieved continuous conductive networks, as evidenced by high conductivity and frequency-dependent permittivity. Micromechanical tests on GFRP composites further emphasized the role of interfacial engineering. A simple silica coating on glass fibers improved surface coverage but not interfacial shear strength, likely due to limited porosity impeding epoxy infiltration. Conversely, incorporating SiO_2@rGO hybrids into the epoxy matrix markedly increased IFSS, confirming a synergistic effect between silica and graphene oxide. Here, silica acts as a carrier that improves rGO dispersion and prevents agglomeration, enabling stronger interfacial bonding and more efficient stress transfer.

In summary, the study demonstrates that X@rGO hybrids can be effectively synthesized from both spherical and tubular inorganic supports, ensuring stable integration of reduced graphene oxide. When introduced into PDMS, these fillers enhance mechanical reinforcement and, with added rGO, enable electrical percolation. Their incorporation into GFRPs further improves fiber–matrix adhesion and mechanical performance, offering a promising route toward multifunctional composites with self-sensing potential for structural health monitoring applications.

The second research direction focused on the development of CNTs@ZnO hybrids, combining the exceptional electrical conductivity of carbon nanotubes with the dynamic ionic crosslinking behavior of zinc oxide. The soft-chemistry synthesis enabled the controlled growth of ZnO nanoparticles on the CNT surface, as confirmed by TEM, XRD, XPS, and TGA analyses, highlighting the key role of water in promoting ZnO nucleation and crystallization. Structural and chemical analyses revealed strong interfacial interactions between ZnO and CNTs, evidenced by XPS binding energy shifts and the decrease in surface area observed by BET, confirming intimate contact between the two phases. Thermal analyses using a CNTs@ZnO–stearic acid model system demonstrated the reactivity of ZnO sites toward carboxylic groups, forming zinc–carboxylate complexes similar to zinc stearate, confirming their potential to promote crosslinking within the polymer. When incorporated into XNBR, the hybrid filler not only reinforced the mechanical performance but also acted as an intrinsic curing agent, establishing ionic Zn^{2+}–COOH interactions within the matrix. Dynamic mechanical tests confirmed excellent self-healing efficiency for all formulations, though slightly lower recovery was observed at higher filler loadings (2 wt.%), likely due to reduced dispersion and compatibility.

Overall, CNTs@ZnO proved to be an effective multifunctional filler that combines mechanical reinforcement with self-healing capability. The synergistic interaction between the conductive CNT network and the ZnO domains offers a promising strategy for the design of advanced elastomeric nanocomposites with autonomous repair functionality, suitable for applications in flexible and dynamic components such as seals, O-rings, and gaskets.

Finally, the third part extended these concepts to structural composite systems, by modifying glass fibers with coatings of reduced graphene oxide and self-healing polymers. A simple and scalable spray-coating method was developed to fabricate self-healing and electrically conductive GFRP laminates using a mixture of rGO and EMAA. This approach enabled the simultaneous deposition of a thermoplastic healing phase and conductive nanofillers directly onto glass fibers, without altering the conventional hand lay-up process. Morphological and mechanical analyses confirmed that the coating treatment preserved the fiber–matrix interface and laminate integrity. Composites containing EMAA and rGO-coated fibers maintained mechanical performance comparable to the neat reference, demonstrating good interfacial adhesion and load transfer. However, the additional dispersion of rGO within the epoxy matrix increased viscosity, causing void formation and reduced flexural and interlaminar shear strength, emphasizing the need to control resin rheology for uniform impregnation. Electrical measurements showed a significant drop in resistivity (6.6 ± 0.6 and 0.9 ± 0.3 kΩ·m for sGF and sGF/rGO respectively) confirming the formation of a continuous, well-percolated conductive network suitable for self-sensing applications. Self-healing tests demonstrated excellent recovery after thermal treatment at 140 °C under low pressure, with healing efficiencies of 85 ± 4 % for sGF and 109 ±

1 % for sGF/rGO. The latter even exceeded the original flexural strength, attributed to the synergistic effect of EMAA's thermoplastic flow and rGO's high thermal conductivity, which enhances heat transfer and crack closure.

Overall, this study demonstrates that rGO/EMAA spray-coating is a versatile and effective strategy to integrate self-healing and electrical functionality into conventional GFRPs while preserving their structural performance. With further optimization of filler dispersion and processing parameters, this method offers strong potential for scalable production of multifunctional composites for structural, sensing, and damage-repair applications.

Appendix A - Characterization method

A.1 ATR-FTIR

Attenuated Total Reflectance (ATR) spectroscopy is a Fourier Transformed Infrared Spectroscopy (FTIR) has based on the principle of total internal reflection within a crystal. As the light reflects off the crystal, a portion of it penetrates the sample. This evanescent wave interacts with the sample, energy is absorbed, and the reflected light is then detected. This absorbed energy is then measured and plotted as a function of wavelength.

ATR measurements were conducted at room temperature using a ThermoFisher Nicolet iS20 instrument, with a spectral resolution of 4 cm^{-1} and 64 scans in the range of 4000-550 cm^{-1}. The resulting ATR-FTIR spectra were processed using OMNIC software to refine the signal through background subtraction, baseline correction and normalization in the range 0-100 to ensure accurate spectral interpretation.

A.2 Charpy Impact Test

The Charpy Impact test is an analysis used to determine the amount of energy absorbed by a material during fracture under a sudden impact. In particular, the impact resistance can be calculated as follows:

$$a_{cu}\ [kJ/m^2] = \frac{E_c}{bh} \tag{A.1}$$

where E_c is the impact energy adsorbed by the specimen; while b and h are the width and the thickness, respectively. The test has been performed with a CEAST pendulum impact machine applying the *UNE-EN ISO 179:2001* standard (specimen dimensions 37.5 mm x 10 mm).

A.3 CHNS analysis

The elemental analysis (CHNS) is destructive technique for determining the concentrations of carbon, hydrogen, nitrogen, and sulphur typically used for organic materials. The analysis involves high-temperature combustion in an oxygen-rich environment, which can occur under static or dynamic conditions, often with catalysts to enhance the process. During combustion, the elements are converted in volatile molecules: C is converted to carbon dioxide, H to water, N to molecular nitrogen or nitrogen oxides, and S to sulphur dioxide. The gases are then separated by gas-chromatography, identified and quantified.

The analysis is performed using an Elementar VarioMICRO analyzer in CHNS configuration, where the temperatures of the combustion and reduction columns are at 1150 °C and 850 °C, respectively.

In this study, CHNS analysis has been used to calculate the degree of substitution in functionalized nanoparticles. As the equation A.16 in the TGA section, the following formula converts the difference in the percentage of carbon mass between the functionalized and the bare NPs in the number of functionalizing agent molecules per unit area.

$$\sigma[molecules/nm^2] = \frac{\frac{wt\,\%\,Y}{MW\,(Y)} * N_A[molecules/mol]}{wt\%_{(1000°C)}(TGA) * SSA_{BET}\,[m^2/g] * 10^{18}[nm^2/m^2]} \quad \text{(A.2)}$$

A.4 Dielectric Spectroscopy

Dielectric spectroscopy is an analysis to study how a material responds to the application of an alternating electrical field over a range of frequencies (ω). In this spectroscopy, the dielectric permittivity is the main parameter measured experimentally. When a sinusoidal electrical field ($E(\omega) = E_0 * \exp(i\omega t)$, the dielectric permittivity and the conductivity must be represented as a complex number:

Complex permittivity: $\varepsilon^*(\omega) = \varepsilon'(\omega) - i\varepsilon''(\omega)$ (A.3)

Complex conductivity: $\sigma^*(\omega) = \sigma'(\omega) + i\sigma''(\omega) = i\omega\varepsilon_0\varepsilon^*(\omega)$ (A.4)

where ε_0 is the dielectric permittivity in vacuum. The complex dielectric permittivity and the complex conductivity are correlated as follows:

$$\varepsilon'(\omega) = \frac{\sigma''(\omega)}{\varepsilon_0\omega};\ \varepsilon''(\omega) = \frac{\sigma'(\omega)}{\varepsilon_0\omega} \quad \text{(A.5)}$$

$$\sigma'(\omega) = \varepsilon_0\omega\varepsilon''(\omega);\ \sigma''(\omega) = \varepsilon_0\omega\varepsilon'(\omega) \quad \text{(A.6)}$$

The real part of the dielectric permittivity, ε', indicates how much energy is stored in the material; while the imaginary part, ε'', describes the energy loss of the material as heat, conduction or other forms. On the other hand, the real part of the conductivity, σ', gives information about the capacity of the material to conduct current, while the imaginary part, σ'', is related to the material's ability to store energy.

Another important parameter to evaluate the conductive properties of a material is the dielectric loss tangent ($tan\delta$). It is a measure of the phase angle difference between the voltage and current waveforms; this phase difference indicates the amount of energy lost in the material. This parameter is defined as follows:

$$tan\delta = \frac{\varepsilon''}{\varepsilon'} \quad \text{(A.7)}$$

The formula is a ratio between the material's loss component (energy dissipation) and its capacitance component (energy storage). So, a higher value of $tan\delta$ indicates greater energy dissipation resulting potentially a poor insulating behavior of the material.

A.5 DMA

The Dynamic Mechanical analysis is used to study the viscoelastic property when a sinusoidal deformation (strain, $\varepsilon(t)$) is applied to a material, and the stress response is measured (stress, $\sigma(t)$). In particular, following the application of a sinusoidal deformation, after an initial transient is exhausted, a stationary regime is established in the material in which the material response is still sinusoidal, with the same frequency of the strain and a phase lag ($\delta(t)$). In materials with a purely elastic behaviour, the stress and strain have the same phase (δ=0); on the other hand, in purely viscous materials, there is a phase lag of 90 degree between stress and strain (δ=π/2).

Strain: $\varepsilon(t) = \varepsilon_0 \sin(\omega t)$ (A.8)

Stress: $\sigma(t) = \sigma_0 \sin(\omega t + \delta)$ (A.9)

where $\omega = 2\pi f$ and f is the frequency of strain oscillation, while δ is the phase lag between stress and strain.

The stress response can be divided in two contributions: $\sigma'(t)$, in phase with the strain $\varepsilon(t)$, representative of an elastic behaviour; and $\sigma''(t)$, 90° out of phase with $\varepsilon(t)$, representative of a viscous behaviour.

$$\sigma(t) = \sigma_0 \sin(\omega t + \delta) = \sigma_0' \sin(wt) + \sigma_0'' \cos(wt) = \sigma'(t) + \sigma''(t) \quad \text{(A.10)}$$

The storage and loss modulus in viscoelastic materials measure the stored energy, representing the elastic portion, and the energy dissipated, representing the viscous portion. The tensile storage and loss moduli are defined as:

Storage: $E' = \frac{\sigma_0'}{\varepsilon_0} = \frac{\sigma_0}{\varepsilon_0} cos\delta$ (A.11)

Loss: $E'' = \frac{\sigma_0''}{\varepsilon_0} = \frac{\sigma_0}{\varepsilon_0} sin\delta$ (A.12)

Similarly, $G'$and G'' are defined as shear storage and shear loss moduli.

The previous equation can be written as:

$$\sigma(t) = E'\varepsilon_0 \sin(\omega t) + E''\varepsilon_0 \cos(\omega t) \quad \text{(A.13)}$$

The ratio between the loss modulus and the storage modulus is defined as $tan\delta = E''/E'$ (tensile), which provides a measure of damping in the material. Similarly, $tan\delta = G''/G'$ (shear) can be defined.

The analysis was performed using a Q800 analyser, purchased by TA Instruments (New Castle, DW, USA). Dumbbell-shaped specimens were used to perform temperature sweeps from −120 °C to 150 °C in tension mode at 15 μm amplitude, 1 Hz frequency and a heating rate of 2 °C min− 1.

A.6 DSC

Differential Scanning Calorimetry (DSC) is a thermal analysis technique used to measure the heat flow associated with material transitions as a function of temperature. During a DSC experiment, both the sample and a reference are subjected to identical heating or cooling conditions, and the difference in energy input required to maintain them at the same temperature is continuously recorded. This allows precise identification of thermal events such as melting, crystallization, glass transition, and decomposition. DSC is widely applied to characterize the thermal behaviour of polymers, metals, ceramics, and other materials, providing essential information on thermal stability, phase transitions, and heat capacity.

The analysis was performed with a DSC 3 STARe System (Mettler Toledo) with a N_2 flow of 50 mL min^{-1}.

A.7 ICP-OES

Inductively coupled plasma – optical emission spectrometry (ICP-OES) is a destructive technique used to determine the elemental composition of a solution. It involves a high-temperature plasma to excite atoms and ions in the sample, causing them to emit light at characteristic wavelengths. The emitted light is analysed by an optical spectrometer to identify and quantify the elements of the solution.

The analysis is performed using an ICP-OES OPTIMA7000 DV PerkinElmer spectrophotometer, with a constant flux of Ar of 20 L min^{-1}. A preliminary mineralization process was undertaken, involving a technique for the disintegration of the solid matrix in a liquid solution. This procedure was conducted using a microwave mineralizer (Milestone Ethos) with a mixture of strong acids: 0.20 g of powdered sample were dissolved in a Teflon beaker with 4 mL HNO_3, 4 mL HCl and 2 mL H_2O_2. The acid digestion method consists of three steps: (i) 8 min, 1000 W at 160°C, (ii) 5 min, 1000 W at 200°C, (iii) 20 min, 1000 W at 200°C. Subsequently, 12 mL of Milli-Q water was added, followed by centrifugation, and finally, the solution was diluted 1:2 with Milli-Q water, to acquire optimal values during the detection process.

A.8 Nitrogen physisorption

Nitrogen physisorption is a non-destructive analytical technique used to determine specific surface area (SSA), pore size distribution, and pore volume of solid materials. It is based on the physical adsorption of nitrogen gas onto the surface of a solid at a constant temperature of 77 K through reversible and weak physical interactions (Van der Waals forces). The output of the analysis is an adsorption isotherm, plots the adsorbed gas volume versus the relative pressure (P/P_0). In particular, as the relative pressure increases, the filling of pores with larger dimensions takes place. The size of the pores is classed, according to the International Union of Pure and Applied Chemistry (IUPAC) classification, into micropores (< 2 nm), mesopores (2-50 nm), and macropores (> 50 nm). Capillarity condensation is a common phenomenon that leads to the presence of hysteresis, which indicates differences in adsorption and desorption behaviour. Isotherms and hysteresis can be classified in different types with IUPAC.

The analysis has been performed using an Autosorb-IQ-C-MP ASiQwin Quantachrome. Various models must be used to obtain all the information needed. In this work, the Brunauer-Emmett-Teller (BET) method has been used to determine the SSA; Barrett-Joyner-Halenda (BJH) for pore size distribution; t-plot for the micropore volume and the Kelvin equation is applied for mesopore size and volume.

A.9 Push-out test

The push-out tests were performed with a self-made indentation testing device. The device can be thought of as a seesaw, with one side having a step driver and a piezo actuator for coarse and fine positioning in z direction. The other side has a combination of a microscope and a force sensor, the latter equipped with a fine flattened steel needle. The sample is mounted on a sample stage that can either be positioned under the microscope to select a fibre or under the indenter needle for fibre push-out. To calibrate the precise distance between the centre point of the microscope and the point where the indenter will hit the surface of the sample, the microscope is equipped with an xy-positioner as well. Below is a schematic representation of the push out device. The testing speed was 1 µm/s and the tests were performed at 23 ± 2 °C.

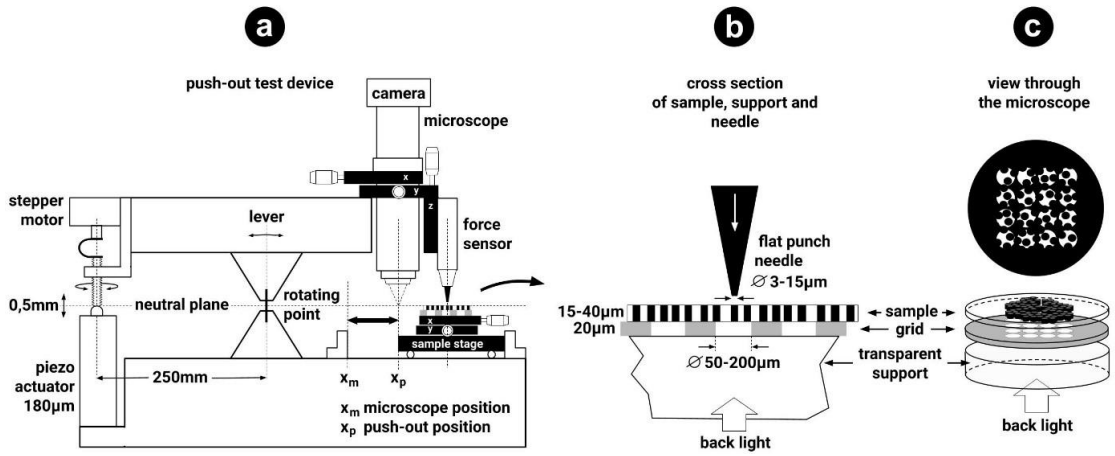

A.10 Raman spectroscopy

Raman spectroscopy is an analytical technique based on the inelastic scattering of monochromatic light, typically from a laser source, by molecular vibrations, phonons, or other excitations within a material. When incident light interacts with the molecules of a sample, most photons are elastically scattered (Rayleigh scattering), while a small fraction undergoes a change in energy corresponding to the vibrational energy levels of the molecules (Raman scattering). The energy difference between the incident and scattered photons, referred to as the Raman shift and expressed in wavenumbers (cm^{-1}), provides a unique spectral fingerprint characteristic of the molecular structure and bonding environment. Because each material exhibits distinct vibrational modes, Raman spectroscopy enables both qualitative and quantitative characterization of compounds with minimal or no sample preparation.

In this work, Raman spectroscopy has been used to evaluate the D and G band of graphene oxide using a Jasco Ventuno µ-Raman instrument with a Peltier-cooled charge-coupled device (CCD) camera (operating temperature: −50 °C) and a He−Ne laser (wavelength, 632.8 nm; power density, 6 kW cm^{-2}).

A.11 SEM

The Scanning Electron Microscope (SEM) is a highly versatile tool for morphological characterization, allowing the examination of relatively large specimens with resolutions and magnifications far superior to those achievable by conventional light microscopy. In SEM, a focused high-energy electron beam is directed onto the sample within a vacuum chamber, where a system of electromagnetic lenses controls the beam's focus and deflection. The interaction between the electrons and the sample generates various emission signals, which are collected and processed into detailed images through dedicated

detection and imaging software. The electron beam originates from an electron gun, which may operate via thermionic emission or field emission, depending on the instrument's configuration.

SEM images were collected by a Zeiss Gemini 500 microscope in a high-vacuum configuration. The electron beam excitation was 30 kV at a beam current of 25 pA, and the working distance was 12 mm. In this configuration, the beam spot was 38 nm. The samples were dispersed in EtOH, deposited onto an aluminium substrate by drop-casting and covered with gold coating.

A.12 TEM

Transmission Electron Microscopy (TEM) is a highly powerful technique for the morphological characterization of nanostructured materials, offering significantly higher resolution than Scanning Electron Microscopy (SEM). In TEM, a high-energy electron beam, accelerated up to 300 kV, is focused through a series of electromagnetic lenses to generate high-resolution images. The sample, usually placed on a 3 mm copper grid, is penetrated by the beam, producing transmitted and elastically scattered electrons. These electrons form a diffraction pattern that is reconstructed by the projection lens into a detailed two-dimensional image of the sample. TEM enables visualization of fine structural features with a resolution of up to 0.17 nm, making it particularly suited for studying nanoparticles, powders, and ultrathin composite sections.

TEM images were collected by using a JEOL JEM-2100Plus TEM operating at an acceleration voltage of 200 kV, equipped with an 8-megapixel Gatan Rio complementary metal-oxide-semiconductor camera. The samples were deposited onto carbon-coated Cu TEM mesh grids by drop-casting dilute NPs dispersions in ethanol.

A.13 Three-point Flexural Test (F3P)

This technique has been used to evaluate the mechanical properties of the GFRP composites. The analysis has been performed using an INSTRON 2204 with a static load cell of 50 kN and a velocity of 1 mm min^{-1} applying the *ASTM D790* standard (specimen dimensions: 50.8 mm x 12.7 mm; span: 25.4 mm). Starting from the curves obtained of applied force and displacement (F vs D), the flexural strength, σ, and the deformation, ε, have been calculated with following formulas:

$$\sigma\,[MPa] = \frac{3FL}{2bh^2} \tag{A.14}$$

$$\varepsilon\ [mm/mm] = \frac{6Db}{L^2} \quad \text{(A.15)}$$

where L is the span distance; b and h are the width and the thickness of the specimen, respectively. Moreover, the flexural modulus, E_f, which measures the material's stiffness in bending, can be calculated starting from the slope, m, of the linear part of the curve σ vs ε:

$$E_f\ [GPa] = \frac{mL^3}{4bh^3} \quad \text{(A.16)}$$

This test can be also used to obtain the Interlaminar Shear Strength ($ILSS$) changing the dimensions of the specimen and the span distance applying the *ASTM D2344* standard (specimen dimensions: 15 mm x 7.5 mm; span: 7.5 mm). In particular, the value must be determined as the maximum point of the curve $ILSS$ (τ_{12}) vs D.

$$\tau_{12}\ [MPa] = \frac{3F}{4bh} \quad \text{(A.17)}$$

A.14 TGA

Thermogravimetric analysis is a destructive technique to record the weight loss percentage of the samples during heating, occurring due to decomposition reactions, oxidation, and physical processes such as vaporization and desorption of solvent molecules.

This analysis was used to estimate the number of surface hydroxyl (OH) groups of the bare NPs. The calculation is based on the following formula:

$$OH_{sup}[mol/g(NPs)\ ] = \frac{2 * \Delta wt\%_{(OH+OEt)st}}{MWH_2O * wt\%_{(1000°C)st}} \quad \text{(A.18)}$$

where $\Delta wt\%_{(OH+OEt)st}$ is the normalized weight loss percentage in the range 150 °C-1000 °C, assuming that before 150°C no significant loss occurred a part of organic contaminants or adsorbed solvent molecules on the surface; $wt\%_{(1000°C)st}$ is the normalized weight loss percentage at the end of the treatment. The number of OH per unit surface area can be calculated as follows:

$$OH_{sup}[molecules/nm^2] = \frac{OH_{sup}[mol/g(NPs)] * N_A[molecules/mol]}{SSA_{BET}[m^2/g] * 10^{18}[nm^2/m^2]} \quad \text{(A.19)}$$

where SSA_{BET} is the specific surface area obtained through a nitrogen physisorption analysis using the BET method.

The TGA experiments were performed with a TGA 2 STARe System in the temperature range 30-1000 °C, with a constant air flow (50 mL min^{-1}) and a heating rate of 10 °C min^{-1}. An isothermal step at 150 °C (15

min) was used to complete the weight loss due to physiosorbed solvent molecules and water and a second one at 1000 °C (5 min). The sample holder was an alumina pan with a volume of 75 µL.

Equation X can be used to estimate the degree of functionalization of grafted nanoparticles. In deep, the weight loss percentage between 150 °C and 1000 °C can be attributed only to the functionalizing agent assuming that each silane binds with x available OH groups. The unreacted hydroxyl groups are also lost in this temperature range and accounted in the formula.

$$wt\%(Y) = \frac{\Delta \mathrm{wt\%}_{(150-1000°C)st} - \Delta wt\%_{(OH+OEt)st}}{MW(Y) + MW(H_2O)\frac{(3-2x)}{2}} MW(Y) \quad 1 \leq x \leq 3 \tag{A.20}$$

The $wt\%(Y)$ can be converted into σ, the number of molecules per unit area calculated through the SSA_{BET} of the bare NPs.

$$\sigma[molecules/nm^2] = \frac{\frac{wt\%\,Y}{MW(Y)} * N_A[molecules/mol]}{wt\%_{(1000°C)st} * SSA_{BET}[m^2/g] * 10^{18}[nm^2/m^2]} \tag{A.21}$$

A.15 XPS

X-ray Photoelectron Spectroscopy (XPS) is a surface analysis technique that identifies the elements and their chemical states within the top 5–10 nm of a material. It works by irradiating the surface with X-rays, causing electrons to be emitted. By measuring their kinetic energy, XPS determines the binding energies of the electrons, which are characteristic of specific elements and chemical environments. From the spectra, XPS provides elemental composition, oxidation states, and bonding information. It can also yield quantitative data (atomic percentages) and, when combined with ion sputtering, a depth profile of the sample.

The employed XPS apparatus is a custom-built system, consisting of an analysis chamber equipped with a non-monochromatic Mg source (Kα = 1253.6 eV, VSW-TA10), and a hemispherical analyser (VSWHA100) with a 16-channel detector. The base pressure of the analysis chamber is around $1*10^{-9}$ mbar. The survey spectra have been registered using a pass energy of 44 eV, while the regions of interest (ROI) have been registered using a pass energy of 22 eV. In both the cases the total power of the source was 144 W (12 mA, 12 kV) and the XPS spectra has been registered at a normal emission angle.

A.16 XRD

To evaluate the crystallinity of ZnO NPs decorating the structure of CNTs, Powder X-ray diffraction (XRD) has been collected at room temperature with a Rigaku MiniFlex 600 diffractometer, operating with

Bragg-Bentan geometry. In this setup, a Cu Kα radiation X-ray source (λ_1=1.5406 Å, λ_2= 1.5443 Å) was used and the X-ray generated are collimated by slits before reaching the sample. The sample was located in an amorphous holder with crystallites placed in a random orientation, to avoid systematic errors in the diffractogram. The X-rays coming from the sample pass through the receiving slits and reach the detector. The diffractogram shown in the thesis was performed in the 2θ range of 15-80° with a 2θ step 0.02° and 1° min^{-1} scan rate.

A.17 XRF

To evaluate the composition of CNTs bare, CNTs_TA and CNTs@ZnO, X-ray Fluorescence Spectroscopy was performed. This analysis determines the elemental composition of materials by irradiating the sample with high-energy X-rays and detecting the resulting secondary (fluorescent) X-rays, whose characteristic energies correspond to the elements present.

XRF was performed using a micro-XRF spectrometer Bruker ARTAX 200 equipped with a Mo anode X-ray tube, collimated down to 0.65 mm in diameter (excited sample area of 0.33 mm^2). The spectra were obtained by operating at 20 kV and 1.0 mA and with an acquisition time of 300 s. The attributions of each signal were performed by using the XRF software.

La borsa di dottorato cofinanziata con risorse dell'Unione europea-*NextGeneration EU*
Piano Nazionale di Ripresa e Resilienza Missione 4 – Componente 1 – Riforma 4.1 Riforma dei Dottorati – Inv. 4.1
Borse PNRR patrimonio Culturale –*CUP H41J22000230009*